



UNIVERSITÀ  
DEGLI STUDI  
FIRENZE

DOTTORATO DI RICERCA IN  
FISICA E ASTRONOMIA

CICLO XXVIII

**Competition between  
heavy-ion reaction mechanisms  
as a function of the system isospin**

Settore Scientifico Disciplinare FIS/04

**Dottorando**  
Dott. Simone Valdré

**Tutore**  
Dott. Giovanni Casini

**Coordinatore**  
Prof. Roberto Livi

Anni 2012/2013 — 2013/2014 — 2014/2015



---

# Contents

---

<b>Introduction</b>	<b>1</b>
<b>1 Physics case</b>	<b>5</b>
1.1 Heavy-ion reaction mechanisms . . . . .	6
1.1.1 Energy and impact parameter . . . . .	6
1.1.2 Central collisions . . . . .	9
1.1.3 Peripheral and semiperipheral collisions . . . . .	11
1.1.4 Pre-equilibrium emissions . . . . .	13
1.2 Nuclear matter and the equation of state . . . . .	15
1.2.1 Liquid drop model . . . . .	16
1.2.2 Equation of state of nuclear matter . . . . .	17
1.2.3 Asymmetric nuclear matter . . . . .	18
1.2.4 Observables related to the isospin . . . . .	20
<b>2 The experimental apparatus</b>	<b>23</b>
2.1 Garfield . . . . .	24
2.1.1 Drift chamber with microstrip electrodes . . . . .	26
2.1.2 CsI(Tl) crystals . . . . .	28
2.2 Ring Counter . . . . .	30
2.3 The electronics . . . . .	31
2.3.1 DSP algorithms . . . . .	32
2.3.2 Trigger and acquisition . . . . .	34
<b>3 Calibrations and particle identification</b>	<b>37</b>
3.1 Preliminary operations . . . . .	37
3.1.1 Bad signal rejection . . . . .	37
3.1.2 Garfield microstrip angular calibration . . . . .	37
3.1.3 Pulser run . . . . .	38
3.2 Particle identification . . . . .	39

3.2.1	Particle identification techniques . . . . .	39
3.2.2	Identification techniques in Garfield . . . . .	41
3.2.3	Identification techniques in the Ring Counter . . . . .	44
3.3	Energy calibration . . . . .	46
3.3.1	Energy calibration of the Garfield CsI(Tl) crystals . . . . .	46
3.3.2	Energy calibration of Ring Counter CsI(Tl) crystals . . . . .	47
3.3.3	Energy calibration of gas detectors . . . . .	47
3.4	Refinement of energy loss calculations . . . . .	49
3.4.1	Stopping power in materials . . . . .	49
3.4.2	Stopping power in gas . . . . .	51
3.4.3	Improvements obtained in Ring Counter . . . . .	53
3.5	Efficiency considerations . . . . .	54
3.5.1	Garfield efficiency . . . . .	54
3.5.2	Ring counter efficiency . . . . .	55
<b>4</b>	<b>Theoretical models and event simulations</b>	<b>57</b>
4.1	Dynamical models . . . . .	57
4.2	Statistical decay . . . . .	60
4.3	The TWINGO code . . . . .	61
4.3.1	General considerations . . . . .	61
4.3.2	Fusion-like events . . . . .	66
4.3.3	DIC events . . . . .	69
4.3.4	Asy-stiffness effects . . . . .	74
4.4	The Gemini++ statistical model . . . . .	74
4.5	Geometrical filter . . . . .	77
<b>5</b>	<b>Data analysis and results</b>	<b>79</b>
5.1	General event features . . . . .	79
5.1.1	Cleaning conditions . . . . .	79
5.1.2	Event selection . . . . .	80
5.1.3	Carbon background . . . . .	85
5.2	Fusion-like events . . . . .	89
5.2.1	Fusion-evaporation events . . . . .	90
5.2.2	Fusion-fission events . . . . .	98
5.3	DIC events . . . . .	99
5.4	The isospin of the heavy fragments . . . . .	104
5.5	Estimation of cross sections . . . . .	107
	<b>Summary and conclusions</b>	<b>111</b>
	<b>Bibliography</b>	<b>117</b>
	<b>Ringraziamenti</b>	<b>119</b>

---

## Introduction

---

Nuclear physics is still playing a major role in fundamental research thanks to the progresses done in the last decades both experimentally and theoretically. In fact nuclear physics is a unique way to investigate aspects of nature still not fully understood, and not accessible by other routes. Since the discovery of radioactivity, nuclear physics studies have driven human knowledge from the nature of nuclei and their charge and matter distribution, continuing incessantly through beta decay and neutrino discovery, up to cosmic rays and sub-nuclear particles. The study of the nuclear structure begins from the Thomson's "plum pudding atomic model", and through the crucial Rutherford experiment comes to the improved Bohr's model. These studies stimulated the evolution of the nuclear physics leading to consider the nucleus a complex system ruled by strong and Coulomb interactions. Afterwards, technological innovations enabled new ways to approach this science, opening the long, very busy road of nuclear reactions.

The goal of nuclear physics is the understanding of the properties of the matter that constitutes our Universe. Nuclear reaction studies aim to reach this goal via the analysis of different reaction mechanisms and the synthesis of new nuclear species. In particular, heavy-ion nuclear reactions performed with projectiles accelerated at  $\beta \gtrsim 0.15$  can lead nuclear systems to extreme conditions of temperature, spin and density, far from the case of nuclei in their ground state. For instance, it is possible to approach conditions found only inside neutron stars or supposed to be present in core-collapses of supernovae and investigate the behaviour of nuclear matter varying its density, pressure, volume, isospin: namely, the Equation Of State for finite nuclear matter.

Stimulated by these great opportunities, in the last decades nuclear research fo-

cused on thermodynamic aspects of heavy-ion reactions at intermediate energies. In particular, one of the hot topic has been the investigation of the very fascinating and exciting world of the phase transitions and, more in general, of the whole class of critical phenomena, with the additional issue related to the finite size of the considered systems. Indeed, nuclei present thermodynamical facets which are strongly impacted by the finite number of constituents. In this regard, it can be worth citing the works about the similarities between the nuclear matter phase transitions and cosmo-gravitational phenomena like the early Universe evolution after the Big-Bang and gravitational collapses [1]. The possibility of a liquid-gas phase transition in nuclear matter and the existence of a region where the two phases can coexist have been theoretically predicted since the 60s. Then they were experimentally signaled and studied in a huge set of experiments, and they are a subject of debate still nowadays. Indeed, a strong support to this topic just arrived from heavy-ion reaction studies as presented among the others in [2]. From an experimental point of view, those topics are addressable through multifragmentation and isospin transport phenomena at intermediate energies (the so called “Fermi energy regime”, ranging from  $\sim 20$  to about  $\sim 100$  MeV/u). At lower energies (5–20 MeV/u) less explosive phenomena happen. For example, reactions in many cases lead to the formation of one or two excited nuclei that decay mainly by emitting light particles. Between the two previously mentioned energy regimes there is a region where the characteristic low energy phenomena are dominant, but they show some behaviour typical of Fermi energy reactions (pre-equilibrium emissions, isospin diffusion, etc. . . ) as it will be better discussed in Chapter 1: the experiment described in this thesis is just within this energy region.

Of course, it can be hard to imagine being able to recreate in laboratory what, up to the advent of particle accelerators, was observed only in the sky. On the other hand the development of these facilities to reach high energies for experiments have implied big technological and interpretative efforts. First of all, the evolution of the phenomena triggered in a laboratory environment takes a very short time, of the order of  $\sim 10^{-22}$  s, and their observation depends on the asymptotic information that we can achieve by the reaction products, properly collected on a typical time scale of  $\sim 10^{-9}$  s by means of a (simple or complex) detector apparatus. Starting from the detected reaction products and the analysis of their features it is possible to go back to the reaction process and to characterize the emitting sources. Information about the number of primary sources and their possible relationship, their size, excitation energy, temperature and  $N/Z$  ratio can be accessible. To achieve this goal, the collection of the reaction products together with their characterization

in term of charge, mass and energy must be as complete as possible. So there has been a crucial effort worldwide in the last two decades to build large acceptance multidetectors that, covering a large solid angle around the target, are able to collect fragments and light particles from collisions with very high efficiency. Among the many multidetectors used worldwide, in Chapter 2 of this thesis the GARFIELD apparatus will be described. GARFIELD (General ARray for Fragment Identification and for Emitted Light particles in Dissipative collisions) is located at Legnaro National Laboratories (LNL) of INFN. This multidetector was used in the experiment which is at the basis of this work and it has been designed and upgraded by the collaboration in which the present activity has been carried out.

Large acceptance detectors are of course composed of a large number of sensors. Moreover, for each sensor, we can have more than one electronic channel. The raw data coming from the apparatus need to be calibrated to extract the energy and the other relevant parameters (positions, velocities, etc...) of the particles. Furthermore, correlations among the various measured quantities are useful to identify the various ions; in particular they allow to reconstruct the charge, and in some cases also the mass, of the detected particles. In our case we have in total almost 400 independent electronic channels and their data processing was a pretty difficult and complex procedure, on which I spent a large part of my PhD work. For this reason the whole Chapter 3 is dedicated to the long and accurate work of data calibration and particle identification.

As in many similar studies on heavy-ion reactions, the goal of this thesis is to add knowledge and to improve the comprehension of the various processes which are often acting together to produce the final distributions and observables. Commonly, there is not a unique parameter to be measured which give a definitive answer on a specific issue; instead the richness and the quality of the data, properly analyzed, allow to progress. In this respect it is extremely important the comparison with predictions of models, better if available in Monte Carlo versions as event generators. Therefore, during my thesis work, we have been in touch with the theorists expert in SMF model. This is a very accredited dynamical model among the heavy-ion physics community and it is particularly suitable for Fermi energies, but it can also be extended to our energy region. The collaboration is of course in progress and it is motivated both by the data presented here and by applications at Fermi energies, now under investigation with the FAZIA telescopes. In Chapter 4 SMF model is described and many simulated spectra produced with different parametrizations are shown.

Finally, in Chapter 5 the results of data analysis are reported. In particular we

focused on the different behaviour of our two examined systems, that only differ in the neutron content of the target. Our analysis covers various topics related to isospin and thus it can be considered as a modern bridge study towards the field of reaction mechanisms investigated with energetic exotic beams. Here we study the formation and decay of fragments in fusion-like or dissipative reactions by varying the isospin content of the system with the only practical method, i.e. by changing the neutron richness of the target. Using radioactive beams made of unstable nuclei coming from the fission of Uranium, as it will be done with SPES at LNL, we will be able to push the initial neutron richness of the system to an unprecedented extent. The investigation of how the properties of the fragments evolve and how the various reaction mechanisms change from peripheral to central collisions in such exotic excited systems will be extensively approached.

# CHAPTER 1

---

## Physics case

---

The study of heavy-ion collisions has been carried on for over thirty years, namely since the technology required to accelerate ions has become available at the various energy regimes. In general, ion collisions allow to obtain information on the behavior of nuclear matter far from normal conditions and to study the reaction mechanisms on a wide energy domain. Indeed, with specific experimental techniques we can make nuclei to fuse at extremely low energies of tens keV (the ones typical of the normal stellar burning regime) or to reach the enormous energies at LHC (CERN). Here, at the extremely ultrarelativistic energies above 1 TeV/u, the ALICE experiment studies very high temperature and low baryonic density systems, where the phase transition from hadron gas to quark-gluon plasma is supposed to happen.

reaction	$\left(\frac{N}{Z}\right)^{(\text{sys})}$	$E_{\text{cm}}$ [MeV]	$Q_{\text{gg}}$ [MeV]	$E^*/A$ [MeV/u]	$\vartheta_{\text{gr}}$ [deg]	$l_{\text{gr}}$ [ $\hbar$ ]	$\sigma_{\text{R}}$ [barn]	$\sigma_{\text{F}}$ [barn]
$^{32}\text{S} + ^{40}\text{Ca}$	1.00	312.7	-6.8	4.25	5.4	142	2.37	0.52
$^{32}\text{S} + ^{48}\text{Ca}$	1.22	337.8	+7.7	4.32	5.2	158	2.53	0.58
$^{32}\text{S} + ^{48}\text{Ti}$	1.11	337.8	-4.2	4.17	5.8	157	2.49	0.55

**Table 1.1:** For the three studied reactions, isospin ratio of the whole system, total centre-of-mass energy,  $Q$ -value for complete fusion, compound nucleus excitation energy per nucleon, grazing angle, grazing angular momentum, total reaction cross section (Gupta model estimation [3]) and fusion cross section (Bass model estimation [4, 5]) are reported.

This thesis is focused on the data analysis of a heavy-ion experiment performed in the third hall of *Laboratori Nazionali di Legnaro* (LNL), where our detector

setup is installed. We used a 200 ns pulsed  $^{32}\text{S}$  beam at  $(565.5 \pm 0.1)$  MeV (around 17.7 MeV/u) from the ALPI linear accelerator. This corresponds to a beam velocity of 57.60 mm/ns ( $\beta = 0.1921$ ) close to the maximum velocity available for S ions at Legnaro. Average beam intensity was about 0.1 pA, corresponding to about  $6 \cdot 10^8$  pps. In Table 1.1 the main reaction parameters are reported for the three systems studied in this work. The meaning of the parameters is explained in the following sections. In Table 1.2 the targets available during the experiment are specified. In particular we focused on the two Calcium targets, while the Titanium one was used for a secondary measurement and it is considered only in few comparisons in the following Chapters. We note that Calcium targets are covered by thin Carbon foils (10  $\mu\text{m}$  thick) on both sides to prevent oxydation. For this reason, we used also a Carbon target to estimate the background (see §5.1.3).

target	used for	thickness $[\frac{\mu\text{g}}{\text{cm}^2}]$	$(\frac{N}{Z})^{(\text{tar})}$
$^{40}\text{Ca}$	measurement	500 ( $^{40}\text{Ca}$ ) + 20 ( $^{12}\text{C}$ )	1.00
$^{48}\text{Ca}$	measurement	500 ( $^{48}\text{Ca}$ ) + 20 ( $^{12}\text{C}$ )	1.40
$^{48}\text{Ti}$	measurement	600	1.18
$^{197}\text{Au}$	calibration	200	1.49
$^{12}\text{C}$	background	15	1.00

**Table 1.2:** List of the available targets during the experiment. For each target, thickness and isospin ratio are reported.

## 1.1 Heavy-ion reaction mechanisms

### 1.1.1 Energy and impact parameter

Heavy-ion reactions are one of the most important tools used to study the nuclear Equation of State and obtain its parameters. Moreover, these reactions allow to investigate the large number of nuclear degrees of freedom, both collective and intrinsic, characterized by different typical energies and time scales. It is also possible that reactions between ions produce many unstable species not found in nature, whose internal structure, when identified, can be investigated.

The interaction between nucleons inside two colliding nuclei can be explained via a mean field potential (one-body) and/or in a complementary way via a two body dissipation process, depending on the energy involved in the reaction. In the first case, when a nucleon hits a nucleus, it “feels” all the nucleons together

inside the nucleus (the so-called mean field approach), while in the second case the interactions are with the individual nucleons. We can qualitatively order the competition between these two processes through the following considerations. In a nucleus-nucleus ( $A$ - $A$ ) collision, the relative velocity  $v_r$  (and so the relative energy) is related to the reduced relative wavelength  $\lambda = \hbar/2\pi\mu v_r$  by the expression

$$\lambda = \frac{\hbar}{\mu v_r}$$

where  $\mu$  is the reduced mass of the system. As the relative energy between nuclei increases, the associated  $\lambda$  decreases.

In a fixed target collision, where  $v_r = v_b$  (beam velocity), we can talk in terms of beam energy: rising values of beam energy (1, 10, 100 and 1000 MeV/u) correspond to decreasing values of  $\lambda$  ( $6.5/A$ ,  $2.1/A$ ,  $0.67/A$  and  $0.24/A$  fm respectively). If we compare these lengths with the average distance between nucleons in the nuclei ( $\sim 1.2$  fm), we can see that in low energy collisions (up to about 20 MeV/u), the mean field dissipation process prevails. In fact, each nucleon of the incident nucleus “sees” the whole target nucleus around itself, experiencing the nuclear and the Coulomb effective interaction as an average potential of all the neighbouring nucleons. In this mean field energy region many reactions have been studied with several techniques and the various processes have been highlighted and described with accuracy. In this energy regime the Pauli exclusion principle reduces the probability of nucleon-nucleon collisions because, due to the small kinetic energy transferred to the nucleons in the reaction, the possibility to reach a free single particle state is reduced. So, as a general characteristic, explosive dynamics is inhibited and we usually have several particles and a few heavy products in the exit channel.

At higher energies, the associated wavelength is short enough to be compared to the nucleon-nucleon relative distance and consequently the two body interactions gain more and more relevance. At intermediate energies, a regime that is also referred to as Fermi energies (between 20 and 100 MeV/u), we have a very rich phenomenology due to the concomitant role of nucleon-nucleon collisions and the nuclear mean field. The former intervene more and more when the energy increases during the overlap of the two nuclei thanks to the large number of single states made available by high velocities. The latter defines the macroscopic properties of the interacting nuclei and continues to play a very important role with regard to the collective degrees of freedom of the sub-systems that are gradually formed.

The experiment studied in this work, as said before, consists of typical fixed target reactions performed with a  $^{32}\text{S}$  beam at 17.7 MeV/u. Therefore we are in

a region where the mean field approach is dominant, but some contributions from nucleon-nucleon (N-N) collisions must be considered to correctly interpret the measured variables.

Beside beam energy, the interaction processes strongly scale with the impact parameter  $b$ . In a semiclassical approach, its value is the distance between the projectile velocity direction and the center of the target nucleus. Unlike the bombarding energy or the projectile and target nuclear species, we cannot choose a priori the impact parameter; we can just try, event by event, to extract the value of  $b$  or some order parameter from the measured observables.

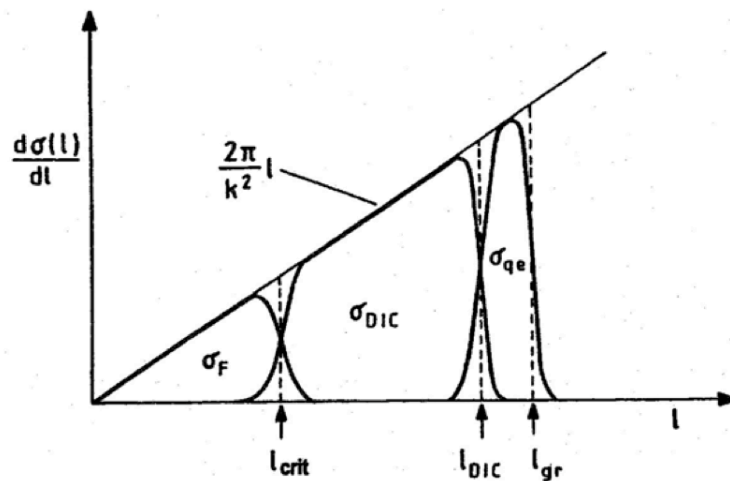


**Figure 1.1:** . Schematic classification and cross sections of different reaction mechanisms on the basis of the entrance channel angular momentum  $l$ . Impact parameter  $b$  is directly proportional to  $l$ .

The value of the impact parameter not only determines the nuclear overlap between projectile and target, but it also drives the reaction toward different interaction mechanisms (Figure 1.1). The minimum value of  $b$  at which nuclear forces are negligible with respect to Coulomb interaction is called “grazing” value ( $b_{gr}$ ). So, when  $b > b_{gr}$ , the Coulomb repulsive potential is the only actor in the interaction (elastic scattering). When  $b$  decreases, indeed, the strong nuclear force gets more and more relevance with respect to the Coulomb interaction and inelasticity rises as the effect of “friction” forces.

We introduce now the main reaction mechanisms between heavy ions and their occurrence at the various energy regimes and at different impact parameters. A schematic representation of the different processes is also shown in Figure 1.2.

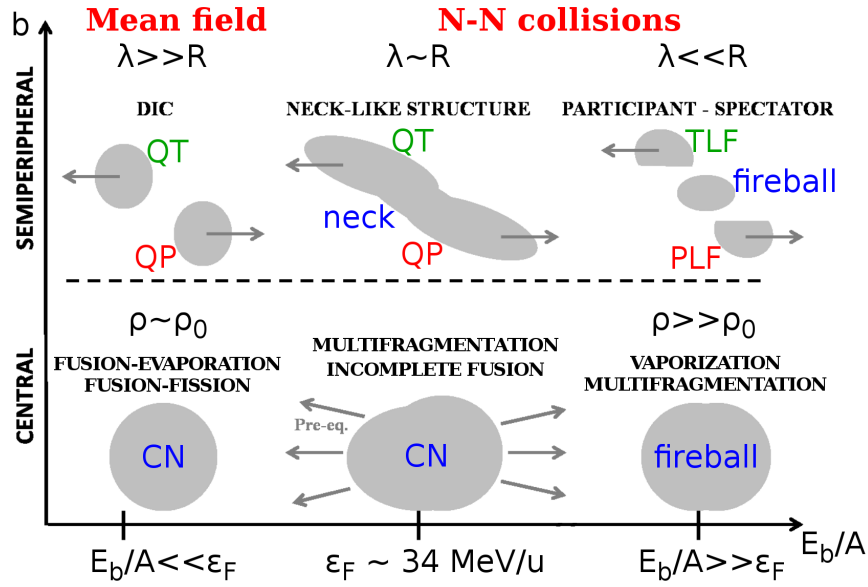


**Figure 1.2:** Schematic diagram of the possible evolutions of a nuclear collision depending on bombarding energy per nucleon ( $E_b/A$ ) and impact parameter  $b$ . The relation between the reduced relative wavelength  $\lambda$  and the average distance  $R$  between the nucleons in the nuclei determines the different interactions between the reacting nuclei (mean field or nucleon-nucleon).

## 1.1.2 Central collisions

### Mean field energy region

Under 10 MeV/u bombarding energy, in case of central collisions, the concurrence of relatively long interaction times ( $\sim 10^{-21}$  s) and moderate excitation energies ( $\lesssim 3$  MeV/u) allows one to assume that the system reaches equilibrium in all its internal degrees of freedom, thus arriving at thermal and chemical equilibrium just before the de-excitation phase. This scenario corresponds to assume two distinct phases of the interaction: the creation of the so-called compound nucleus (CN) and its following decay.

The statistical model concepts, largely used through this thesis (see Chapter 4), are based on the fact that once the CN is created, it forgets the dynamics which has been necessary to produce it. In fact, considering a complete fusion, one can completely characterize the CN in terms of charge  $Z_{CN}$ , mass  $A_{CN}$  and excitation

energy  $E^*$  starting from the projectile and target:

$$\begin{aligned} A_{\text{CN}} &= A_p + A_t \\ Z_{\text{CN}} &= Z_p + Z_t \\ E^* &= E_{\text{CM}} + Q_{\text{gg}} \end{aligned}$$

where  $Z_p$  ( $Z_t$ ) and  $A_p$  ( $A_t$ ) are the projectile (target) charge and mass respectively,  $E_{\text{CM}}$  is the total kinetic energy of the system in the centre-of-mass frame and  $Q_{\text{gg}}$  is the  $Q$ -value of the reaction. Also the initial orbital angular momentum of the system is effectively transferred to the CN, which can so reach high spin values. In many cases high thermal and collective excitations characterize the produced compound nucleus, allowing to study nuclear decay from very excited sources.

Typically, after CN formation, the system can undergo evaporation or fission. In the former case the compound nucleus loses its excitation energy by emitting light particles and  $\gamma$ -rays; the remaining nuclear fragment is called evaporation residue (ER). In the latter case the CN undergoes a complicate path ruled by the Coulomb and strong forces, it deforms and finally it splits in two fragments. The two channels are not exclusive: indeed, some neutron or charged particle evaporation can occur from the CN along the road to the scission. The two fission fragments can be still excited above the particle separation energies and some residual particle evaporation can occur from one or both of them. In a statistical scenario, as currently assumed to treat the decay, the system evolution is ruled by the competition of the various channels according to their statistical weight, independently of the previous history of the process. As a general trend, for a given nucleus the fission is favoured in high spin configurations and also (but not strictly) by strong excitation energies.

### Fermi energy regime

When the energy increases, in general, the assumption of two separated stages (formation and decay) in the CN evolution weakens. The interaction becomes gradually faster and equilibrium may not be reached before de-excitation. Different processes, mainly linked to the dynamics of the collision and difficult to be experimentally disentangled, can occur. For example, for central collisions, a quasi-fusion (or incomplete fusion) scenario can appear: the compound nucleus is produced after some particle emission (pre-equilibrium emission), so that the CN mass isn't anymore the sum of the interacting nuclei masses and its excitation energy is lower than in the case of complete fusion. In other cases, a true fusion process is inhibited by the centrifugal entrance channel barrier: the contributing  $l$ -waves are such that an at-

tractive pocket cannot be formed during the reaction. Instead, a transient system that survives in a di-nuclear potential for a long time without passing through states of a true CN (quasi-fission) is produced.

Going deeper into the Fermi energy regime, the nuclear matter transition from liquid to gas can be studied, among other topics, specifically in central collisions, where a large and very excited system (fireball) can be more easily formed. The fireball is a region characterized by high temperature and density, that usually decays by disintegrating into light particles (vaporization). The gas state is associated to the vaporization mechanism, while the CN formation may be intended as the liquid state.

Just due to the concurrent role of N-N collisions and mean-field, the system can be brought into the spinodal region of the equation of state. This region is characterized by strong mechanical instabilities and the nuclear system can break apart in many fragments (multifragmentation) [2, 6–8]. The search for possible liquid-to-gas phase transition in nuclei strongly heated and compressed has been motivated by some analogy of the phenomenological nuclear potential with the molecular Van der Waals potential of fluids. For this reason, considering the nuclei as thermodynamic systems subject to phase transition must not surprise. The transition characteristics depend both on the energy of the input channel and on the impact parameter. Especially for almost central collisions, the system first reaches high-density configurations (up to 2–3 times the saturation density), then expands before re-separating in many particles and fragments, at densities far below the saturation value ( $\rho \sim 0.2 \rho_0$ ). During these phases, which have different time scales, abundant emissions may occur. The energy densities typical of the multifragmentation phases with possibly related liquid-gas phase transition are above 4–5 MeV/u.

The reactions studied in this work, even in case of complete fusion, lead to energy density not larger than 4 MeV/u. Therefore one can expect only a marginal contribution (some percent) of multifragmentation in our measured central collisions. A fortiori multifragmentation can be excluded for the excited QP and QT in dissipative collisions. Thus, this important subject will not be considered in this thesis. In the studied events, nuclei behave as thermodynamical systems in liquid-like phase.

### 1.1.3 Peripheral and semiperipheral collisions

#### Mean field energy region

Around the grazing value the reactions have mainly a binary character. In particular, the main reaction mechanisms are quasi-elastic scattering and Deep Inelastic

Collisions (DIC). In the first case, the interaction between the projectile and the target is minimal. The target ions aren't excited enough to be usually detected. The projectile decays to its ground state emitting  $\gamma$ -rays from low lying states or also some nucleons if it is excited above separation energies.

Towards less peripheral collisions, the interaction between projectile and target increases and nucleon exchanges between them become more relevant. The two reacting nuclei acquire larger and larger excitations (both internal and collective) and start emitting particles and gammas. Therefore in the exit channel we can find a quasi-projectile fragment (QP) and a quasi-target fragment (QT) with characteristics (size and angular distributions) similar to the projectile and target ones respectively, as the name suggests. They re-separate after the collision from a system where a global equilibrium (of internal degrees of freedom) cannot be assumed and then, as two different CN, they decay towards the respective ground state.

For semiperipheral collisions, inelasticity further increases and, especially for not too heavy systems, the formation of a compound nucleus starts to compete with DIC. As the entrance orbital angular momentum is high (it is directly proportional to impact parameter), the CN can reach high spin states and thus fission can be the favourite decay mode.

### Fermi energy region

At Fermi energies, the probability to emit particles or fragments from the di-nuclear (still interacting) complex grows. In DIC events and along with QP, QT and evaporated particles, also intermediate mass fragments (IMF) with  $3 \leq Z \leq 12$  can be emitted at velocities between the projectile and the target ones. The origin of this IMF emission in the intermediate region between the major fragments (neck emission) is a matter of debate; while there is some interpretation based on statistical arguments [9], in most cases it is argued that this emission is of dynamical nature [10]. As we will see in Chapter 4, in our energy region the neck emission is an extremely rare event, as indicated by dynamical simulations, that show only one event of this kind on ten thousand.

Toward higher energy collisions ( $E_b \gtrsim 50$  MeV/u), the N-N interactions prevail, thus only a portion of the colliding nuclei reacts. In the exit channel the projectile-like and the target-like fragments (PLF and TLF respectively) can be found almost not excited (spectator fragments), while a fireball is found in the overlapping region.

### 1.1.4 Pre-equilibrium emissions

One of our main goals is the study of the evolution of the cross section from peripheral to central collisions, then attempting to describe the experimental findings with the help of a well performing model. Following the schema introduced in the previous paragraphs, at our energy we expect mainly fusion-like reactions (complete or incomplete fusion) for central impact parameters and DIC for peripheral and semiperipheral collisions.

We briefly introduce here what is expected at the investigated energy — from the point of view of pre-equilibrium emissions — basing on some papers found in the literature. We don't aim at a general summary report also because, due to the very large number of papers over a long period, it would be too long and out of the scope of this thesis. Thus we restrict ourselves to cases dealing with medium-mass systems as ours.

Below 10 MeV/u, as a guidance energy limit, most collisions occur without contribution of fast emission. For semiperipheral reactions this means that the two nuclei exchange mass and charge and in this way they gain excitation and spin. After equilibrium is reached (the total excitation is shared on average on all nucleons) the QP and QT flight apart while decaying via evaporation or fission. In central collisions, the absence of preequilibrium emission leads to a CN formed with full linear momentum transfer (LMT): the velocity of the CN before evaporation is exactly that of the centre of mass and its mass and charge take the total system values. This is reported for example by [11] which studied the fusion-fission of  $N = Z$  nuclei ( $^{60}\text{Zn}$  formed in the  $^{36}\text{Ar} + ^{24}\text{Mg}$  reactions) at 5.4 MeV/u.

At energies above 10 MeV/u, although this is not a threshold strictly speaking, the dynamics intervenes more strongly and the time scales of excitation and relaxation of the degrees of freedom overlap. There is a general consensus on this observation as it is signaled for instance in [12]. Therefore, both for binary collisions and in fusion-like reactions, experiments reveal some discrepancies with respect to the simple scenario of two phases. The findings have been many and we cite some of them. Morgestern *et al.* [13] reported that the velocity of the fused system diverges from zero in the centre of mass frame for reactions performed between 10 and 25 MeV/u. In particular, the onset of those anomalies happens earlier for mass asymmetric systems.

Lassen *et al.* [14, 15], presenting systematic results for  $^{40}\text{Ar} + ^{40}\text{Ca}$  from 10 to 30 MeV/u, shows how much pre-equilibrium (PE) emission of protons and neutrons increases and limits the maximum energy available for the CN. This paper is interesting as it gives some guidance also for the systems studied in this work.

Figure 1.3a shows the neutron emission dependence on bombarding energy. Clearly from 15 MeV/u, a fast component is visible, and at our energy (17.7 MeV/u) about 1.5 neutrons should come from pre-equilibrium emissions.

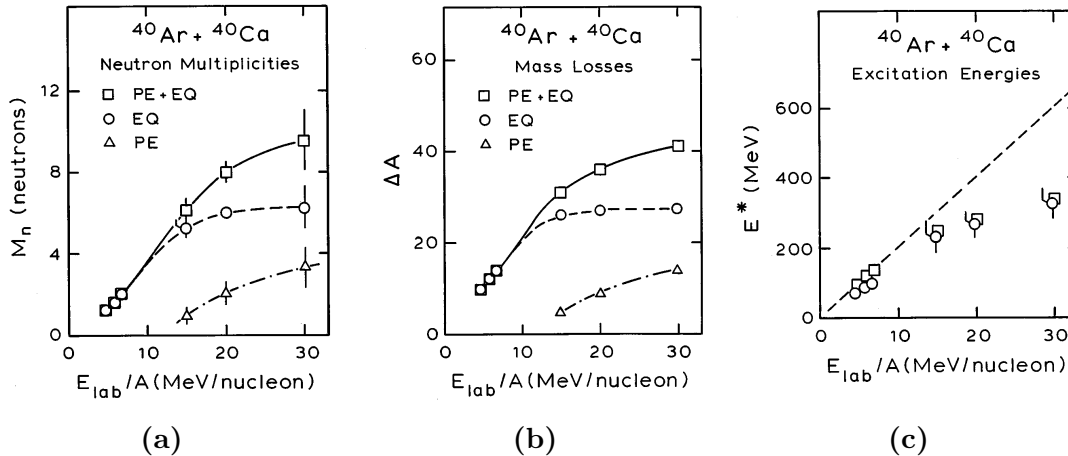


**Figure 1.3:** Pre-equilibrium emission characterization for the reactions  $^{40}\text{Ar} + ^{40}\text{Ca}$  studied by Lassen *et al.* [14]

The total number of nucleons missing in the ER with respect to CN is shown in Figure 1.3b. At about 18 MeV/u we see that 35 nuclear masses can be lost from the CN with  $A = 80$  and 7–8 of them come from PE emissions. This nuclear mass deficit in fusion corresponds to a limit in the energy attained by the system. With increasing  $E_b$  we observe a saturation trend in the value of the CN excitation (Figure 1.3c) due to pre-equilibrium. Interestingly, as the CN mass after the PE decreases faster than the removed energy, the CN energy density still shows a continuous linear trend; at our energy for the  $^{40}\text{Ar} + ^{40}\text{Ca}$  system Lassen suggests  $E^*/A = 3.5$  MeV/u instead than  $E^*/A = 4.2$  MeV/u as it would be in case of full LMT.

Many papers reported on the properties of light charged particles (LCP) — and some of them also on neutrons — measured in coincidence with CN in fusion or binary collisions. The various analyses show that with increasing energy differences appear with respect to the predictions of statistical model assuming no pre-equilibrium. The differences mainly concerns the yields of particles, especially at forward angles, and/or the centre of mass energy spectra, whose shapes are no more compatible with a Maxwellian structure related to a unique slope temperature. An example is shown in Figure 1.4a taken from [16] where energy spectra of LCP measured in coincidence with ER are reported for the reaction  $^{40}\text{Ar} + ^{\text{nat}}\text{Ag}$  at 27 MeV/u bombarding energy. While at large angles, except for  $^3\text{He}$ , the shapes are in fair agreement with the evaporation model (lines), at  $21^\circ$  “shoulders” appear in the spectra, signaling that some other source, beside the assumed CN, is

emitting particles. The authors also give a figure (Figure 1.4b) in which ejectiles multiplicities are shown, separating the cases of pre-equilibrium and statistical emissions. The picture summarizes an investigation on the  $^{40}\text{Ar} + \text{natAg}$  system from 7 to 34 MeV/u. It must be noticed that, according to this finding, at about 18 MeV/u the pre-equilibrium LCP (bottom-right part of Figure 1.4b) represent about 20 % of the thermal emissions.

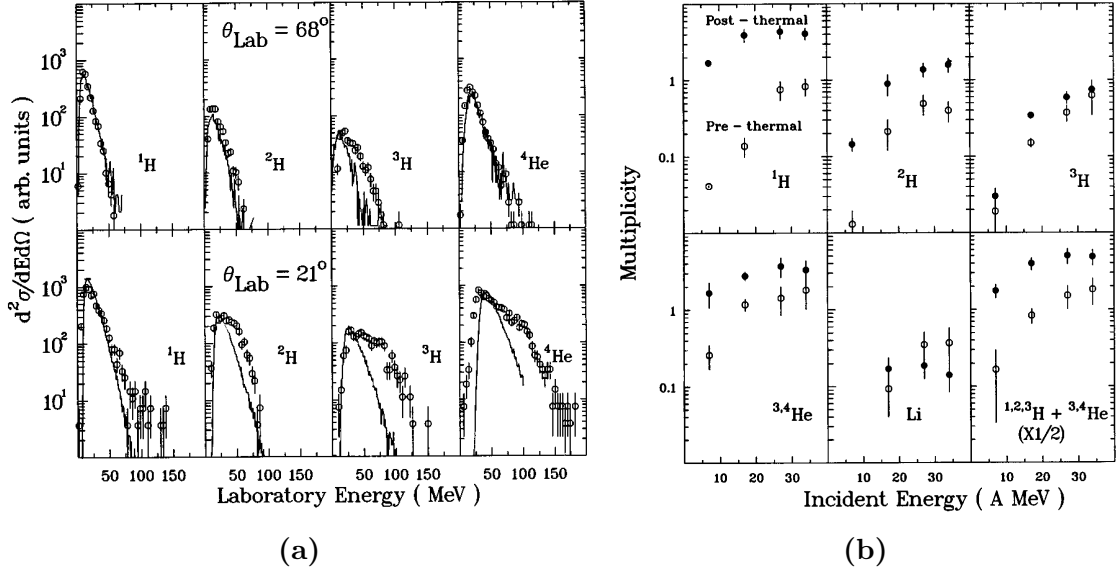


**Figure 1.4:** Pre-equilibrium emission characterization for the reactions  $^{40}\text{Ar} + \text{natAg}$  studied by Magda *et al.* [16]

Summarizing, there is wide and robust evidence for the onset of non-equilibrium effects above 10–12 MeV/u. Such effects should also be present in our data, possibly with some variations between our two studied systems due to the difference of the isospin values. In Chapter 5 we will discuss the data with special care to the various output channels, having the guidance of the statistical model for the decaying sources and a modern well-performing dynamical code describing the system evolution as a function of the reaction impact parameter.

## 1.2 Nuclear matter and the equation of state

Looking at the scenario depicted in the previous paragraphs, it is clear that we are studying a system where the main reaction mechanisms are those typical of the mean field energy regime, but we start to see effects due to nucleus-nucleus collisions. In fact the transition from one body to N-N interaction mechanism is not sharp, but the onset of the typical high energy processes competes with the

progressive disappearance of the low energy ones. So, the energy region of this transition becomes a very productive and challenging field of study in order to understand how, why and under what conditions nuclear matter chooses to follow one or another behaviour. Such a behaviour, in terms of physical observables (like density, temperature, pressure, volume, isospin, . . . ) could be described in terms of an Equation Of State (EoS) of finite nuclear matter: following various trajectories in the phase space, nuclear matter can explore several regions of density, temperature and excitation energy very far from the ground state. Nowadays, the main part of our knowledge regards symmetric nuclear matter at saturation density, so that a lot of efforts are being done toward nuclear matter at extreme condition (and exotic nuclear matter too).

### 1.2.1 Liquid drop model

The Bethe-Weizsäcker formula (Equation 1.1) can be considered the first attempt to describe the nucleus as a thermodynamic system governed by different kind of forces. It was first formulated in 1935 by German physicist Carl Friedrich von Weizsäcker and it is a semi-empirical formula for nuclear masses based partly on theory and partly on empirical measurements. The theory behind the formula is the liquid drop model proposed by George Gamow, which can account for most of the terms in the formula and gives rough estimates for the values of the coefficients. Although refinements have been made to the coefficients over the years, the structure of the formula remains the same today.

The liquid drop model treats the nucleus as a drop of incompressible nuclear fluid. The fluid is made of nucleons (protons and neutrons), which are held together by the strong nuclear force. This is a crude model that doesn't explain all the properties of the nucleus, but it explains the spherical shape of most nuclei in their ground state. It also helps to predict the nuclear binding energy and to establish the energy balance for the reactions (Q-values). The binding energy  $E_B$  can be written in terms of the number of protons ( $Z$ ) and neutrons ( $N$ ) as:

$$E_B = a_V A - a_S A^{2/3} - a_C \frac{Z^2}{A^{1/3}} - a_A \frac{(A - 2Z)^2}{A} - \delta(A, Z) \quad (1.1)$$

where  $A = N + Z$  is the number of nucleons and  $a_V$ ,  $a_S$ ,  $a_C$ ,  $a_A$  and  $\delta(A, Z)$  are parameters. This equation has five terms on its right hand side. These correspond to the cohesive binding of all the nucleons by the strong nuclear force, a surface energy term, the electrostatic mutual repulsion of the protons, an asymmetry term (derivable from the protons and neutrons occupying independent quantum momen-

tum states) and a pairing term (partly derivable from the protons and neutrons occupying independent quantum spin states) respectively. If we consider the sum of the following five types of energies, then the picture of a nucleus as a drop of incompressible liquid roughly accounts for the observed variation of the binding energy of the nucleus.

### 1.2.2 Equation of state of nuclear matter

While the Weizsäcker formula works fine for nuclei in the ground state, it is useless when we are interested in the energy of an excited nucleus. But we can keep the assumption of a thermodynamic system and try to model the excited nucleus as a Fermi-Dirac statistical ensemble. In the equilibrium limit, from the effective interaction one can extract the nuclear equation of state. In particular, at  $T = 0$ , the energy can be written as

$$\rho \frac{E}{A} = 4 \int \frac{d^3p}{h^3} \left( \frac{p^2}{2m} + V(\vec{r}) \right) f(\vec{r}, \vec{p}) = \rho \frac{3}{5} \varepsilon_F + \int_0^\rho \mathcal{U}(\rho') d\rho' \quad (1.2)$$

where in the last part we separated the kinetic and the potential term and we adopted a mean field assumption for the potential. In the previous expression  $E/A$  is the energy per nucleon of nuclear matter at density  $\rho$  and  $\varepsilon_F$  is the Fermi energy depending on  $\rho$ .  $\varepsilon_F \sim 34 \text{ MeV}$  for  $\rho = \rho_0$ , where  $\rho_0 \sim 0.16 \text{ fm}^{-3}$  is the nuclear saturation energy.

The central assumption of the mean field theories is that the nuclear system can be described taking into account the force felt by each nucleon moving independently in an average potential. Since two nucleons interact with each other in presence of many other nucleons, they feel an effective in-medium interaction rather than the bare nucleon-nucleon force. Thus an important task is to find the best analytical form for such effective forces.

At present we are not able to derive a suitable effective nuclear potential directly from the underlying N-N interaction. Data from nucleon-nucleon scattering experiments may be used to identify its functional form and determine which terms are important for describing certain nuclear properties. However, the computational difficulties, related to the nature of the nuclear forces, and the lack of a perfect quantitative agreement with the experimental data make a more phenomenological treatment preferable. Phenomenological effective interactions are therefore commonly used in connection with self-consistent mean fields models: the form of their energy functional is motivated from *ab-initio* theories, but the adjustable parameters are set through systematic fits to the observables of finite nuclei. Currently,

one of the most widely used effective interaction for nuclear matter is the Skyrme interaction [17].

A simplified Skyrme interaction leads to the following form of the mean field potential:

$$\mathcal{U} = \mathcal{A} \left( \frac{\rho(\vec{r})}{\rho_0} \right) + \mathcal{B} \left( \frac{\rho(\vec{r})}{\rho_0} \right)^\sigma \quad (1.3)$$

where  $\rho_0$  is the nuclear saturation density. The first term represents the long-range attraction ( $\mathcal{A} < 0$ ), the second one is repulsive ( $\mathcal{B} > 0$ ) with  $\sigma > 1$  to avoid the collapse of the nuclear system. The values of the parameters  $\mathcal{A}$ ,  $\mathcal{B}$  and  $\sigma$  are adjusted to fit the nuclear matter properties at equilibrium. Putting the expression 1.3 found for the mean field potential inside the Equation 1.2, we obtain the equation of state for symmetric nuclear matter at zero temperature:

$$\frac{E}{A} = \frac{3}{5} \varepsilon_F + \frac{\mathcal{A}}{2} \left( \frac{\rho}{\rho_0} \right) + \frac{\mathcal{B}}{\sigma + 1} \left( \frac{\rho}{\rho_0} \right)^\sigma \quad (1.4)$$

At equilibrium we introduce the compressibility modulus

$$K = 9\rho_0^2 \left( \frac{\partial^2}{\partial \rho^2} \frac{E}{A}(\rho) \right)_{\rho=\rho_0}$$

which is related to the curvature of EoS around the minimum. The EoS (Equation 1.4) depends on three parameters, but only two physical constraints are fixed: the value of the saturation density ( $\rho_0 = 0.16 \text{ fm}^{-3}$ ) and the binding energy per nucleon at  $\rho_0$  ( $E(\rho_0)/A = -16 \text{ MeV}$ ). The third constraint is given by the compressibility modulus whose value is not unequivocally determined. Recent experimental circumstantial results [18] indicated that the EoS is rather soft with a compressibility  $K \sim 200 \text{ MeV}$ . According to the previous constraints, we used a model that adopts the following set of EoS parameters:

$$\mathcal{A} = -356 \text{ MeV} \qquad \mathcal{B} = 303 \text{ MeV} \qquad \sigma = 7/6$$

### 1.2.3 Asymmetric nuclear matter

Today the study of asymmetric nuclear matter is a very active topic in the field of nuclear physics [19, 20]. In fact a better understanding of asymmetric nuclear systems may shed light on many processes, both on subatomic (neutron skin, multifragmentation, neck formation, ...) and on astronomical (supernovae and neutron stars) scales.

The equation of state for asymmetric nuclear matter (*asyEoS*) includes a symmetry term which depends not only on the total density  $\rho$ , but also on the neutron and proton densities  $\rho_n$  and  $\rho_p$  ( $\rho = \rho_n + \rho_p$ ). A key parameter to describe the asymmetric nuclear matter is the asymmetry (or isospin) parameter:

$$I = \frac{(\rho_n - \rho_p)}{\rho} = \frac{N - Z}{A}$$

We want to note that in the literature, especially in experimental papers, the isospin parameter is often defined as  $N/Z$ .

The charge independence of nuclear forces, shown by experimental evidences and confirmed by theoretical calculations, leads to a parabolic form of the *asyEoS* in terms of  $I$ :

$$\frac{E}{A}(\rho, I) = \frac{E}{A}(\rho) + \frac{E_{\text{sym}}}{A}(\rho)I^2$$

The symmetry energy  $E_{\text{sym}}$  includes a potential contribution and a kinetic contribution which can be evaluated and separated, coming directly from Pauli correlations, so we get:

$$\frac{E_{\text{sym}}}{A} = \frac{E_{\text{sym}}^{\text{kin}}}{A} + \frac{E_{\text{sym}}^{\text{pot}}}{A} = \frac{\varepsilon_F}{3} + \frac{C(\rho)}{2} \left( \frac{\rho}{\rho_0} \right) \quad (1.5)$$

where  $C(\rho = \rho_0) \simeq 32 \text{ MeV}$  so that the symmetry energy value at saturation density will reproduce the symmetry term  $a_A$  of the Bethe-Weizsäcker formula (Equation 1.1) which is known from experimental data with reasonable accuracy ( $a_A = 27\text{--}36 \text{ MeV}$ ).

The function  $C(\rho)$  establishes the density dependence of the symmetry potential whose knowledge is still limited far from saturation conditions. There is a large variety of parametrizations for  $C(\rho)$ , coming from macroscopic and phenomenological approaches. While they obviously have the same value at normal conditions, their extrapolations to densities away from saturation are in strong disagreement. An intense theoretical and experimental work has been dedicated to find new observables (§1.2.4) which are sensitive to the density dependence of the symmetry term in order to set some physical constraints on the choice of the more suitable parametrization of the symmetry energy.

In this work we have compared experimental data with simulations (see Chapter 4) performed with different parametrizations of the symmetry energy. In particular we adopted an *asy-stiff EoS*, where the symmetry potential  $E_{\text{sym}}^{\text{pot}}/A$  linearly increases with density, and an *asy-soft EoS*, where the potential shows a saturation

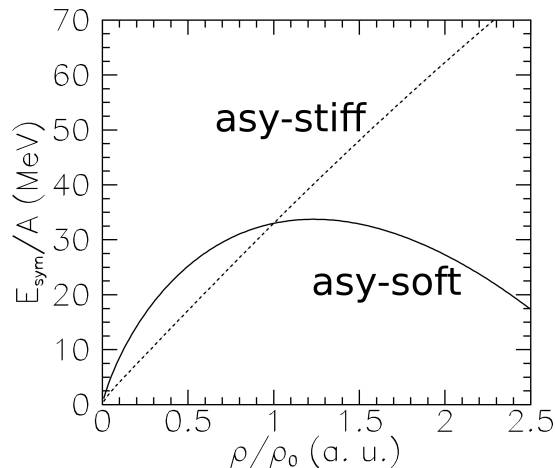


**Figure 1.5:** Density dependence of the symmetry energy for the asy-stiff and asy-soft parametrizations of the EoS.

followed by a decrease above normal density (Figure 1.5). We stress that all the parametrizations have the same saturation properties for symmetric nuclear matter.

#### 1.2.4 Observables related to the isospin

The challenge of any *asyEoS* parametrization is to extend the Equation Of State validity at high temperature or at densities far from  $\rho_0$  [21]. It has been shown theoretically that  $E_{\text{sym}}$  of an excited nucleus may be directly measured in the evaporative regime through the so-called *isoscaling* parameter (related to the ratios between the yields of various isotopes produced in two different reactions involving nuclei with similar mass but different isospin). The same parameter can be used to obtain the density dependence of the symmetry energy in reactions at intermediate energies. Another observable recently proposed [22, 23] is the width of the isotopic distributions of primary fragments which is expected to significantly depend on  $E_{\text{sym}}$  both in case of fragment emission at equilibrium and in case of fragment emission before equilibrium.

The production of strong compression-expansion phase of nuclear systems is a necessary condition to study the EoS far from equilibrium. However, the extraction of quantitative information on  $E_{\text{sym}}$  at finite temperature is challenging: in fact secondary decays of excited primary fragments distort isotopic distributions. On the other hand, it is just accessing the properties of the fragments produced during the interaction (primary fragments whose isotopic content is influenced by the symmetry energy) that the various terms of the nuclear potential and in particular  $C(\rho)$  can be studied in regions far from normal conditions.

We can try to reconstruct the primary distributions from the measured ones using iterative methods and sophisticated techniques [24]. For example, multi-particle correlations can be used to identify in the events particles produced by intermediate decay of nuclei or hot fragments [25]. Alternatively or in a complementary way, we can try to reach the secondary distributions with a two-step simulation. In the first step the primary distributions are generated using nuclear dynamical models including the ingredients that we want to study (e.g.  $E_{\text{sym}}$  and its  $\rho$  dependency). The simulated primary events are then used as sources for a statistical model that simulates the nuclear de-excitation process. This two-step approach is the method that we adopted and it is described in Chapter 4.

The original intent of the experimental campaign described in this thesis was to constrain the  $E_{\text{sym}}$  dependence on density exploiting isotopic distributions of fragments. The idea was that at 17.7 MeV/u the emitted fragments would have a small excitation energy: as a consequence, the secondary distribution would be not too dissimilar from the primary one. However, model simulations showed that after the fragment de-excitation any information on asystiffness of the symmetry energy is lost (see §4.3.4). So the focus of the experiment moved on isospin transport mechanisms.

The main isospin transport mechanisms are the isospin diffusion and isospin drift. The former consists in the equilibration of neutron content between projectile and target during the interaction. The latter produces an excess of neutrons with respect to protons migrating toward diluted regions of nuclear systems during the interaction. An asy-soft EoS gives more repulsion between neutrons and protons at undersaturation densities. Among other effects, it favours pre-equilibrium neutron emission in collisions with n-rich nuclei and isospin diffusion. Differently, an asy-stiff EoS predicts stronger repulsion above saturation densities and shows a larger derivative with respect to density around saturation: this favours the isospin drift.

As isospin drift involves the presence of low density regions (i.e. the neck region in DIC), we cannot observe this phenomenon because at our energies, as we observed in §1.1.3, the neck emission is strongly depressed. Thus, we focused on isospin diffusion by studying the isotopic distribution of the QP in DIC events: we will show in Chapter 5 that there is a small dependence on the target isospin.

We will discuss also the effects of target isospin on pre-equilibrium emission and how much the initial  $N/Z$  asymmetry is preserved in the exit channels. Finally, by extracting cross section values we will give an estimate of the different weights of the exit channels depending on the isospin of the entrance channel. All these kinds of analyses are possible thanks to an experimental apparatus (Chapters 2 and

3) capable of  $A$  discrimination in a huge range of  $Z$  and  $E$ . Moreover, this is the first time that SMF dynamical model (§4.3) ran inside a Monte Carlo simulation over the whole range of impact parameters at this low beam energy and then it was compared to the experimental data.

---

The experimental apparatus

---

As described in Chapter 1, in heavy-ion reactions, different channels are populated with a rich variety of products in a wide range of energies. To efficiently collect products and to well select the various event types a large acceptance detector is needed.

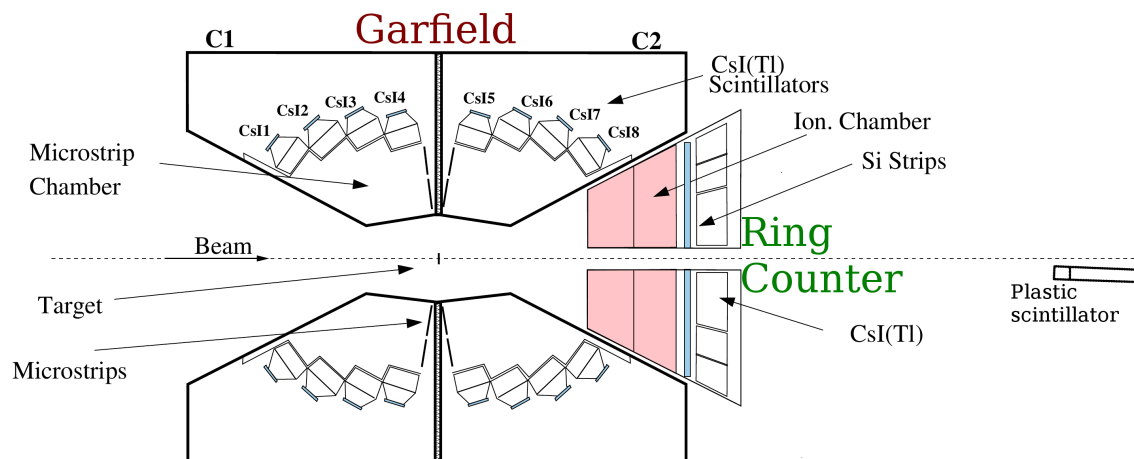


**Figure 2.1:** The detector layout for the studied experiment. GARFIELD surrounds the target while the Ring Counter is mounted at forward angles. A small plastic scintillator at around  $1^\circ$  is used for cross section normalization by means of Rutherford scattering counts.

In the present experiment the charged products from the reactions were measured by the GARFIELD detector (§2.1) [26, 27] complemented with the *Ring Counter*

(RCo) [27, 28] at forward angles. In the very forward cone left free by the RCo (below  $2^\circ$ ), a small plastic scintillator (with a circular active area of 11 mm diameter) was mounted at far distance (2580 mm) to measure elastically diffused beam ions for absolute cross section normalization purposes. In Figure 2.1 a schematic drawing of the whole experimental apparatus is shown.

## 2.1 Garfield

GARFIELD is a multi-detector consisting of two drift chambers (C1 and C2 in Figure 2.1) and it is based on  $\Delta E - E$  modules, equipped with digital electronics. The forward chamber has cylindrical symmetry with respect to the beam axis and it is mechanically divided in 24 azimuthal sectors. Each sector features four CsI(Tl) crystals covering the angular region  $29.5^\circ < \vartheta < 82.5^\circ$ . The scintillators have different shape and dimensions depending on the polar angle  $\vartheta$  (Table 2.1). Furthermore, they are placed in such a way that impinging particles coming from the target enter perpendicularly to the crystal face in its center (Figure 2.2).

	GARFIELD backward				GARFIELD forward			
	CsI-1	CsI-2	CsI-3	CsI-4	CsI-5	CsI-6	CsI-7	CsI-8
$\vartheta_{\min}$	139.9°	127.5°	113.5°	97.5°	68.0°	53.0°	41.0°	29.5°
$\vartheta_{\text{c}}$	145.2°	133.0°	120.0°	104.8°	75.3°	60.0°	47.0°	34.9°
$\vartheta_{\max}$	150.4°	138.5°	126.5°	112.0°	82.5°	66.0°	52.0°	40.0°

**Table 2.1:** Minimum, central and maximum angles corresponding to the regions covered by each GARFIELD CsI(Tl) crystal. The “central” angle indicates the position at which a particle coming from the target impinges perpendicularly to the crystal face.

The forward chamber consists of 96  $\Delta E(\text{gas}) - E(\text{CsI(Tl)})$  modules. The gas volume is unique for all of them and it is filled with flowing  $\text{CF}_4$  at a pressure around 50 mbar.  $\text{CF}_4$  (carbon tetrafluoride) is a stable gas; it is very good for detectors thanks to its high stopping power (five times larger than  $\text{CH}_4$  and 17% more than isobutane), high density ( $3.93 \text{ mg/cm}^3$  at STP) and relatively low cost. Its average ionizing potential is around 16 eV. In our working conditions, considering a typical 10 cm long track in the gas, the  $\Delta E$  stage has a massive thickness of  $1.8 \text{ mg/cm}^2$  corresponding to  $7.7 \mu\text{m}$  of Silicon.

The collecting anodes of the  $\Delta E$  stage, based on metal/glass microstrip technology (Figure 2.4), provide a moderate gas multiplication; while preserving the linear response with deposited energy, the internal gain allows for detection and identifica-

tion (in charge) from  $Z = 2$  to intermediate mass fragments (typically  $Z \sim 15$ ). The  $\Delta E(\text{gas}) - E(\text{CsI(Tl)})$  telescopes are organized in four polar rings corresponding to four CsI(Tl) shapes. There is a CsI(Tl) crystal for each sector in a ring; considering that the drift chamber electrodes are segmented in two independent azimuthal regions, each ring consists of 48 effective  $\Delta E - E$  telescopes, with an azimuthal granularity of  $7.5^\circ$ .

The backward chamber covers the region  $97.5^\circ < \vartheta < 150.4^\circ$  and it has the same structure of the forward one except that 3 sectors are missing (see Figure 2.3), allowing for the mounting of other possible detectors. However, in this experiment the gas stage has not been used and only the CsI(Tl) crystals of the backward chamber have collected data. Indeed, due to kinematics, essentially only light particles can reach angles above  $90^\circ$  in the laboratory frame and these particles can be effectively identified and measured with the only CsI(Tl) scintillators via Pulse Shape Analysis. Although the backward  $\Delta E$  gas stage was not used, it was kept in gas flow at low pressure (20 mbar) in order to provide a sufficient cooling of the CsI(Tl) photodiode preamplifiers that are mounted within the gas volume (“P.A.” in Figure 2.2) without increasing too much the dead layer in front of the scintillators.

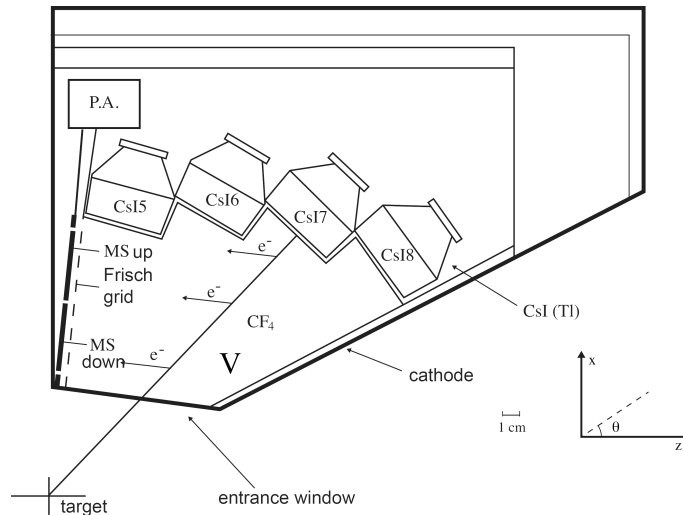


**Figure 2.2:** Lateral schematic view of a  $\Delta E - E$  sector of the GARFIELD chamber.

In summary, the  $\Delta E - E$  telescopes of the forward chamber allowed to detect and identify ions from  $Z = 2$  to around 15. Instead, light charged particles ( $Z = 1$  and  $Z = 2$ ) have been measured via PSA from the CsI(Tl) scintillators ( $96 + 84 = 180$  crystals) of both chambers. The active solid angle covered by the two chambers is around 7.8 sr. The large coverage of the setup is clearly shown in Figure 2.3 where the polar plots of the active solid angle covered by the backward (left) and forward (right) GARFIELD chambers are drawn starting from realistic sim-

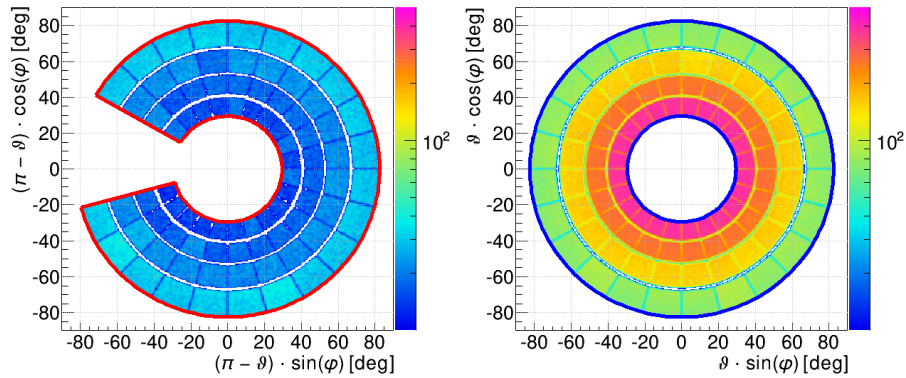


**Figure 2.3:** Polar plots of simulated particles in GARFIELD (§4.5). Left side: backward chamber; right side: forward chamber. The backward chamber has a  $45^\circ$  aperture in  $\varphi$  to allow the mounting of ancillary detectors. CsI(Tl) disposition is easily spotted.

ulated events. The color scale (logarithmic  $z$  axis) evidences the very different yields in the two emispheres. The hole in the backward chamber, where three sectors are lacking, is also well visible.

### 2.1.1 Drift chamber with microstrip electrodes

The drift chamber operating mechanism is relatively simple and it is illustrated in Figure 2.2: a particle produced in the projectile-target interaction, after passing through the entrance window, enters the drift chamber and interacts with the gas contained within it. The energy loss of a charged particle penetrating into a gas is mainly due to two mechanisms, both caused by the Coulomb interaction: the excitation and the ionization of the molecules (or atoms) that constitute the gas. Only in the latter case electron-ion pairs are produced (primary ionization). They represent the charge carriers that can be collected on the electrodes if some drift field is created in the gas volume. The average number of electron-ion pairs produced by the particle is given by  $\Delta E/W$ , where  $\Delta E$  is the particle total kinetic energy lost in the gas and  $W$  is the average kinetic energy spent to generate a pair ( $W = 54$  eV for  $\text{CF}_4$ ). Along their path to the electrodes, the electrons ( $\delta$ -rays) can gain a kinetic energy larger than the gas ionization energy; thus they themselves can create other pairs (secondary ionization) [29].

GARFIELD chambers have a  $6 \mu\text{m}$  thick ( $0.78 \text{ mg/cm}^2$ ) mylar entrance window with thin metallic deposited strips (see below). This thickness keeps low the window dead layer while maintaining a safe mechanical robustness to sustain the pressure deformations. As said, the drift chamber gas is  $\text{CF}_4$ , which has a high stopping power and therefore allows to work at relatively low pressures ( $\sim 50$  mbar). The gas circulates in a closed circuit system and it is forced to flow in a continuous

cycle (the time required for a total replacement is of the order of minutes), with the purpose of eliminating any impurity and contamination such as, for example, molecules produced by the  $\text{CF}_4$  breaking or oxygen and water vapor infiltrations.

Inside the drift chamber a cathode at around  $-1000\text{ V}$  and a Frisch grid (at  $60\text{ V}$ ) generate an electrical field oriented in a transverse direction with respect to the trajectory of the particles. Since the cathode and the grid are not parallel (Figure 2.2), the cathode is not a single equipotential electrode, but it is composed of many strips kept at the proper voltages via a resistive divider to make the electric field as homogeneous as possible. There are electrodes put at different potential via resistive dividers (scaled taking into account the irregular shape of the chamber) also on the front and side surfaces of the various CsI crystals and on the entrance window. These electrodes keep uniform the electric field so that electrons move at constant drift velocity; the speed of the electrons is about three orders of magnitude higher than the speed of the ions, which move in the opposite direction to reach the cathode. Typical values of electric field inside the GARFIELD chamber are of the order of  $10^4\text{ V/m}$ . With these numbers, considering the selected gas pressure, the electron drift velocity is about  $\sim 10\text{ cm}/\mu\text{s}$  (more details in Fig. 10 from [30]).

The Frisch grid is a dense Nickel wire mesh (wire diameter:  $30\text{ }\mu\text{m}$  and mesh pitch:  $1/20\text{ in}$ ; the geometric transparency of the grid is about  $95\%$ ). Behind it, about  $3\text{ mm}$  away, the microstrip plane is placed. The Frisch grid delimits a region close to the microstrips in which the electric field reaches a much greater intensity than in any other part of the chamber and enough to start the multiplication effect. It also prevents the induction of signals on the microstrips when charge carriers drift in the active gas volume and it eliminates the positive ions contribution to the signals.

The microstrip pads (Figure 2.4) have a trapezoidal shape (with dimensions of approximately  $4\text{ cm}$  for the larger base,  $2\text{ cm}$  for the smaller base and  $7\text{ cm}$  for the height) and each is divided into four zones, indicated conventionally with  $ul$ ,  $ur$ ,  $dl$  and  $dr$ . The letters  $u$ ,  $d$ ,  $l$  and  $r$  stand for *up*, *down*, *left* and *right* when one looks at the glass pads with the small base downward. So the two *down* areas are those closest to the beam, while the two *up* are the furthest. The microstrip are made with photolithographic techniques, by depositing thin metal tracks on an insulating glass substrate. An alternation of anodic and cathodic strips is thus realized; their width is respectively  $10\text{ }\mu\text{m}$  and  $85\text{--}190\text{ }\mu\text{m}$  (the width of cathodic tracks varies to follow the trapezoidal shape of the pad). The distance between the tracks ( $50\text{ }\mu\text{m}$ ) is constant to ensure the periodic invariance of the electric field. Unlike the most common use of microstrips, where each anodic track provides an independent signal,

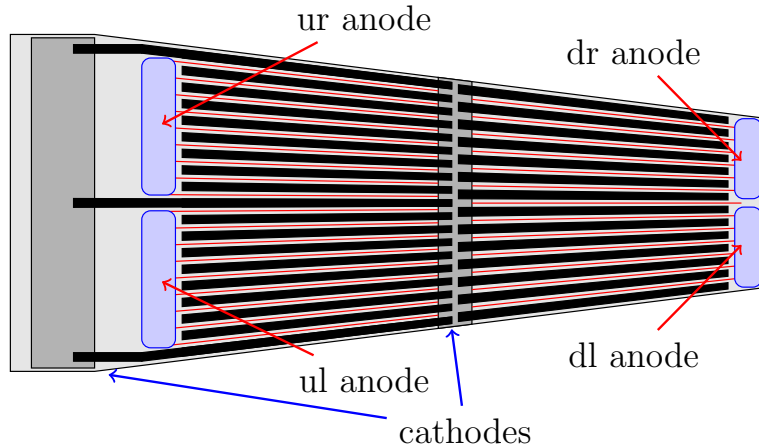


**Figure 2.4:** Schematic representation of a GARFIELD microstrip in which the four electrically separated regions can be distinguished.

for each of the four areas ( $ul$ ,  $ur$ ,  $dl$  and  $dr$ ) the anodes are connected to form a single electrode. So we have four anodic output signals for each microstrip, while cathodes are all grounded.

As said, when the electrons arrive in proximity of the microstrips (at a distance of about  $500\ \mu\text{m}$ ), the non-uniform intense electric field causes an avalanche multiplication. At the chosen gas pressure and microstrip bias voltages ( $+420\ \text{V}$  anodes, grounded cathodes), the device is operating in proportional mode and so the number of collected electrons is directly proportional to the number of primary electrons. As it has been said, the number of primary electrons is in turn proportional to the energy deposited in the gas by the particle. So the output signal results to be roughly proportional to this energy (see §3.3).

### 2.1.2 CsI(Tl) crystals

If a particle has sufficient kinetic energy to traverse the gas stage, it reaches the CsI(Tl) crystal where it loses its remaining energy.

Thallium doped Cesium Iodide scintillators are commonly used as last-stage detectors in a telescope because of their high stopping power (even the most energetic light charged particles in our typical reactions are stopped) and their moderate cost. In addition to stopping power, CsI(Tl) scintillators are characterized by good energy resolution (about 3–4% when detecting  $5.5\ \text{MeV}$   $\alpha$ -particles emitted by a  $^{241}\text{Am}$  source), negligible degradation after prolonged irradiation, low hygroscopic level and ease of cutting and machining.

An advantage of CsI(Tl) detectors is the possibility to perform pulse shape analysis (PSA) for detected particles. This possibility comes from the fact that the

scintillation of the CsI(Tl) crystal is well described by the sum of two exponentials with different time constants: a short one ( $\tau_s \sim 0.75 \mu\text{s}$ ) and a long one ( $\tau_l \sim 5 \mu\text{s}$ ). So the current pulse produced in the photodiode by the scintillation light is described by:

$$i_L(t) \equiv \frac{dQ_L(t)}{dt} = \frac{Q_s}{\tau_s} e^{-t/\tau_s} + \frac{Q_l}{\tau_l} e^{-t/\tau_l} \quad (2.1)$$

where  $Q_L(t)$  is the whole collected charge at time  $t$ ;  $Q_s$  and  $Q_l$  are the charges produced respectively by short and long components of scintillation.  $Q_L$  is thus given by:

$$Q_L \equiv \int_0^\infty \frac{dQ_L(t)}{dt} dt = Q_s + Q_l \quad (2.2)$$

Particle identification capability comes from the different charge and mass dependence of  $Q_s$  and  $Q_l$  components. Also  $\tau_s$  and  $\tau_l$  values slightly depend on charge and mass of the particle. In general, with the same total charge, the short component grows when  $Z$  increases. By means of two shapers with different shaping constants it is possible to determine the intensity of the two components and so to perform PSA. In GARFIELD and in the RCo these different shaping operations have been implemented directly on the digital electronic card (§2.3) purposely designed for our setup [31].

The GARFIELD crystals have variable thicknesses of about 3–4 cm and are able to stop protons and  $\alpha$ -particles with energies up to  $\sim 100 \text{ MeV/u}$ . Each crystal is wrapped in a white diffusive paper and finally protected with an opaque layer to avoid light penetration from outside. This is an additional  $1.5 \mu\text{m}$  thick dead layer to be considered when reconstructing the original energy of particles from the residual energy. The rear part of the crystal is tapered to behave as light guide and it narrows to reach the dimensions of the photodiode coupled to the crystal. This photodiode is the model S3204-05 manufactured by Hamamatsu, with an active area of  $18 \text{ mm} \times 18 \text{ mm}$ . The choice of using photodiodes in place of photomultiplier tubes is due to their greater stability, low power dissipation, much smaller size and to their low bias voltage ( $\sim 100 \text{ V}$ ) which makes possible the operation inside the GARFIELD low pressure gas chamber.

## 2.2 Ring Counter

The Ring Counter is a device that, like GARFIELD, uses PSA and the  $\Delta E - E$  telescope techniques to identify particles. However, it is structured in three different stages (instead of two) in order to identify particles in a greater range of masses and energies. The first stage is an ionization chamber (IC). Segmented Silicon detectors take place behind the chamber. Finally, the third stage is composed of CsI(Tl) crystals. During the measurement, the Ring Counter is inserted just in the forward cone of the GARFIELD metallic cage and its entrance window is placed 177 mm far from the target. Covered polar angles are in the range  $5.4^\circ < \vartheta < 17.0^\circ$ .

The Ring Counter has a cylindrical symmetry along the beam axis and it is divided into 8 azimuthal sectors. Each sector thus covers  $45^\circ$  in  $\varphi$  (azimuthal coordinate). The ionization chamber is of the axial type with electric field parallel to the ion tracks in the gas. There are three electrodes made of aluminized mylar: the two input-output electrodes are the grounded anodes, while the cathode is a central foil with metal deposition on both faces. The mylar anodes act also as gas windows and are metallized only on the internal face. Since the cathode is in between the two anodes, its voltage can be kept halved (150 V in our case) with respect to a geometry with only two electrodes for the same gas gap. The anodes are azimuthally divided in eight parts in order to follow the 8-sector partition of the RCo in the  $\varphi$  coordinate. As in GARFIELD, the gas used for the chamber is the carbon tetrafluoride ( $\text{CF}_4$ ), maintained at a pressure of 50 mbar and in continuous flow. With this pressure value the IC has an active thickness of  $1.1 \text{ mg/cm}^2$ . This active layer is substantially equal to the dead layer introduced by the three mylar electrodes ( $7.5 \mu\text{m}$  corresponding to about  $1 \text{ mg/cm}^2$ ).

	str. 1	str. 2	str. 3	str. 4	str. 5	str. 6	str. 7	str. 8
$\vartheta_{\min}$	$15.6^\circ$	$14.2^\circ$	$12.9^\circ$	$11.5^\circ$	$10.1^\circ$	$8.6^\circ$	$7.2^\circ$	$5.4^\circ$
$\vartheta_{\max}$	$17.0^\circ$	$15.6^\circ$	$14.2^\circ$	$12.8^\circ$	$11.4^\circ$	$10.0^\circ$	$8.6^\circ$	$7.2^\circ$

**Table 2.2:** Minimum and maximum angles defining the regions covered by the Ring Counter Silicon strips according to the design. Each strip detector covers about  $45^\circ$  in the azimuthal coordinate.

A trapezoidal  $300 \mu\text{m}$  thick Silicon pad, segmented into eight strips (Figure 2.5), is placed behind each IC sector. Starting from the experiment of this thesis, Silicon detectors are built from neutron transmutation doped (nTD) material to have a high doping uniformity; moreover, they are reverse mounted, namely oriented in such a way that the particles impinge on the ohmic side. This mounting has been proved

by the FAZIA group to improve the fragment discrimination capabilities by means of PSA [32]. Table 2.2 shows the polar angle intervals at which each strip is located.

Finally, for each sector, there are 6 CsI(Tl) crystals read by a photodiode (model S2744-08 manufactured by Hamamatsu) with active area  $10\text{ mm} \times 18\text{ mm}$ . Therefore, we have 48 Cesium Iodide crystals, each one covering half sector in the azimuthal coordinate. So the azimuth angle of particles reaching the scintillators is known with an accuracy of  $22.5^\circ$ .

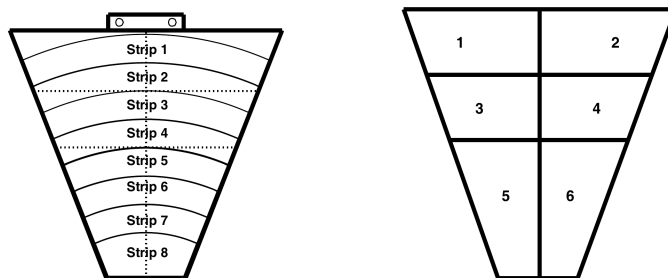


**Figure 2.5:** Ring Counter Silicon strip arrangement compared with CsI(Tl) crystals.

The designed overlap between Silicon pads and CsI(Tl) crystals is well illustrated in Figure 2.5. Part of CsI 1,2 are obscured by the supporting structure of the RCo ionization chamber in correspondence of the non active area of Silicon pads beyond strip 1. Thus, particles reaching only CsI crystals out of any Si strips are forbidden according to the design. From the figure one can also see that at least two Silicon strips correspond to each crystal. Moreover, the geometry introduces some marginal overlap between Si strips and CsI(Tl). For example, the strip 2 has a very small area overlapping CsI 3 and 4. In some cases the border between two couples of crystals (i.e. 3, 4 and 5, 6) is tangent the circular limit between two strips (i.e. 4 and 5). Unfortunately, in practice, due to small geometrical mismatches and to Si border effects, a minority of not well detected particles whose tracks correspond to some detector borders (i.e. particles passing through strip 5 and CsI 3 or 4, that should not be detected according to Figure 2.5) have been found.

In summary, the solid angle covered by the Ring Counter is  $0.25\text{ sr}$  and it corresponds to 30% of the forward cone from  $0^\circ$  to  $29.5^\circ$  not covered by GARFIELD. In Figure 2.6 a polar representation of all the Ring Counter detectors is shown.

## 2.3 The electronics

In the experimental setup, the various detectors (except the GARFIELD drift chamber) were equipped with electronics featuring digital stages. The signals from all the

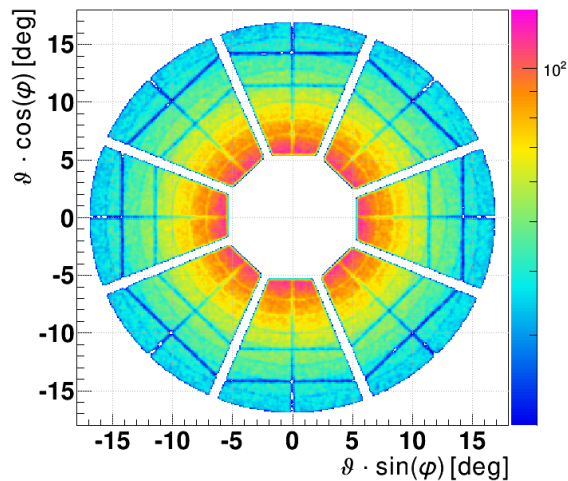


**Figure 2.6:** Polar plot of simulated particles (see §4.5). Silicon strips and Cesium Iodide crystal disposition is easily spotted.

detectors were processed by charge sensitive preamplifiers with different gain. The outputs of these preamplifiers feed the digital cards — developed within the collaboration by the Florence group — containing a 125 MHz, 12 bit ADC (*Analog-to-Digital Converter*) and a DSP (*Digital Signal Processor*). The DSP is programmable and it is capable to perform advanced on-line data reduction [31]. It substitutes the charge amplifier and the peak sensing ADC that were present in the old “analogic” chain. Instead of sending all the digitized samples to acquisition, the DSP elaborates the data and reduces them applying some algorithms (mainly filtering and shaping). In any case, every 1000 events the DSP sends a complete waveform to acquisition for further off-line checks and debugging analysis.

### 2.3.1 DSP algorithms

The DSP is programmed to extract for each detector the absolute maximum of the signal, the baseline value (BL) and the signal amplitude, that is the maximum of the shaped signal, as it is described below. The calculation of those values starts when a trigger validation arrives (see §2.3.2). When it happens, the content of a circular buffer (pre-trigger samples) is transferred to a FIFO memory in which is then stored the actual signal. Overall 8192 samples — of which 512 before the trigger — are saved on the FIFO. Then, about 2000 samples (16  $\mu$ s) are transferred to the DSP: 256 samples ( $\sim 2 \mu$ s) among the pre-trigger ones are used to calculate the baseline, while the maximum is searched inside an interval of 1100 samples (8.8  $\mu$ s) starting from sample n.420. Then the signal (after BL subtraction) is convoluted with a semi-gaussian shaper to extract the signal amplitude. The filter was implemented

with the aim of faithfully reproducing the behaviour of the CAEN N568 module, that was the amplifier previously adopted for the GARFIELD analogic chain. The chosen peaking time for all the detectors was 6  $\mu\text{s}$ .

DSPs associated to CsI(Tl) crystals implement a function that extracts also a fast shaped signal amplitude. The fast shaper is again a semi-gaussian filter but with a shorter peaking time (700 ns) with respect to the “slow” shaper used for signal amplitude calculation. These two different integrations of the signal allow to exploit Pulse Shape Analysis (see §3.2.1). In Figure 2.7 two examples of acquired waveforms are shown. The windows for baseline and maximum search are reported along with the shaped signals.

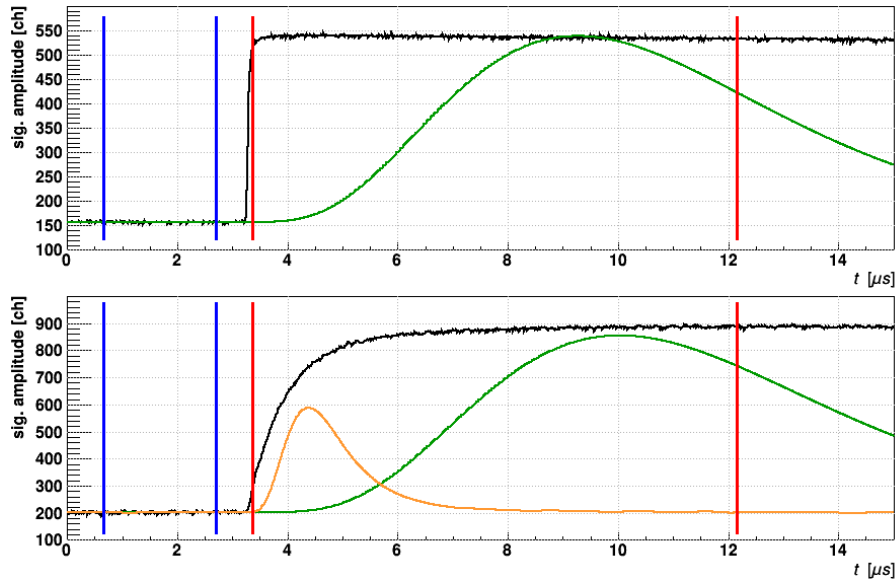


**Figure 2.7:** Typical waveforms acquired by our digital modules (black lines). In the top panel a Ring Counter Si detector waveform is shown (sector 2, strip 4) while in the bottom panel a waveform from a GARFIELD CsI(Tl) crystal (sector 14, Cesium 8) is drawn. The time windows represent the search interval for baseline (blue) and maximum (red). Green curves show the shaped signal with the semi-gaussian filter implemented inside the DSP. In the bottom panel the orange curve shows the fast shaped signal for PSA.

Moreover, each DSP stores four samples around 25% of the maximum signal amplitude. These points are used in an off-line analysis to extract a time mark by cubic interpolation [33]. The time mark is relative to the “start” given by the trigger, and thus it is common to all fired detectors in an event. The DSPs associated to Silicon detectors take into account also other four signal samples, around 75% of the maximum, to estimate off-line a second time mark. This latter, together with the 25% level time, gives the charge signal risetime (labelled as  $Qt_{\text{rise}}$ ), which is a pulse shape parameter needed for particle identification (§3.2.1).

As said before, all the above described variables are calculated by each DSP only when a trigger validation arrives. Then, the signal amplitude value is compared with a user adjustable threshold (acquisition threshold), to decide whether to send all the stored data to acquisition.

### 2.3.2 Trigger and acquisition

The DSPs send the data to acquisition only when a validation signal arrives and the acquisition threshold is exceeded. The validation is generated by the trigger-box CAEN V1495, which is a VME standard electronic board, featuring a field-programmable logic array (FPGA), specifically programmed to perform coincidence and trigger handling tasks.

As said before, for each channel, the acquisition threshold determines whether a signal has to be acquired or not. Beside that, there is the possibility to set another threshold on the signal to start a local trigger when exceeded. In particular we could set the trigger threshold and obtain local triggers from GARFIELD CsI(Tl) crystals (forward chamber only), from Ring Counter Si detectors and from the small plastic scintillator used for cross section normalization.

The trigger-box collects all the local triggers and performs some logical operations to decide whether to send a validation signal. In particular it queries a user defined table of possible combinations of local triggers inside specific time windows. The logical conditions on triggers and the time windows are editable by the user during the measurement.

To exploit at its best the assigned limited beam time, trigger considerations for data acquisition are important. If we acquired everything coming from the detectors, most of the data would be useless events. For example, the elastic and quasi-elastic scattering rates — although the most forward Silicon ring is masked — would be still too high if a minimum bias trigger (only one particle in whatever detector) dominated. Moreover, taking into account that during the acquisition of an event it is not possible to start acquisition of another event, we would also have a relevant dead time. Thus, we have to select the best trigger conditions in order to reduce dead time and to acquire mostly interesting events.

Inside the trigger-box, up to eight different trigger combinations can be programmed. From now on, we will refer to those primary eight combinations simply as “triggers”. The trigger-box output is a bitmask that indicates which trigger was activated (each bit is a specific trigger). A trigger could also be reduced by a factor  $f$ , so it will be activated only one time every  $f$  occurrences.

In Table 2.3 trigger bits and reduction, along with their description, are reported

bit	trigger	reduction	description
0	various	var.	Varied during experiment
1	Garf	200	OR among all GARFIELD scintillators
2	Garf & Strip1-7	1	AND between trigger 1 and 7
3	$M \geq 2$	-	At least 2 GARFIELD scintillators
4	$M \geq 3$	1	At least 3 GARFIELD scintillators
5	Plastic	200	Plastic scintillator
6	Pulser	-	PB-5 Pulser
7	Strip1-7	10	OR among RCo strips 1–7

**Table 2.3:** The available triggers with their reduction factors adopted during physics measurement. Detailed description in the text.

as used in the experimental campaign described in this work. Depending on the specific run, different triggers have been used. For example, during a pulser run (see §3.1.3), only trigger 6 was selected with a reduction factor of 1 (that means no reduction at all). During the main physics measurement we adopted the reduction factors reported in the table. The main trigger (the less reduced one) is the number 2, that selects events with at least a hit in a GARFIELD CsI(Tl) and one in a RCo Si strip (the ring of strips 8 have been excluded because they were blinded, see §3.5.2). The multiplicity triggers 3 and 4 were implemented for selecting high multiplicity events (candidates for multifragmentation) and have not been used here. Thus, at the end, inside the analysis tool we adopted two triggers:

**trigger 2** main physics trigger to perform the largest part of the analysis;

**trigger 5** to register elastic scattering events inside the plastic scintillator in order to normalize counts to the absolute cross sections;



---

### Calibrations and particle identification

---

Our collaboration developed in the last years a powerful framework to calibrate the data: ODIE. It consists of a database for calibration parameters and of several routines used to elaborate raw data. ODIE output is a ROOT tree containing calibrated data.

### **3.1 Preliminary operations**

#### **3.1.1 Bad signal rejection**

The first step of the data reduction has been the removal of signals originated from noise or disturbances that however exceeded the on-line detection thresholds. In the case of DSP signals (§2.3), the noise removal is done by putting specific conditions on baseline and signal maximum. In particular, considering that 12 bit samples assume values in the range 0–4095, the baseline must be within a reasonable interval of values (10–2000) and the maximum of the charge signal must not exceed 4095 (overflow) but however being larger than the baseline.

#### **3.1.2 Garfield microstrip angular calibration**

Our detectors are in general not position sensitive and the angular resolution is in fact given by the detector granularity. Only the GARFIELD drift chambers, thanks to the measurable drift time of the tracks (§2.1.1), can give in principle the polar angle with 1–2 degree precision. This result, however, is applicable only above a

minimum deposited energy in the gas. This can introduce biases in the analysis (position would be determined only for some particles) and therefore in this work the drift time option has been disregarded.

From now on we state that the positions of the particles (i.e. their emission angles) correspond to the known angles of the detector they hit. In particular, in the analysis we can select two options:

1. the position of a particle is the center of the active area;
2. the position of a particle is randomly extracted on the active area of the hit detector.

The second choice is the default option of our analysis.

### 3.1.3 Pulser run

Pre-amplification electronics is sensitive to environmental conditions, mainly temperature variations; thus the gain may slightly change over time. It is a common practice to test the electronic stability and linearity from time to time by using a pulser. The pulser is a signal generator that produces pulses similar to the ones produced by the detectors. These pulses enter the pre-amplifiers in the same way the detector signals do. We used the pulser model BNC PB-5 followed by a series of passive splitters to fan-out the signal for each pre-amplifier.

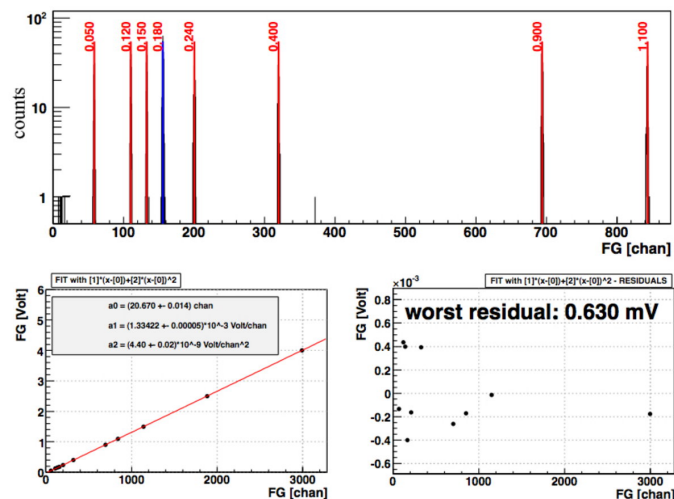


**Figure 3.1:** A typical pulser run check. Ten different peaks are acquired from time to time to check the electronics stability and linearity of each channel of GARFIELD and of the Ring Counter.

In Figure 3.1 an example of fit of pulser peaks is shown. During our whole experiment eight pulser runs have been performed. They have been used to verify the electronic stability. We found no significant variations of the gain (all the fluctuations were below the 1%) and no corrections have been applied accordingly.

## 3.2 Particle identification

The particle identification (PID) is particularly important in this study and I devoted much effort in this calibration phase. The importance originates firstly from the goal of the experiment that is the study of how the reaction properties (fragment nature and abundances, reaction channel sharing) could change with changing the isotopic target composition. It is obvious that particle recognition is at the basis of this kind of search. A second important aspect of PID is technical: the measured energy of a particle is in general a fraction of the initial energy due to the passage of different dead layers. The dead layer energy loss correction is a procedure that needs the knowledge of  $Z$  (and possibly  $A$ ) of the particles as the loss depends on the specific ion. For this reason ion identification must be performed before energy calibration; in this respect the electronic stability check described in the previous paragraph assumes its importance. In fact to better identify the particles we need to sum lots of non calibrated runs and so the preamplifier gains must have been stable for all the measurement.

In experimental heavy-ion physics several identification methods are adopted. The most frequently used are the  $\Delta E - E$  technique, the pulse shape analysis (PSA), and the  $E - \text{tof}$  correlation. We briefly introduce all these methods, specially referring to our detectors. For each kind of correlation we extracted  $Z$  (and  $A$  where possible) by applying graphical cuts and/or by interpolating between clicked lines over the ridges corresponding to different atomic species.

### 3.2.1 Particle identification techniques

#### $\Delta E - E$ technique

When a nucleus goes through a material it loses energy (see §3.4.1). The energy loss is quite well described by the Bethe-Bloch formula, whose important dependencies in the non relativistic limit are:

$$-\frac{dE}{dx} \propto \frac{Z^2 Z_m}{v^2 A_m} \quad (3.1)$$

where  $Z$  and  $v$  are the particle charge number and velocity respectively, while  $Z_m$  and  $A_m$  are the charge and mass numbers of the absorbing material. If this latter is a compound, the energy loss is the average of partial  $-dE/dx$  (one for each atomic species in the absorber) weighted with partial molar masses. Because  $v^2 = 2E/m$ , for a fixed material we have that

$$-\frac{dE}{dx} \propto \frac{Z^2 A}{E}$$

So the energy loss inside a material strongly increases with the impinging particle charge and slightly with its mass, while it decreases with energy.

Exploiting the Bethe-Bloch formula it is then possible to identify particles by putting two different detectors one behind the other: the first one must be entirely crossed by the ion, which is then stopped in the second layer. The correlation between the energy released inside the first detector ( $\Delta E$ ) and the residual energy ( $E_{res}$ ) shows different ridges for each atomic species (Figures 3.2 and 3.4) and, if the detectors have sufficient energy resolution, also isotopes can be discriminated (Figure 3.6).

### Pulse shape analysis (PSA)

The details of the process of energy deposition within detectors are at the basis of PSA. For example, in Silicon detectors, for a fixed energy of the impinging particles, heavier ions tend to create more electron-hole couples and they tend to form a plasma region in which the electric field is weaker. So the charge collecting process lasts longer and correspondingly the charge signal risetime is longer. As previously said (§2.1.2), also in CsI(Tl) scintillators the light output depends on the impinging ion charge and mass. Then, for this kind of detectors, it is possible to extract PID information using only one layer by studying the signal shape. In particular, for Silicon detectors the *energy* vs. *risetime* correlation is usually adopted. In scintillators, instead, the *fast* vs. *slow* technique is used: *fast* and *slow* are the values of the charge signal maximum obtained with two different shaping constants (a short and a long one respectively) to enhance the differences between the contributions related to the two characteristic scintillation time constants  $\tau_s$  and  $\tau_l$ .

Of course, there are limits in the applicability of PSA in detectors when the particle tracks are modestly penetrating in the active volume (i.e. toward low deposited energies). For example, according to detailed studies of the FAZIA group [32] charge identification for light ions in Silicon is prevented for ion range lower than 30  $\mu\text{m}$ .

### Energy versus time of flight

Using fast response detectors and sufficiently long flight path for the emitted particles, some mass identification can be obtained via  $E$  vs. time of flight (*tof*) correlations. In our case the flight paths are short because GARFIELD and Ring Counter are mounted close to the target. For example, in the RCo, a Zinc ion ( $Z = 30$ ) travelling at the velocity of the centre of mass (as can occur after a fusion event), that is 25.8 mm/ns for the  $^{32}\text{S} + ^{40}\text{Ca}$  reaction, needs only  $\sim 10$  ns to reach the Silicon wall. With such short times any ion discrimination is impossible taking into account that beam pulsing resolution is usually worse than 1 ns. For this reason no timing information has been used in this thesis.

We can still use the time mark as it can be obtained by applying a digital constant fraction discriminator to the various detector signals (not caring too much of the time resolution, so we didn't correct for the synchronization of the different electronic channels) to order in time the particles and to reject on this basis, at least partially, the spurious ones. This has been possible taking into account that we run the experiment with a pulsed beam, as said, having time resolution of about 2 ns over a period of 200 ns.

#### 3.2.2 Identification techniques in Garfield

In the previous chapter the experimental apparatus has been described. In particular, GARFIELD has been introduced as a  $\Delta E - E$  telescope array where the drift chamber constitutes the  $\Delta E$  layer while the residual energy is collected by CsI(Tl) crystals. An example of typical  $\Delta E - E$  correlation in GARFIELD is shown in Figure 3.2 for the reaction  $^{32}\text{S} + ^{40}\text{Ca}$ . Since the gas resolution is not excellent (about 5–6%) and the tracks have not the same length for a given Cesium (see Figure 2.2), isotopes cannot be discriminated. However, thanks to the very low energy threshold typical of gas detectors, even very slow ions up to  $Z = 16$  can be identified, with a threshold that depends on  $Z$  (from 2 MeV/u for  $Z = 3$  up to 3.5 MeV/u for  $Z = 16$ ).

From the formula 3.1 it is easy to see that light charged particles don't lose much energy in materials with respect to a heavier ion with the same initial energy. So the signal coming from the GARFIELD drift chamber for Hydrogen and high energy Helium isotopes is comparable to noise and  $\Delta E - E$  technique cannot be used. Thus we adopted the PSA in CsI(Tl) crystals to identify protons, deuterons, tritons,  $^3\text{He}$  and  $^4\text{He}$  isotopes. This identification method introduces a relatively high energy threshold, but permits to have mass discrimination. In Figure 3.3 a

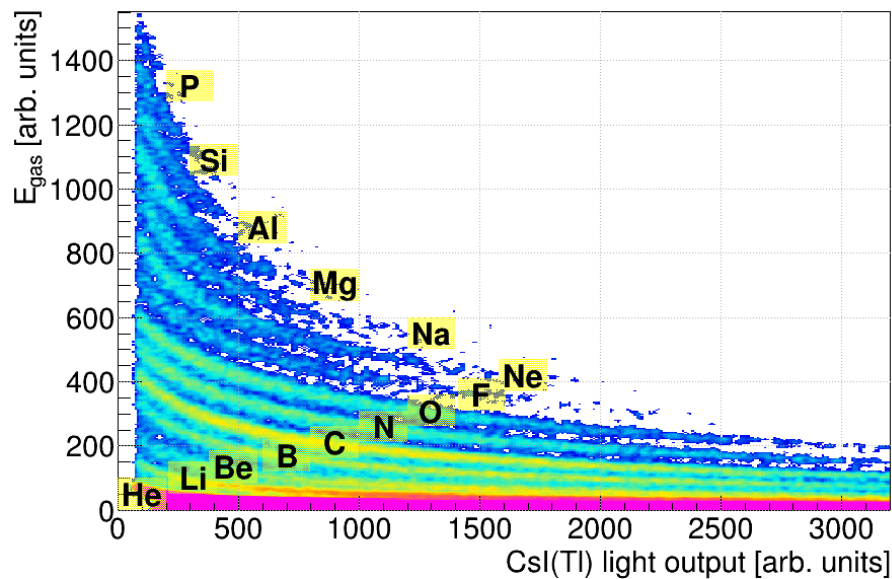


**Figure 3.2:** Typical  $\Delta E - E$  correlation in GARFIELD for the reaction  $^{32}\text{S} + ^{40}\text{Ca}$ . Ions can be discriminated from  $Z = 2$  up to  $Z = 15$ .

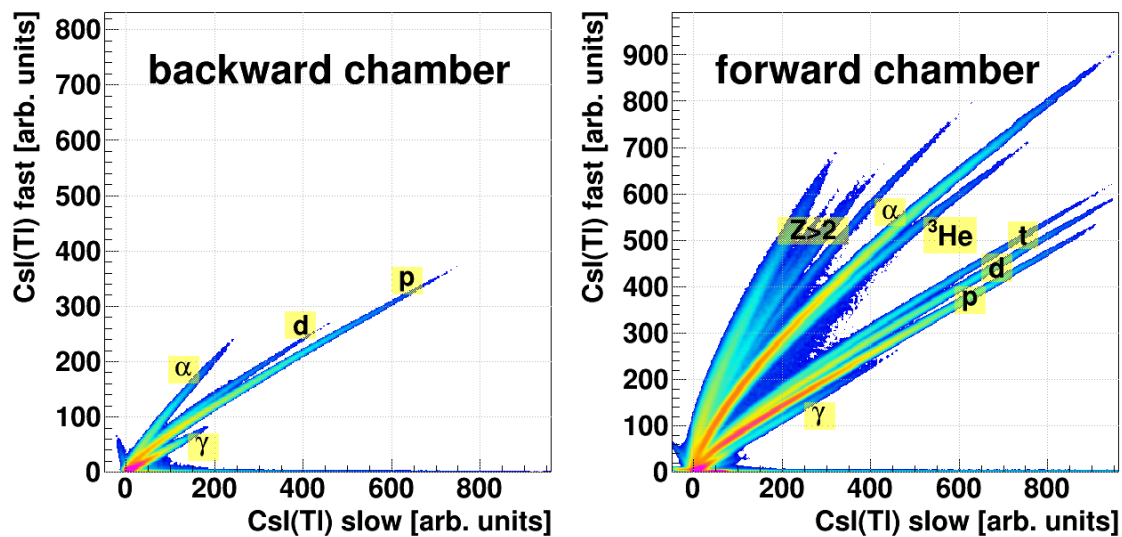


**Figure 3.3:** Typical *fast* vs. *slow* correlations in the GARFIELD Csl(Tl) crystals. Left panel: sector 14, CsI 3 (backward chamber). Right panel: sector 14, CsI 8 (forward chamber). In both cases Hydrogen and Helium isotopes can be distinguished.

typical *fast vs. slow* plot is shown. To recover low energy Helium isotopes that cannot be identified with PSA, we used  $\Delta E - E$  correlation, considering that for He ions with  $5 \text{ MeV} < E < 10 \text{ MeV}$  sufficient energy is released in the gas stage.

$Z$	ID	$E$ range	isotopic ID
1	CsI PSA	$>3 \text{ MeV}$	✓
2	CsI PSA	$>8 \text{ MeV}$	✓
	$\Delta E - E$	$5\text{--}10 \text{ MeV}$	-
3–12	$\Delta E - E$	$>2\text{--}3 \text{ MeV/u}$	-

**Table 3.1:** Summary of GARFIELD forward chamber identification capabilities. In the backward chamber only the CsI PSA method is used.

Intermediate mass fragments and heavy particles cannot reach the backward chamber for kinematic reasons. In fact, looking at the left panel of Figure 3.3 we can see that heavy particles region in the *fast vs. slow* correlation of a backward CsI(Tl) crystal is empty. Thus only PSA in the scintillators was used and only Hydrogen and Helium isotopes were identified. As already said, to reduce energy thresholds, gas pressure has been kept low (at about 20 mbar) during the experiment. In Table 3.1 the GARFIELD identification limits are summarized.

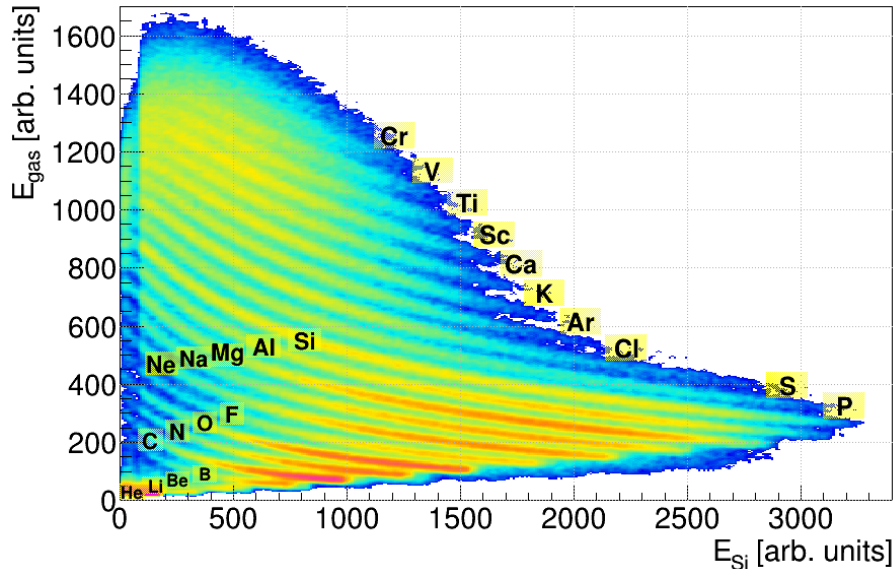


**Figure 3.4:** Typical  $\Delta E - E$  correlation in Ring Counter between IC and Si (sector 2, strip 4). In this case ions can be clearly discriminated from  $Z = 4$  up to  $Z = 24$ . The plot is done with the condition that no CsI(Tl) crystal behind the considered Si strip gave a signal. For small Silicon signals, a trigger threshold effect is clearly visible.

### 3.2.3 Identification techniques in the Ring Counter

Particles impinging on the Ring Counter are on average more energetic with respect to ions going in GARFIELD because the Ring Counter is located at forward angles and the centre-of-mass velocity boost is summed to all reaction products. For this reason energy thresholds are in general less critical and even Phosphorus ions ( $Z = 15$ ) can reach the third detector layer. However, there are heavy and slow reaction

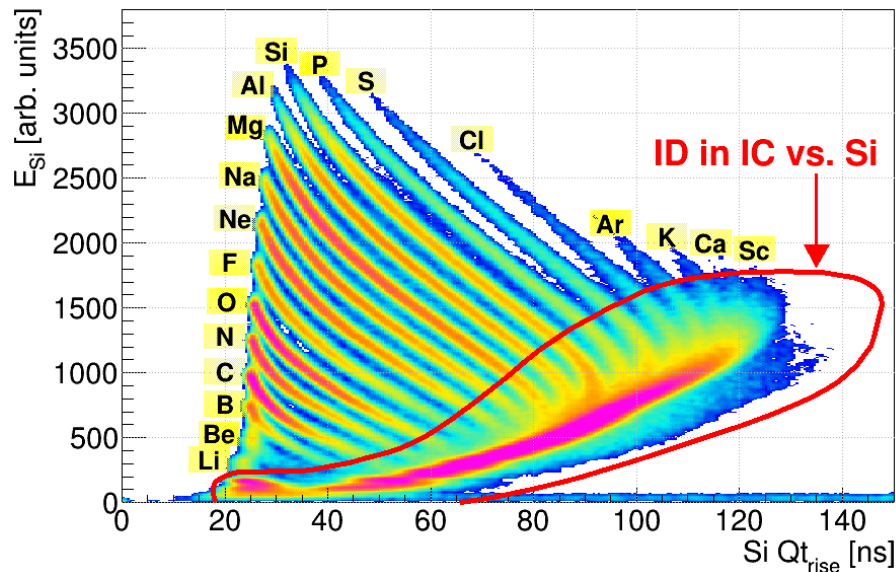


**Figure 3.5:** Typical PSA for ions stopped in a Ring Counter Si detector (sector 2, strip 4). Discrimination is feasible from  $Z = 4$  up to  $Z = 20$ . The plot is done with the condition that no CsI(Tl) crystal behind the considered Si strip gave a signal. The ions with too low energy in Silicon, not enough for good PSA, are shown inside a graphical cut. For these particles  $\Delta E - E$  (IC-Si) identification is adopted (Figure 3.4).

fragments for which the threshold is an issue. Specifically, evaporation residues, slow quasi-target fragments from DIC and kinetically disadvantaged fission fragments could not reach the CsI(Tl) scintillators (last layer of the telescope), so they can be identified by means of  $\Delta E - E$  technique in IC-Si (Figure 3.4) and by means of PSA (Figure 3.5) in Silicon pads when a sufficient range is traversed by the ions. Combining PSA and  $\Delta E - E$  methods we are able to identify particles ranging from  $Z = 4$  up to about  $Z = 30$ , but isotopic discrimination cannot be obtained. If both the identification methods are feasible, we use the information from PSA.

For more energetic particles, like quasi-projectiles, kinematically favourite fission fragments and light charged particles, we use the  $\Delta E - E$  correlation (Figure 3.6) between Silicon and CsI(Tl) detectors. Thanks to the high energy resolution of Silicon detectors, we are able to discriminate charge and mass of all particles from  $Z = 1$ . Due to kinematics we observed particles stopping in the scintillators up

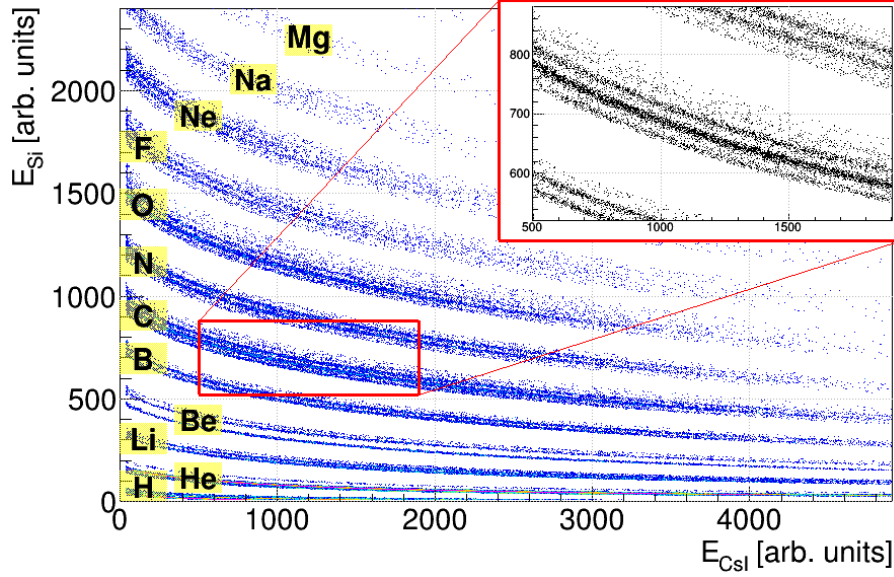


**Figure 3.6:** Typical  $\Delta E(\text{Si}) - E(\text{CsI})$  correlation in a Ring Counter telescope. In this particular case (sector 2, strip 4, cesium 4) ions can be identified from  $Z = 1$  up to  $Z = 13$ . We obtain isotopic discrimination (detailed for  $Z = 6$  in the inset) for all particles identified with this method.

$Z$	ID	$E$ range	isotopic ID
1	CsI PSA	$>10$ MeV	✓
	Si-CsI	6–60 MeV	✓
2–3	Si-CsI	$>6-7$ MeV/u	✓
4–15	Si-CsI	$>9-15$ MeV/u	✓
	Si PSA	from 3–5 to 9–15 MeV/u	-
	IC-Si	from 1.5 to 9–15 MeV/u	-
16–20	Si PSA	$>5$ MeV/u	-
	IC-Si	$>1.5$ MeV/u	-
21–30	IC-Si	$>1.5$ MeV/u	-

**Table 3.2:** Summary of RCo identification capabilities. Energy threshold for Si-CsI ion identification depends on  $Z$  (from 6 MeV/u for  $Z = 1$  up to 15 MeV/u for  $Z = 15$ ).

to  $Z = 15$  for the inner Silicon strips and up to  $Z = 11$  for outer strips. For most energetic protons, the  $\Delta E - E$  method is not exploitable because the energy released in the Silicon pad is below the acquisition threshold defined in §2.3.1. So, in that case, we use the *fast vs. slow* correlation in CsI(Tl) crystals to recover the identification information. In summary, Ring Counter identification limits are shown in Table 3.2.

### 3.3 Energy calibration

The next important step in data processing is the energy calibration. This step is relatively easy for nearly linear detectors such as the GARFIELD microstrips, the Ring Counter ionization chamber and the Silicon detectors. For this kind of detectors, in principle, the energy calibration can be done by associating the peak position of the energy spectrum with the known deposited energy for specific particles in specific events (typically elastic scattering reactions). For this purpose during the experiment we performed some runs with a  $^{197}\text{Au}$  target to increase the reaction grazing angle (to  $18^\circ$ ) in order to have elastically scattered projectiles with enough count rate into the maximum number of detectors. We considered also other older measurements — performed with the same gain — and we used the calculated deposited energy for elastic scattering to calibrate all the detectors. For example, for Silicon detectors a single calibration factor is extracted from a linear fit of several measured centers of elastic scattering peaks (expressed in channels) as a function of their calculated value (in MeV). In the next paragraphs the more complex calibration techniques adopted for CsI(Tl) and gas detectors are discussed.

#### 3.3.1 Energy calibration of the Garfield CsI(Tl) crystals

The light output (LO) of CsI(Tl) scintillators is not proportional to the released energy and the literature reports on many different attempts, from empirical to more funded recipes, to obtain the conversion from LO to deposited energy. For example, we cite [34] where a very accurate study of the energy, charge and mass dependence of the LO was performed. However, the formula presented there is very complicated and it involves a high CPU usage. For this reason our collaboration adopted a simpler semi-empirical expression, deduced from experiments at Legnaro purposely devoted to CsI calibrations [35]. The formula reads:

$$LO(Z_{eff}, E) = (d_1 + d_2 e^{-d_3 Z_{eff}}) (1 + d_4 Z_{eff}) E^{d_5 - d_6} \exp(-d_7 Z_{eff}) \quad (3.2)$$

The parameters in the functional were fixed thanks to spectra obtained from many Coulomb scattering conditions where the various LO peak positions were easily associated with the calculated deposited energy for various ions. The experiments show that the main non-linearity is found for  $E/A < 10.5$  MeV/u, where  $A$  is the ion mass. Above this empirical value, the  $E$  dependence of LO is linear with angular coefficient equal to the derivative of the Equation 3.2 at this threshold. Using  $Z_{eff} = (AZ^2)^{1/3}$  permits to better take in account the charge and mass dependence of the light output [35, 36].

The described formula permits to know the energy dependence of the acquired CsI(Tl) signal apart from an overall normalization factor depending on the electronic gain. This constant, for each CsI, has been deduced using the elastic scattering peak energy converted to LO using Equation 3.2. The factor is obtained by the ratio between this value and the experimental one in channels.

### 3.3.2 Energy calibration of Ring Counter CsI(Tl) crystals

The Equation 3.2 was specifically obtained for the GARFIELD CsI(Tl) crystals and it is not a priori guaranteed to work fine for other crystals that may have different Tl doping rates and different shapes, wrapping materials and photodiodes. In any case we tried to correlate the experimentally obtained light output with the predicted one obtained by reconstruction of particle energy loss in each detector layer (and then converting CsI(Tl) energy to LO using Equation 3.2). This procedure can be performed thanks to the previous energy calibration in Si for identified ions. More precisely, to an identified particle which stops in CsI is assigned an energy loss in Si. From these data and by the known traversed layers, using energy loss tables, we deduce the energy deposited in CsI which is finally converted in LO by means of Equation 3.2. If the functional works fine, a linear correlation should be found. This is the result for ions with  $Z \geq 2$  (Figure 3.7b), while we had to modify the functional for  $Z = 1$  as can be seen in Figure 3.7a. Specifically, we used a parabola under 1000 ch to take into account the non linearity observed for small energy releases of Hydrogen in CsI with respect to the Equation 3.2.

### 3.3.3 Energy calibration of gas detectors

Both gas detectors used in this experiment — the GARFIELD drift chamber and the Ring Counter ionization chamber — operate in a propotional regime, that means that the signal amplitude is propotional to the deposited energy. So, if we identify an elastic scattering peak in an energy spectrum, it is very simple to obtain the

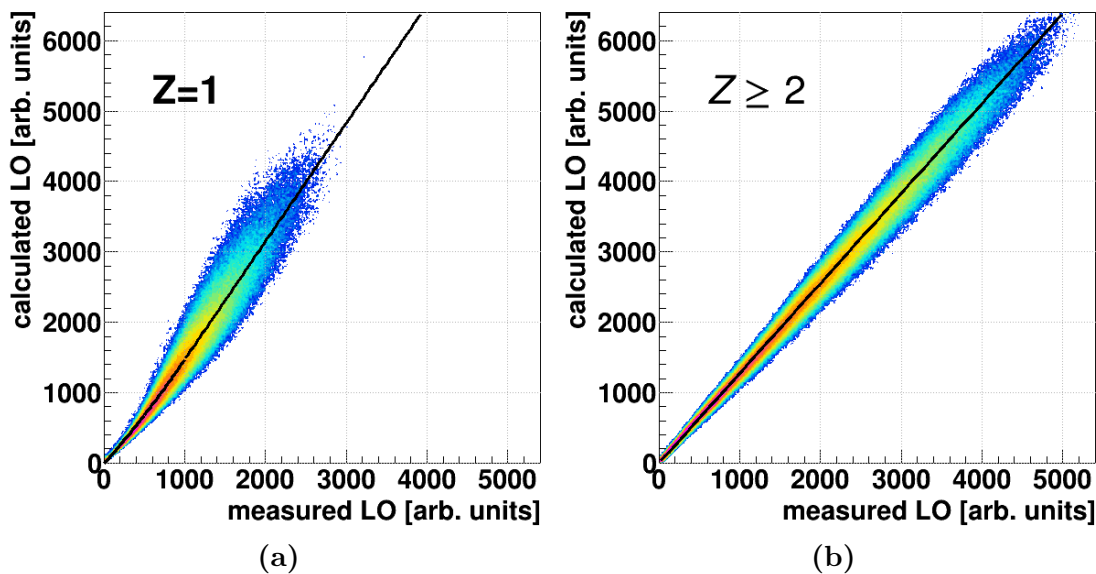


**Figure 3.7:** Different energy calibration functions between  $Z = 1$  and  $Z \geq 2$  ions in RCo CsI(Tl) crystals. In the former case a parabola jointed to a straight line is used, while only a straight line passing through the origin is used in the latter case. The functions convert the measured values of light output to the energy equivalent expressed in term of LO from the equation 3.2.

calibration factor to convert the acquired amplitude in channels to an energy scale. However, usually the elastic scattered ions have high energy and so they release only small fractions of it inside the gas volume. This implies a large relative uncertainty on the signal amplitude of the elastic peak signal. Moreover, due to the peculiar geometry of the GARFIELD chamber, in this case the electric field is not exactly homogeneous in every part. This implies small inhomogeneities in energy calibration (that depends on  $\vartheta$  and  $\varphi$ ).

For all the previous reasons the gas calibrations were performed taking advantage of the predicted energy loss. Knowing the ion species and their residual energy (in CsI(Tl) for GARFIELD, in Si for RCo), we reconstructed the energy loss inside the gas and we correlated that value with the measured signal amplitude, of course taking into account the effective dead layers encountered by the ions along their tracks. With this method we obtained different calibration parameters for each GARFIELD/RCo sector ( $\varphi$ ) and GARFIELD ring/RCo strip ( $\vartheta$ ). In particular we adopted a second order polynomial fit and so we obtained three calibration parameters per detector. We notice that this procedure takes into account the expected residual non-linearities and at our best uses all the available information (many ions at various energies) to estimate the calibration parameters, instead of fixing a conversion MeV/ch factor with a few specific energy/ion combinations (as it would be

using elastic scattering).

## 3.4 Refinement of energy loss calculations

The determination of the kinetic energy of the heavy products is important in this work and in particular for ions detected in the RCo. Heavy and relatively slow fragments are produced mainly in fusion reactions when an evaporation residue flights at forward angles with almost the centre-of-mass velocity. In our systems, in case of complete fusion, this corresponds to Kr nuclei ( $Z = 36$ ,  $A = 72, 80$ ) with velocities around 25 mm/ns and thus energies around 250 MeV. On the other hand, the fission of a source formed in central collisions can lead to one fragment emitted backward in the centre-of-mass frame, again this resulting in low laboratory velocities, thus high energy losses in the IC. We remark that for these heavy products the wrong kinetic energy determination causes a sizeable systematic error on the energy (momentum) balance of the event.

In practice, in the  $\Delta E - E$  spectra (Figure 3.4), we observe evaporation residues up to  $Z \simeq 28$  because they originate from fusion-like processes and then they evaporate many particles. For a typical  $Z = 24$  evaporation residue with an energy of 100 MeV the energy loss in the IC is 29 MeV and similarly in its mylar electrodes, while the energy released in the Si pad is 38 MeV. So, in the energy reconstruction process, for that kind of fragments the energy released inside the IC is relevant. The effect can be appreciated for the heavy ions in the Figure 3.8a that will be discussed in the following paragraph.

From the above arguments, it follows that a right estimate of the energy losses in the gas (and in the dead layers) is crucial. For this reason I carefully verified this part of the calibration comparing different available formulas and then I implemented a new subroutine to include the recent published results on stopping power in gases.

### 3.4.1 Stopping power in materials

Energy loss models are fundamental to reconstruct the initial ion energy from the partial energies released inside each detector. Stopping power is defined as the retarding force acting on charged particles due to interaction with matter, resulting in loss of particle energy. The stopping power  $S$  of the material is numerically equal to the loss of energy  $E$  per unit path length  $x$ :  $S(E) = -dE/dx$ . The force usually increases toward the end of range and reaches a maximum, the Bragg peak, shortly before the energy drops to zero. The curve that describes the force as function of the material depth is called the Bragg curve. The mean range can be calculated by

integrating the stopping power over energy:

$$\Delta x = \int_0^{E_0} \frac{1}{S(E)} dE$$

where  $E_0$  is the initial kinetic energy of the particle,  $\Delta x$  is the ion range and  $S(E)$  is the stopping power. The deposited energy can be obtained by integrating the stopping power over the entire path length of the ion while it moves in the material.

As generally done, we here consider the stopping power as composed by two terms: electronic ( $S_e$ ) and nuclear ( $S_n$ ) stopping power. At the beginning of the slowing-down process at enough high energies, the ion is slowed down mainly by electronic stopping and it moves almost along a straight path. When the ion has slowed down sufficiently, the collisions with nuclei (the nuclear stopping) become more and more probable, finally dominating the slowing down.

Electronic stopping refers to the slowing down of a projectile ion due to its inelastic collisions with bound electrons in the medium. The term inelastic is used to signify that energy is lost during the process (the collisions may result both in excitations of bound electrons of the medium, and in excitations of the electron cloud of the ion<sup>1</sup> as well). Since the number of collisions an ion experiences with electrons is large, and since the charge state of the ion while traversing the medium may fluctuate, it is very difficult to describe all possible interactions for all possible ion charge states, especially at the end of the range where the charge state fluctuations are larger. Instead, the electronic stopping power is often given as a simple function of energy  $S_e(E)$  which is an average taken over all energy loss processes for different charge states. As introduced before (§3.2.1), an accurate way to consider the electronic energy loss of charged particles is the classic Bethe-Bloch formula (Equation 3.1), found by Hans Bethe in 1930.

As said before, nuclear stopping power refers to the elastic collisions between the projectile ion and atoms in the material, and it is usually negligible except at the lowest energies. For very light ions slowing down in heavy materials, the nuclear stopping is weaker than the electronic one at all energies. To summarize, the total non-relativistic stopping power is therefore the sum of two terms:  $S(E) = S_e(E) + S_n(E)$ .

Several semi-empirical stopping power formulas have been devised. In the past (around the 80s) the most common parametrizations were based on the Northcliffe-Schilling tables [37]. One of these is the formula of Braune and Schwalm used at GSI, that was adapted for the various materials studied and commonly used at that time.

---

<sup>1</sup>if the considered ion is not completely ionized its electrons form a “cloud” around it

The Braune and Schwalm formula was optimized for the energy ranges available at that time (under 20 MeV/u). With the developing of new particle accelerators, the Hubert-Bimbot-Gauvin range tables [38, 39] were proposed. They are however not valid for ions with energy under 2.5 MeV/u. The Hubert tables are the base of the Vedaloss routine [40], largely employed by the INDRA collaboration since the nineties. Vedaloss aims to extend the validity of the tables under the original energy threshold, but this extension is not very accurate for composite absorbers and in general for gases. Finally we mention the model given by Ziegler, Biersack and Littmark, implemented in different versions of the SRIM/TRIM codes [41], which is one of the most used today.

### 3.4.2 Stopping power in gas

While Vedaloss and SRIM codes work very fine for solid materials, one frequently find disagreement when using them to reproduce energy loss in gases. A recent attempt to reproduce the stopping power in gases was carried out by Barbui *et al.* in [42]. They measured the experimental stopping powers for heavy ions in some gases commonly used in detectors over an energy range 0.1–15 MeV/u. At the end they extracted an effective charge parametrization suitable for stopping power calculation and extrapolation to low energy, high  $Z$  ions. Commonly, the parametrization of the effective charge is the crucial point to get a general use  $S(E)$  recipe.

In a given medium, the stopping power  $S$  of an ion can be related to that of a reference ion  $S_{\text{Ref}}$  with the same velocity by the scaling law:

$$\frac{S}{(\gamma Z)^2} = \frac{S_{\text{Ref}}}{Z_{\text{Ref}}^2}$$

where  $\gamma$  is the effective charge fraction of the ion with atomic number  $Z$ . In this equation, the reference ion having atomic number  $Z_{\text{Ref}}$  is assumed to be fully stripped. Hence, the effective charge fraction  $\gamma$  can be defined empirically by

$$\gamma^2 = \frac{S(v, Z, \text{target})/Z^2}{S_{\text{Ref}}(v, Z_{\text{Ref}}, \text{target})/Z_{\text{Ref}}^2}$$

where  $v$  is the ion velocity and “target” labels the stopping material.

The parameterization of the effective charge fraction  $\gamma$  requires the determination of the functional dependence on the variables  $v$ ,  $Z$  and “target”. As said, some such parameterizations have been proposed in the past and used to produce stopping power tabulations. As an example, the Hubert tabulation [39] has been shown

to be very good in reproducing the experimental data of heavy ions in solids. In the Hubert work, the factor  $\gamma$  is a function of the energy per nucleon of the ion ( $E_A = E/A$ ), its atomic number  $Z$  and the atomic number  $Z_T$  of the target:

$$\gamma = 1 - P_0 \exp(-P_1 E_A^{P_2} / Z^{P_3}) \quad (3.3)$$

The dependence of the parameters  $P_0$ ,  $P_1$ ,  $P_2$  and  $P_3$  on the target atomic number  $Z_T$  can be found in [39].  ${}^4\text{He}$  is used as the reference ion and the tabulation is limited to solid stopping materials. The parameterization has a lower energy threshold at 2.5 MeV/u, value above which the assumption of fully electron stripping is quite reasonable. However, Diwan *et al.* [43] found that, for ions with  $3 \leq Z \leq 35$ , the validity of the Hubert formula can be extended into the energy range of 0.5–2.5 MeV/u by properly tuning the parameter  $P_0$ . The values of  $P_1$ ,  $P_2$  and  $P_3$  in 3.3 are kept fixed and  $P_0$  is obtained by a polynomial fit as a function of the projectile atomic number  $Z$ . It is worth mentioning that their parameterization of the effective charge is independent of  $Z_T$ .

Since we are interested in the stopping powers for low energies and high  $Z$  ions, we could think to adopt Diwan parametrization, but this would have not resolved the problem of the gaseous absorbers. Instead, we preferred to follow up the Barbui *et al.* work, that, differently from Diwan *et al.* was developed specifically for gases. It introduces a different parameterization making use of protons as reference ions, since they can be fully stripped at lower energies than  ${}^4\text{He}$  and the proton  $S$  is rather well known in many materials. First of all, Barbui tried to reproduce the experimental proton stopping power in various media using the largely employed and acknowledged SRIM code. While it gave an excellent agreement in  $\text{CH}_4$  and aluminum, some corrections were necessary for mylar and  $\text{CF}_4$ . The empirical  $\gamma$  values were then reproduced using the Equation 3.3 in which:

$$\begin{aligned} P_0 &= p_0 + p_1 \log(Z) & P_2 &= p_2 \\ P_1 &= p_4 + p_5 \log(Z) & P_3 &= p_3 \end{aligned}$$

where  $p_0$ ,  $p_1$ ,  $p_2$ ,  $p_3$ ,  $p_4$ ,  $p_5$  are fitting parameters.

Parameters values are slightly target dependent. In particular, for  $\text{CF}_4$ , Barbui found the following fit results:

$$\begin{aligned} p_0 &= 1.468 & p_1 &= -0.08301 & p_2 &= 0.4039 \\ p_3 &= 0.2965 & p_4 &= 4.615 & p_5 &= -0.71544 \end{aligned}$$

### 3.4.3 Improvements obtained in Ring Counter

During the GARFIELD-RCo energy calibration, the first choice was the Vedraloss routine to calculate energy loss in dead layers and in detectors. For what concerns GARFIELD and Silicon and CsI layers in Ring Counter we never found significant discrepancy between predicted and measured energy loss. For solids this is trivial, while the rather good agreement for the  $\Delta E$  stage of GARFIELD is mainly due to the fact that we didn't detect ions with  $Z > 15$  and to the higher energy thresholds with respect to the Ring Counter. Instead, we observe sizeable mismatches using Vedraloss to calculate the  $E$  loss in RCo, in particular for slow ions with  $Z > 6$  and for all the ions with  $Z \geq 18$ . This is shown in Figure 3.8a where the calculated  $\Delta E - E$  lines are superimposed to the data for the  $^{32}\text{S} + ^{40}\text{Ca}$  reaction: we can notice that for  $Z \geq 21$  there is also a line crossing between adjacent ions. For a Calcium ion ( $Z = 20$ ) that loses 50 MeV in the Si layer, the relative difference between the predicted  $\Delta E$  in IC and the experimental ridge is 6 %.

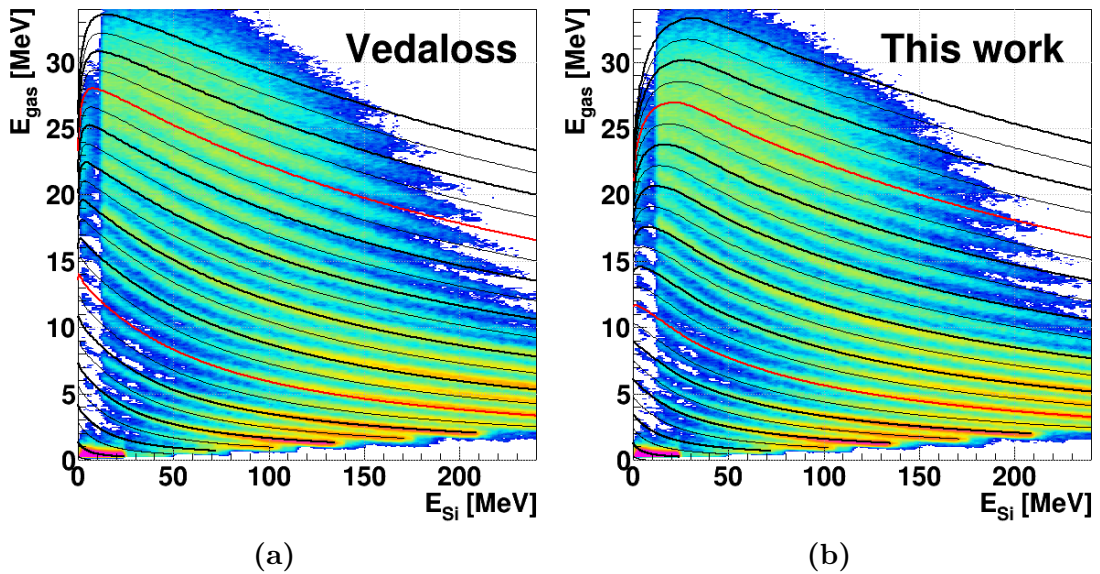


**Figure 3.8:**  $\Delta E - E$  correlation between IC and Si in Ring Counter sector 2, strip 4. Predicted lines for  $1 \leq Z \leq 24$  are overimposed. For eye guidance, the  $Z = 10$  and  $Z = 20$  lines are colored in red. Left panel: lines are calculated with Vedraloss routine. Right panel: lines are calculated with the new routine (see text).

To better reproduce IC energy loss I modified the energy loss calculation. In particular, I wrote a routine that creates a range table for each ion in  $\text{CF}_4$  using the Barbu parametrization for stopping power. The energy-range table allows to reduce calculation time for the event by event analysis. We can see from Figure 3.8b that the agreement at lowest energies definitely improves. In particular there are only small distances between calculated lines and experimental ridges from  $Z \sim 15$ . In

comparison with the Vedaloss calculated lines, for the same Calcium ion that loses 50 MeV in the Si layer, the relative difference between the predicted  $\Delta E$  in IC and the experimental ridge is now 2 %.

## 3.5 Efficiency considerations

Taking into account that GARFIELD+RCo is composed of almost 400 independent electronic channels, it is understandable that some detectors or pre-amplifiers or digital modules didn't work. In some cases no signal was acquired, due to a variety of reasons (broken detector or pre-amplifier, etc...). In other cases, we acquired signals, but affected by too much noise that blurred the identification correlations. In the following paragraphs we specify the inefficiencies in the various modules.

### 3.5.1 Garfield efficiency

Talking about GARFIELD, we didn't use — for particle identification and for total energy calculation — the signals coming from *down* electrodes of the microstrips because they were found to be generally more noisy than those from *up* electrodes. This is possible because the *down* signals were redundant (each particle traversing the gas volume releases energy both in the *down* and in the *up* regions). As we adopt one microstrip  $\Delta E$  signal in correlation with 4 different CsI(Tl) crystals, we have to consider for the efficiency calculation all the combinations between *up* microstrips and Cesium in the forward chamber. A combination is not used if the *up* microstrip signal is not present or the  $\Delta E - E$  correlation is poor and so the particle identification is not permitted. In total we have 5 (out of 48) *up* microstrips which didn't work at all during the experiment, precluding 20 correlations. In addition to those, 14 more combinations were not usable. In total 17 % of correlations (34 out of 192) were not good enough for identification of particles with  $Z > 2$ .

Not all the CsI(Tl) crystals worked, too. In the forward chamber 5 out of 96 crystals gave no signal at all. We excluded 7 more scintillators due to poor resolution. Overall we had 13 % of crystals not working properly. In the backward chamber 12 out of 84 CsI(Tl) didn't have signals and 5 were excluded, so 20 % of the backward crystals were not working properly. The polar plots of the working detectors of GARFIELD are shown in Figure 3.9 and they offer a clear panorama of the experimental efficiency.

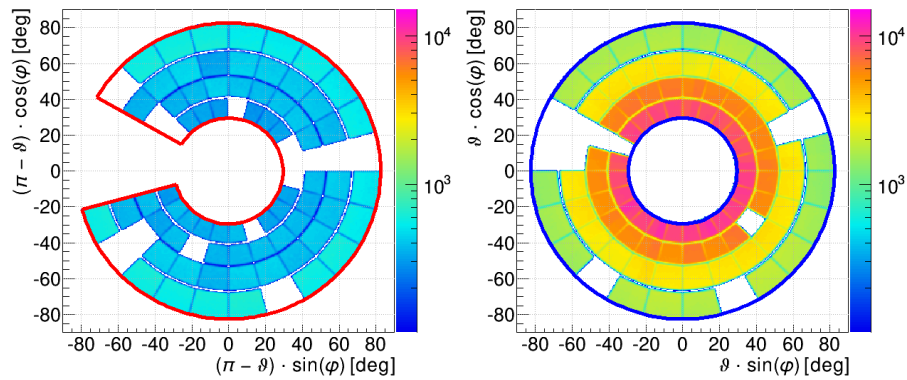


**Figure 3.9:** Polar plots of particles identified in GARFIELD. In the two plots, the detectors not properly working have been excluded causing blank regions.

### 3.5.2 Ring counter efficiency

In the Ring Counter, all the ionization chamber sectors worked properly. As for Silicons we had to exclude the inner Si strip (strip 8), because a metallic shield covered it during the experiment to protect it from radiation damage coming from elastic scattered ions. Then we have also strip 2, 4 and 6 of sector 6 not working because of a wrong connection and strip 1 of sector 5 that gave an anomalous yield and for this reason was removed from the analysis. Overall 19% of Si strips didn't work properly. Finally, all CsI(Tl) crystals responded, but 4 out of 48 had a poor resolution, thus were excluded. The polar plot of the working detectors of RCo is shown in the projection of Figure 3.10.

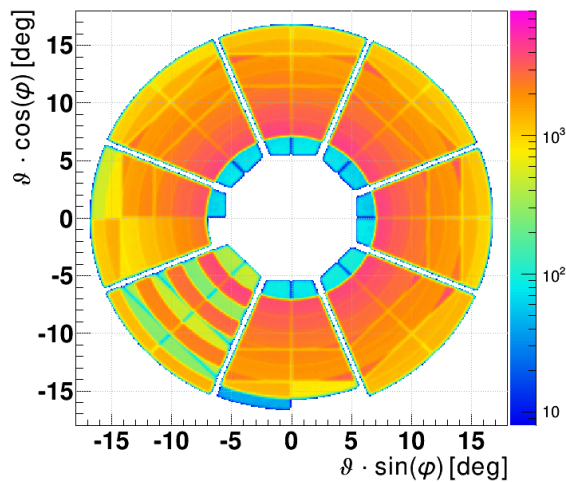


**Figure 3.10:** Polar plot of particles identified in Ring Counter is shown; Not working detectors are also visible, causing blank or blue zones.



---

## Theoretical models and event simulations

---

To understand the physical processes that bring to the fragment emissions and their characteristics, it's fundamental to compare our experimental data with models that can predict the different reaction mechanisms. Many different models have been developed for different kinds of reactions at different energy ranges. We can consider two big classes of nuclear decay models: dynamical and statistical models. The former kind implements an interaction between particles and tracks the system evolution in time. The latter class considers the nuclei as thermodynamical systems at internal equilibrium and decides which and how many particles are emitted to reach the ground state level on the basis of decay rates of different channels and of the available excitation energy and angular momentum.

### 4.1 Dynamical models

The time evolution of a nuclear system is a typical many-body problem. In particular it involves quantum particles, so a quantum treatment is required. However, no analytical solution to the very complicated many-body problem exists and several approximated methods have been developed. Many features of nuclear dynamics with low energy beams (up to  $\sim 10$  MeV/u) can be studied using one-body models, such as the time-dependent Hartree-Fock theory (TDHF), or its classical analog, the Vlasov equation. They aim at following the evolution of the one-body density matrix, which is propagated in a self consistent mean field. This description is reliable as long as the energy is low enough that the residual two-body correlations

can be neglected because they are mostly suppressed by the Pauli blocking towards the final states. At higher energies, the Pauli blocking is less effective and nucleon-nucleon (N-N) collisions need to be incorporated into the dynamical models. In this respect, semi-classical approaches are preferable, because a collision term can be rather easily introduced to take into account two-body correlations.

There are lots of different implementations of dynamical models. Some codes, such as AMD (*Antisymmetrized Molecular Dynamics*) [44], consider each nucleon as a gaussian wave packet. The dynamics during the contact of the reacting heavy-ions is described in terms of the propagation in an effective (mean field) interaction and of hard two-body collisions. The interactions can be between two or more nucleons (many body). Other implementations, like SMF (*Stochastic Mean Field*) [45], consider each nucleon as composed of many test particles and they introduce a phase-space lattice in which the particles are subject to a mean field. In this way, one simulates the time evolution of the one-body distribution function  $f(\vec{r}, \vec{p}, t)$  (classic equivalent of the wave function). In particular, SMF uses the *Boltzmann-Nordheim-Vlasov* (BNV) transport equation, that is substantially the Vlasov equation including the collision term. How this equation is derived from the Schrödinger equation is well described in [46]. To improve the treatment of the two-body interactions within the SMF model, a stochastic term is added to the collision integral (actually projected in coordinate space) to simulate fluctuations from the average evolution.

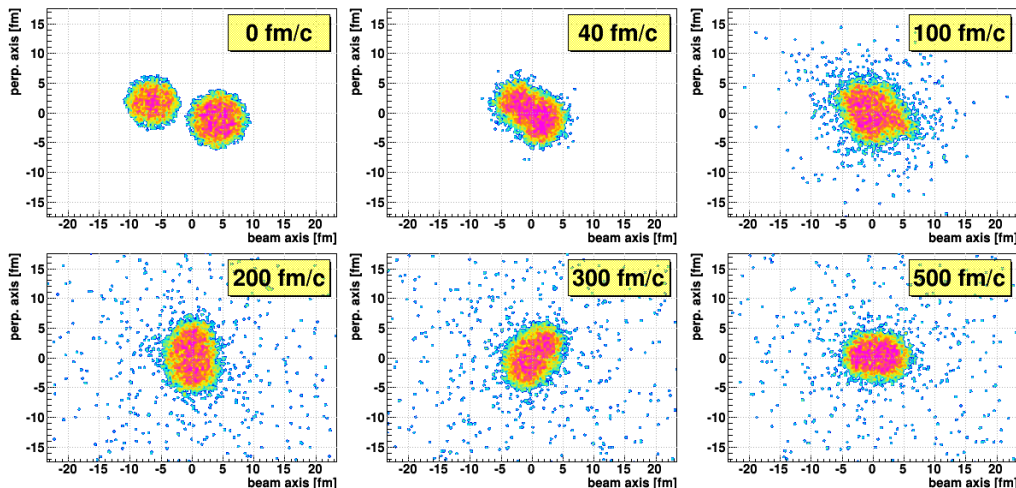


**Figure 4.1:** Example of an event simulated with the TWINGO code for the system  $^{32}\text{S} + ^{48}\text{Ca}$  at 17.7 MeV/u for a rather central collision ( $b = 2.76$  fm). The reaction produces a unique main nucleus (quasi-fusion).

During this thesis we got in touch with the theorists expert in AMD and in SMF models. The collaboration is of course in progress and it's motivated both by the

data presented here and by applications at Fermi energies, now under investigation with the FAZIA telescopes. AMD is particularly suitable for Fermi energies while its extension under 20 MeV/u is not straightforward according to its author. Therefore we limited ourselves to SMF calculations, implemented in the TWINGO code (§4.3). This code, which for this thesis has been implemented in a full Monte Carlo package, is meant to produce the primary fragment distributions for the various impact parameters  $b$ . Primary fragments are the main (hot) ions produced in the reaction, which, after their separation, can decay by emitting particles and  $\gamma$ -rays and/or fissioning (secondary products).

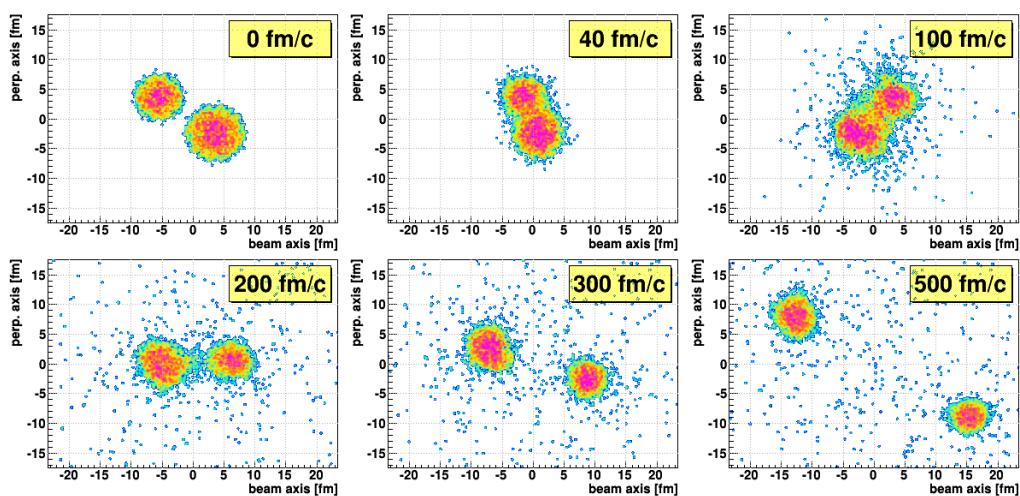


**Figure 4.2:** Example of an event simulated with the TWINGO code for the system  $^{32}\text{S} + ^{48}\text{Ca}$  at 17.7 MeV/u for a semiperipheral collision ( $b = 5.83$  fm). The reaction produces two main nuclei (DIC).

An important effort done during this thesis has been the proper usage of the TWINGO code in a fully “experimental” fashion. This means that events have been produced running the code on a triangular impact parameter distribution from zero to the grazing value, for each S+Ca reaction, in order to populate the primary phase-space in a realistic way. For each event, depending on  $b$ , we get one (Figure 4.1) or two (Figure 4.2) main fragments (fusion or dissipative binary collisions respectively) which are hot and rotating. After the evaporation step (see below) the secondary distributions can be analyzed and filtered as the data and compared to the measured quantities.

We remark that SMF predictions have been largely compared with experimental data but this is the first time, to our knowledge, that the model has been implemented, at this low energy, as a full event generator to be used with just the same experimental data analysis package and covering not a specific interval of impact parameters but the whole range.

## 4.2 Statistical decay

Dynamical models, such as SMF, are used to generate events (in Monte Carlo implementations) or distributions (in general approaches) for the nuclear species which are predicted to originate from the reaction. Let's consider the Monte Carlo approach, which is more useful because it permits to simulate faithfully a true experimental measurement with fragments produced in any event. Each of these fragments is hot ( $E^* > 0$ ) and rotating ( $J > 0$ ). Thus, a so-called “afterburner” is needed to predict the primary fragment de-excitation and to obtain the secondary quantities for a direct comparison with data. An afterburner is nothing else but a statistical model code.

We here remark an important problem in coupling dynamical to statistical models. The separation into two distinct phases (dynamics and statistics) is rather reliable when excitation energies are low (partial widths  $\Gamma_i$  are small) and the lifetimes of the nuclei are long compared to the typical scale of the dynamics. But with increasing bombarding energies and/or excitations, this sharp timescale separation becomes more and more doubtful. So, the user's choice on the separation time between the two phases must be properly verified and circumstantially proved in the various cases. In this work we discuss various afterburner times — from 200 to 500 fm/c — also taking into account a reasonable CPU investment. Longer times are safer considering the equilibrium attainment. In fact, the big sources identified in the dynamical model at 500 fm/c after the beginning of the collision, are more probably the final ones because the residual interactions are definitely over. However, in the application of the dynamical model, test particles are emitted along the time, independently of the attainment of equilibrium. In this respect it would be better to move the freeze-out phase (start of a well performing decay stage) at shorter times. This can conflict with the safe source (fragment) recognition, as at the bombarding energies of this work the dynamics is not so fast and the fragments could not be clearly defined. Below in this chapter (§4.3) we will discuss in details this subject.

We here explicitly note an aspect of the use of the statistical model to investigate our data. The expression “compound nucleus” usually refers to nuclei formed in a fusion like process, as it was indeed observed in our data for central collisions. However, the statistical decay of CN is supposed to occur for many other sources — big and medium size fragments — which are produced during the interaction. For example, the CN formation is also assumed for quasi-projectiles, i.e. excited Sulphur-like nuclei produced in binary collisions; similarly, we can assume that in fission each of the two primary fragments is a compound nucleus whose decay can

be described by a statistical code.

In this work we used the statistical model GEMINI++ (§4.4) to describe the de-excitation of the primary sources predicted by the SMF model. We also run GEMINI++ alone to simulate the decay of the big hot source corresponding to the whole system; this allows to compare the experimental fusion-like distributions with those predicted for a pure complete fusion process.

## 4.3 The TWINGO code

### 4.3.1 General considerations

The collaboration with the SMF model group, headed by Dr. Maria Colonna, brought to the adaptation of the TWINGO code to our data set. We ran TWINGO for both the investigated reactions ( $^{32}\text{S} + ^{40,48}\text{Ca}$  at 17.7 MeV/u), also adopting two different parametrizations for the symmetry energy term (asy-stiff and asy-soft EoS choice) for isospin related comparisons (see §1.2.3). For each system and each parametrization, we produced 10000 primary events over the whole impact parameter range (from 0 up to the grazing value with a triangular distribution, as shown in Figure 4.3). The output of TWINGO+GEMINI++ (primary and secondary observables in  $4\pi$ ) are presented here, while the filtered simulations (§4.5) are discussed together with the experimental data in Chapter 5.

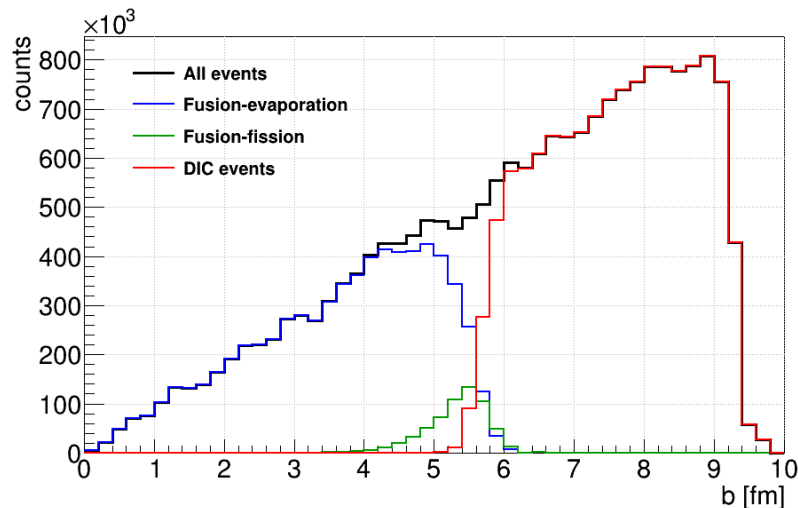


**Figure 4.3:** In black, the impact parameter distribution used as input for the TWINGO code is drawn for the reaction  $^{32}\text{S} + ^{48}\text{Ca}$  at 17.7 MeV/u. Coloured lines represent the different yields, predicted by TWINGO, for the available reaction channels, as a function of the impact parameter.

In the calculation 50 test particles per nucleon were used and a non-cubic geo-

metrical box was employed, measuring  $40 \text{ fm} \times 40 \text{ fm} \times 120 \text{ fm}$ , with the larger size along the beam axis and divided (for the calculation) in cubic cells with a volume of  $1 \text{ fm}^3$ . By choosing shorter dimensions for the sides perpendicular to the beam direction we optimized the calculation time without losing information. The calculation was stopped at  $500 \text{ fm/c}$ ; then the algorithm for the fragment recognition was applied at different times (200, 260, 300, 400 and  $500 \text{ fm/c}$ ) with a threshold density of  $0.03 \text{ fm}^{-3}$ ; test particles included in cells with density lower than the threshold are not attributed to any fragment. By definition, the test particles (of p-type or n-type) not included in any fragment constitute the light particle emission. As pointed out before, since the longer the recognition time, the larger the number of test particles emitted by fragments, it is clear that the recognition time has strong influence on the excitation energy of the recognized fragments at the end of the dynamical model calculation. Since those fragments with their properties (in primis, the excitation energy) are then fed to the afterburner (GEMINI++, in our case), the amount of secondary decay and the energy spectra of the evaporated particles (to be compared with the experimental ones) obtained at the end strongly depend on the recognition time.

Because of the lack of correlations in the SMF model, light particle emission is not well described. Nonetheless it is possible to keep track of the total mass and charge of the test particles which have been emitted, due to pre-equilibrium and evaporative effects, at the recognition time. However, at present it is not possible to recover the test particles that are not clusterized in nuclear fragments. This of course represents a significant difference with respect to the experimental case, where all particles and fragments, independently of the production mechanism and emission time, can be detected by the experimental setup (provided that, of course, they can overcome the detection threshold and that they are inside the detector geometrical acceptance). As a consequence, the best choice would be to recognize the fragments as soon as possible, with the caveat that if the time is too short, mainly for less central binary collisions, the distance among the clouds of test particles representing QP and QT is not enough and the algorithm finds only one big fragment, wrongly classifying as fusion a clearly binary event. An example was previously shown in Figure 4.2, where the test particle distribution at different times for an event with  $b = 5.83 \text{ fm}$  was plotted. In that case, if the fragment recognition is performed at  $300 \text{ fm/c}$ , the algorithm finds two heavy fragments with charge (mass) equal to 12 (26) and 17 (37), respectively, while at  $200 \text{ fm/c}$ , because of the neck of test particles between the two dense cores, only one heavy fragment is found, with charge (mass) 31 (68). The following de-excitation stage, treated by GEMINI++ code (see §4.4), does not

keep into account the fact that this big fragment is strongly deformed and this fact brings to an erroneous classification of the events (from DIC to fusion-like). For sake of accuracy we have to cite that, before applying the afterburner, the primary fragments are propagated along Coulomb trajectories up to 1200 fm/c; this allows to boost the fragments with the proper source velocity in order to compare with the experimental data.

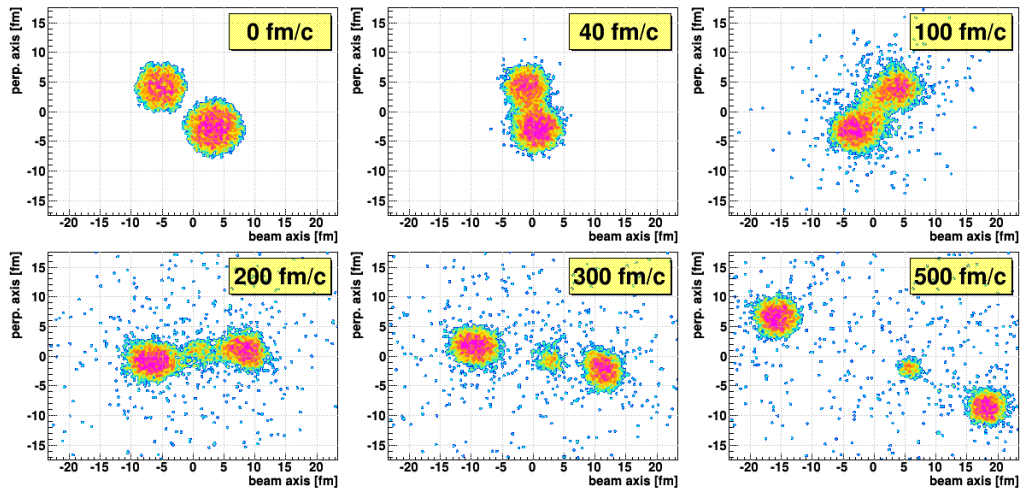


**Figure 4.4:** Example of an event simulated with the TWINGO code for the system  $^{32}\text{S} + ^{48}\text{Ca}$  at 17.7 MeV/u for a semiperipheral collision ( $b = 6.54$  fm). The reaction produces three main nuclei (neck emission). This is the only event of this kind in our set of simulated data (10000 events).

In this range of energy, the calculation predicts only two classes of events, as it is shown in Figure 4.3, where the yield of the different processes is plotted as a function of the impact parameter. Fusion events (with only one heavy fragment at the end of the recognition algorithm) are dominant for central collisions, but they extend up to impact parameter around 6 fm. DIC events (with two heavy fragments, QP and QT, at the end of the recognition algorithm) start from  $b \sim 5$  fm and they arrive up to the grazing impact parameter. To be precise, TWINGO predicted also a unique three fragment event. It corresponds to a very rare (at these energies) neck-type event in which also a  $Z = 2$ ,  $A = 5$  particle is identified in the middle of the two heavy fragments (see Figure 4.4). The fact that a so small number of neck-like events is found means that large density gradients cannot develop during the interaction. As a consequence we cannot expect to observe effect of isospin drift; on the contrary, isospin diffusion phenomena (i.e. the transport of isospin from the projectile to the target in the  $^{32}\text{S} + ^{48}\text{Ca}$  reaction) might be present.

In Figure 4.5 the impact parameter distribution for fusion events is shown on the left side; each curve corresponds to a different recognition time for the fragments.

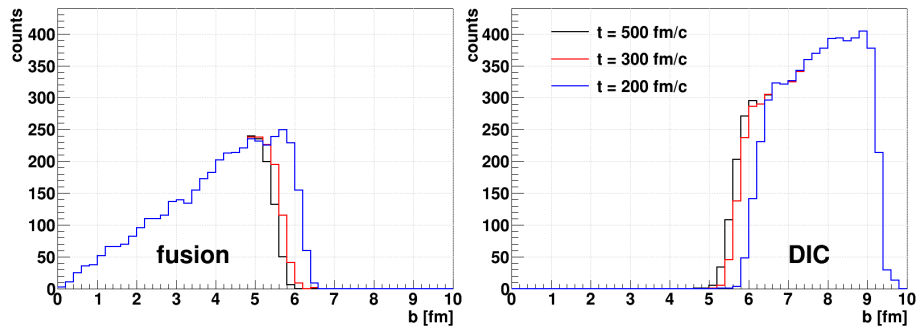


**Figure 4.5:** Left side: impact parameter distribution for events ending with only one heavy fragment (fusion events); right side: impact parameter distribution for events ending with two heavy fragments (DIC events). Different curves correspond to different fragment recognition times (black curve: 500 fm/c, red curve: 300 fm/c, blue curve: 200 fm/c)

The same for DIC events is plotted on the right side. As expected, reducing the recognition time, some DIC events in the region  $5 \text{ fm} < b < 7 \text{ fm}$  are shifted to the fusion class.

As we said before, increasing the recognition time the multiplicities of emitted particles increase both for the neutron number  $N$  and for charge number  $Z$ , as it is shown in Figure 4.6 as a function of the impact parameter for fusion-like and DIC events for both reactions. We repeat that, at present, the code is not able to regroup in light nuclei the test particles not included inside the identified fragments; as a consequence, it is not exactly correct to identify the  $N$ -particle emission as neutrons and the  $Z$ -particle emission as protons.

In Figure 4.7 top part the average  $Z$ -particle emission (left side) and  $N$ -particle emission (right side) as a function of the recognition time (integrated on the impact parameter) are summarized for both systems for the different reaction mechanisms. We can note that the particle emission increases with the recognition time, but also another aspect emerges from this figure (and from Figure 4.12 onwards): the system tends to emit more protons than neutrons both for DIC and for fusion events in the reaction  $^{32}\text{S} + ^{40}\text{Ca}$  (open symbols in Figure 4.7), at variance with the case of the reaction  $^{32}\text{S} + ^{48}\text{Ca}$  (full symbols in Figure 4.7). This is expected because in the  $N = Z$  system, whatever the degree of dissipation (i.e. reaction type), the total excitation energy must be spent to emit more protons (both free and bound) with respect to the  $^{48}\text{Ca}$  n-rich system. The more abundant proton (neutron) yield emitted by the  $^{40}\text{Ca}$  ( $^{48}\text{Ca}$ ) reaction has strong influence on the possible search for the isospin diffusion mechanism. In fact evidence of isospin diffusion should be found comparing the  $\langle N \rangle / Z$  of the QP in DIC reactions when changing the n-richness of the target. In presence of isospin diffusion, the  $\langle N \rangle / Z$  of the S-like QP should be higher in the reaction with  $^{48}\text{Ca}$ . Unfortunately, both the more abundant neutron

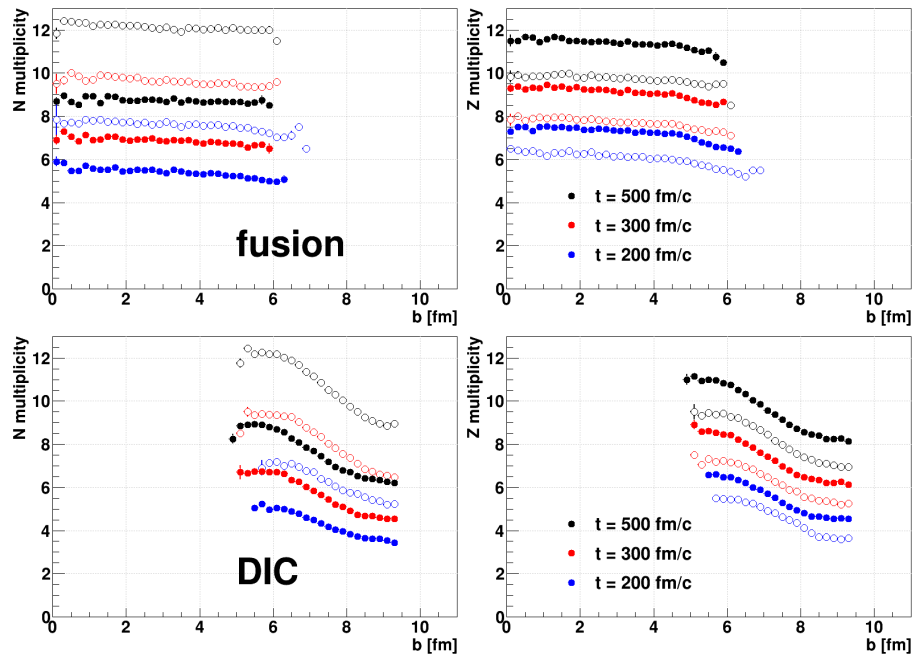


**Figure 4.6:** Average  $N$ -particle (left side) and  $Z$ -particle (right side) emission multiplicity as a function of the impact parameter. Top panels: fusion-like events; bottom panels: DIC events. Full circles:  $^{32}\text{S} + ^{40}\text{Ca}$ ; open circles:  $^{32}\text{S} + ^{48}\text{Ca}$ . As in Figure 4.5, different colors correspond to different fragment recognition times.

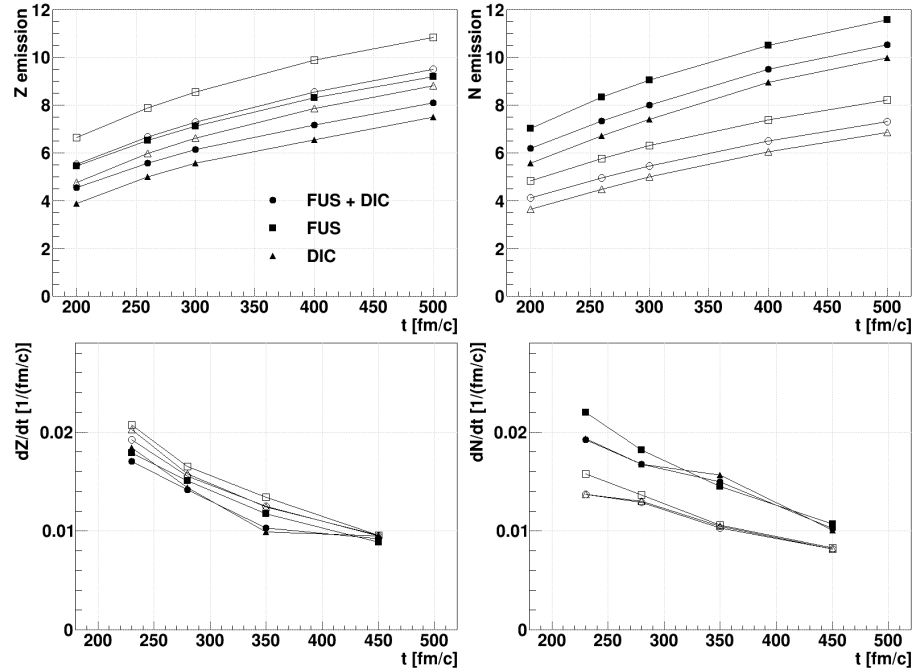


**Figure 4.7:** Top panels: average Top left: average  $N$ -particle (left side) and  $Z$ -particle (right side) emission multiplicity as a function of the recognition time. Bottom panels: rate of the  $Z$  (left side) and  $N$  (right side) emission as a function of the time. Full symbols:  $^{32}\text{S} + ^{40}\text{Ca}$ ; open symbols:  $^{32}\text{S} + ^{48}\text{Ca}$ . Circles correspond to the total emission, squares to fusion events and triangles to DIC events.

emission in the  $^{48}\text{Ca}$  case and, on the contrary, the excess of protons ejected in the  $^{40}\text{Ca}$  reactions play to reduce the isospin transport effect.

In the bottom part of Figure 4.7 the particle emission rate ( $Z$  on the left and  $N$  on the right), is presented as a function of the time (with the same symbols of the top part). The emission rate is roughly estimated from the differences of the emission found at different recognition times. These pictures show that at short times particles are fast emitted and then their emission rate decreases. We expect that, when we fully enter in the evaporative regime, the emission rate tends to flatten. Here we observe that at 400 fm/c, mainly for neutrons, the rate is only slightly decreasing; as a consequence we can assume the value 300 fm/c as a reasonable limit between the dynamical regime and the statistical decay. Thus, in the next Chapter we will adopt the fragment recognition at 300 fm/c as input of the GEMINI++ afterburner to produce the final distributions.

### 4.3.2 Fusion-like events

For fusion events, the average charge and mass of the compound nucleus as a function of the impact parameter is shown in Figure 4.8 for both reactions at various recognition times. An almost flat behaviour (with a slight increase for less central collisions) of mass and charge of the CN as a function of the impact parameter is observed.

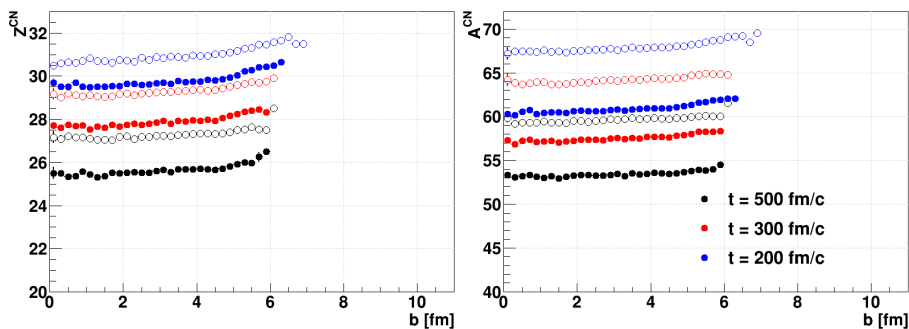


**Figure 4.8:** Average charge (left side) and mass (right side) of the compound nucleus as a function of the impact parameter for fusion events. Full circles:  $^{32}\text{S} + ^{40}\text{Ca}$ ; open circles:  $^{32}\text{S} + ^{48}\text{Ca}$ . As in Figure 4.5, different colors correspond to different fragment recognition times.

Concerning excitation energy, the obtained results for  $^{32}\text{S} + ^{40}\text{Ca}$  are presented in Figure 4.9 as a function of the impact parameter and for different recognition times. For the  $^{48}\text{Ca}$  case the results are similar. Since a considerable amount of pre-equilibrium emission is observed (see Figure 4.6), the excitation energy of the

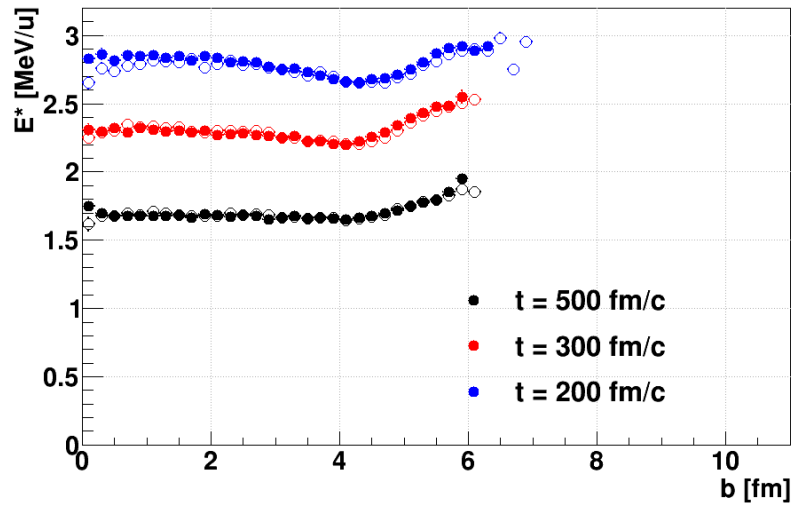


**Figure 4.9:** Average excitation energy per nucleon of the CN as a function of the impact parameter for fusion events. Full circles:  $^{32}\text{S} + ^{40}\text{Ca}$ ; open circles:  $^{32}\text{S} + ^{48}\text{Ca}$ . As in Figure 4.5, different colors correspond to different fragment recognition times.

formed CN is below the total available energy (more than 4 MeV/u, see Table 1.1 on page 5) and it obviously decreases when the recognition time is delayed.

As we will see in the next Chapter, when comparing experimental fusion evaporation events to simulated data (after applying an afterburner), the experimental LCP features (mainly multiplicity and energy spectra) will not be very well reproduced by the model. This discrepancy is partly due to the fact that the simulated CN fed to GEMINI++ is too little excited (Figure 4.9) because it already emitted many particles before the recognition time. Since these particles (not regrouped in clusters) cannot be included in the final energy spectra, it is quite expected that experimental spectra are harder than simulated ones.

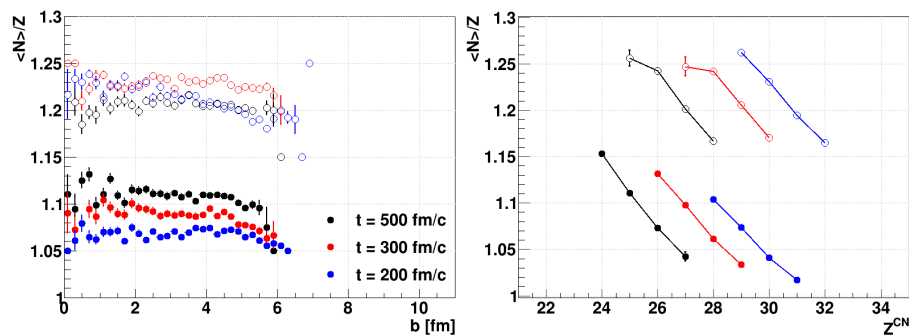


**Figure 4.10:**  $\langle N \rangle / Z$  of the CN as a function of the impact parameter (left side) and of its charge (right side) for fusion events. Full circles:  $^{32}\text{S} + ^{40}\text{Ca}$ ; open circles:  $^{32}\text{S} + ^{48}\text{Ca}$ . As in Figure 4.5, different colors correspond to different fragment recognition times.

Coming to the  $\langle N \rangle / Z$  of the fragments, which is a key observable for the study

of the isospin transport phenomena, in Figure 4.10 on the left the isospin of the CN as a function of the impact parameter for different recognition times is plotted. On the right the average isospin is plotted as a function of the charge of the fragment, integrated over all the impact parameters (we know from Figure 4.8 that the average charge of the CN slightly increases with the impact parameter). As expected, due to the different isospin content of the total system, the average isospin of the CN is higher for the n-rich system than for the n-poor one; the difference tends to decrease increasing the recognition time because, as we have seen, in the  $^{40}\text{Ca}$  case protons are preferentially emitted and the opposite is true for the  $^{48}\text{Ca}$ , thus reducing the  $\langle N \rangle / Z$  differences.

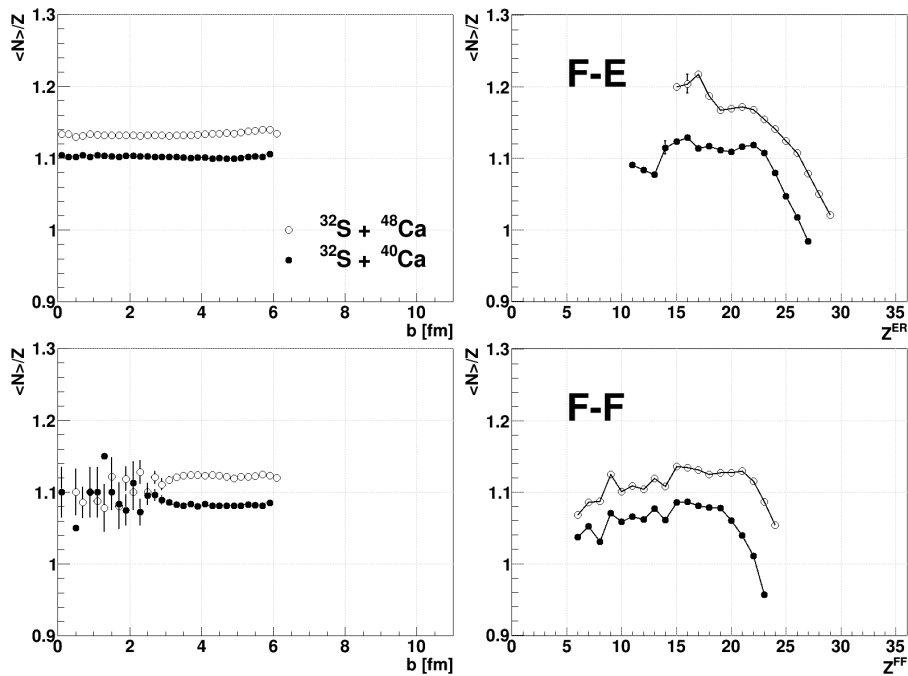


**Figure 4.11:** Average isospin as a function of the impact parameter (left side) and of the charge (right side) of evaporation residue/fission fragments in fusion-evaporation events (top panels) and in fusion-fission events (bottom panels). Bottom right: average isospin of the secondary fission fragments as a function of their charge in fusion-fission events. Full circles:  $^{32}\text{S} + ^{40}\text{Ca}$ ; open circles:  $^{32}\text{S} + ^{48}\text{Ca}$ . The recognition time is 300 fm/c.

In Figure 4.11 the average isospin obtained after applying GEMINI++ as afterburner is shown for the two reactions. Top part refers to fusion-evaporation events, ending with an heavy evaporation residue, while the bottom part concerns fusion-fission events, ending with two fission fragments in the exit channel. As before, on the left the average isospin is shown as a function of the impact parameter, while on the right we present the isospin as a function of the charge of the fragments. In fusion-evaporation events we observe a clear (and almost constant, as a function of

the impact parameter) difference between the  $^{40}\text{Ca}$  and the  $^{48}\text{Ca}$  case, obviously due to the different isospin content of the system and also to the different evaporation path (more emitted protons for the  $^{40}\text{Ca}$  case). For fusion-fission events, the model predicts a clear separation of the isospin values for the two reactions, both as a function of the impact parameter and as a function of the fragment charge. Thus, some isospin effects can be expected also in the experimental data, provided that the fission fragments are emitted in the solid angle covered by the Ring Counter detector and that their energy overcomes the threshold for isotopic separation. This is a quite restrictive condition which reduces the isospin analysis to only a small fraction of all the possible fission fragments.

### 4.3.3 DIC events

For more peripheral collisions, the amount of emitted light particles decreases too, but since it does not vanishes, also for grazing collisions the mass and charge of QP and QT are lower than those of projectile and target, as it is shown in Figure 4.12. This observation is confirmed also looking at the Wilczynski and Diffusion plots,

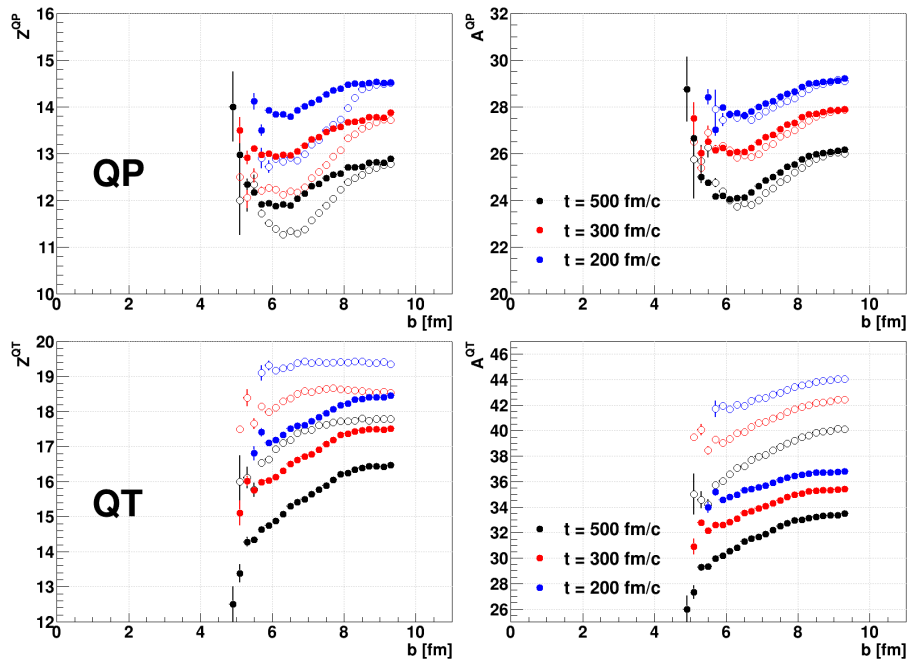


**Figure 4.12:** Average charge (left side) and mass (right side) of the QP (top panels) and the QT (bottom panels) as a function of the impact parameter. Full circles:  $^{32}\text{S} + ^{40}\text{Ca}$ ; open circles:  $^{32}\text{S} + ^{48}\text{Ca}$ . As in Figure 4.5, different colors correspond to different fragment recognition times.

shown in Figure 4.13 (left and right panels respectively), which are often used to characterize the binary dissipative collisions. The Wilczynski plot shows the Total

Kinetic Energy (TKE) of the primary fragments versus the angle in the centre-of-mass frame  $\vartheta_{\text{CM}}^{\text{QP}}$  at which the QP is emitted. The Diffusion plot shows the TKE versus the QP mass  $A^{\text{QP}}$ . The figure refers to the case of  $^{32}\text{S} + ^{48}\text{Ca}$  and

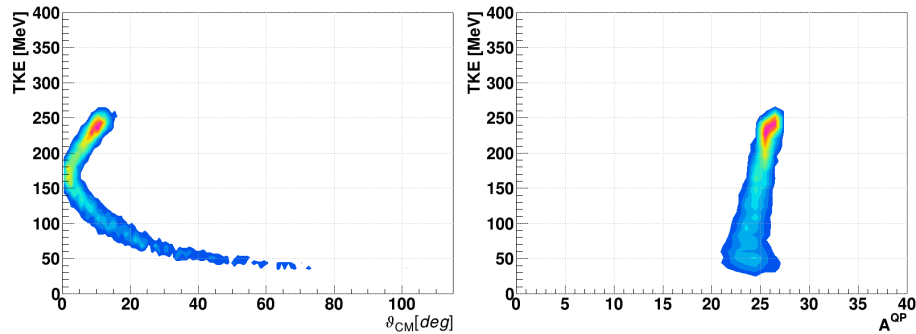


**Figure 4.13:** Wilczynski plot (left side) and Diffusion plot (right side) for the  $^{32}\text{S} + ^{48}\text{Ca}$  reactions. The recognition time is 300 fm/c.

the recognition time is 300 fm/c. According to this picture, the general behaviour expected for this kind of binary reactions is well reproduced by the model (for example, the polar angle of the QP in most peripheral reactions is very close to the grazing value); but even for the most peripheral collisions, the mass of the QP is considerably lower than that of the projectile ( $A = 32$ ). Moreover, from both the plots we note that the initial kinetic energy in the centre-of-mass frame is never reached (338 MeV for the  $^{32}\text{S} + ^{48}\text{Ca}$  reactions, see Table 1.1).

These facts suggest that the description of the model loses its reliability for the most peripheral collisions. Since this effect is due to the collisions among the test particles which are not inhibited also at very large impact parameters, one could improve a bit the situation increasing the number of test particles per nucleon. However, in order to obtain reasonable results, it would be necessary to increase their number at such a level that the numerical complexity of the calculation would become unaffordable. The comparison with our data is slightly affected by this limit because our experimental trigger and the geometrical acceptance of our setup strongly depress the most peripheral collisions.

In Figure 4.14 we can see that the QP and QT excitation energies decrease toward high impact parameters, as expected. However they don't drop to zero, neither for grazing collisions, because of the already cited spurious collisions among test particles. Delaying the recognition time, the excitation energy decreases because more particles are emitted in the meanwhile.

Concerning isospin related results, we show in Figure 4.15 some predicted effects (top part concerns the QP case, while bottom part refers to the QT) comparing the two reactions. Looking at the left side, where the isospin of the QP is plotted as a

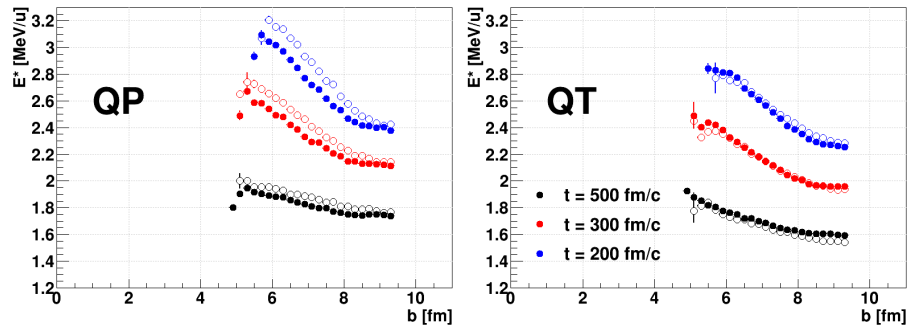


**Figure 4.14:** Average excitation energy per nucleon as a function of the impact parameter for QP (left side) and QT (right side) in DIC events. Full circles:  $^{32}\text{S} + ^{40}\text{Ca}$ ; open circles:  $^{32}\text{S} + ^{48}\text{Ca}$ . As in Figure 4.5, different colors correspond to different fragment recognition times.

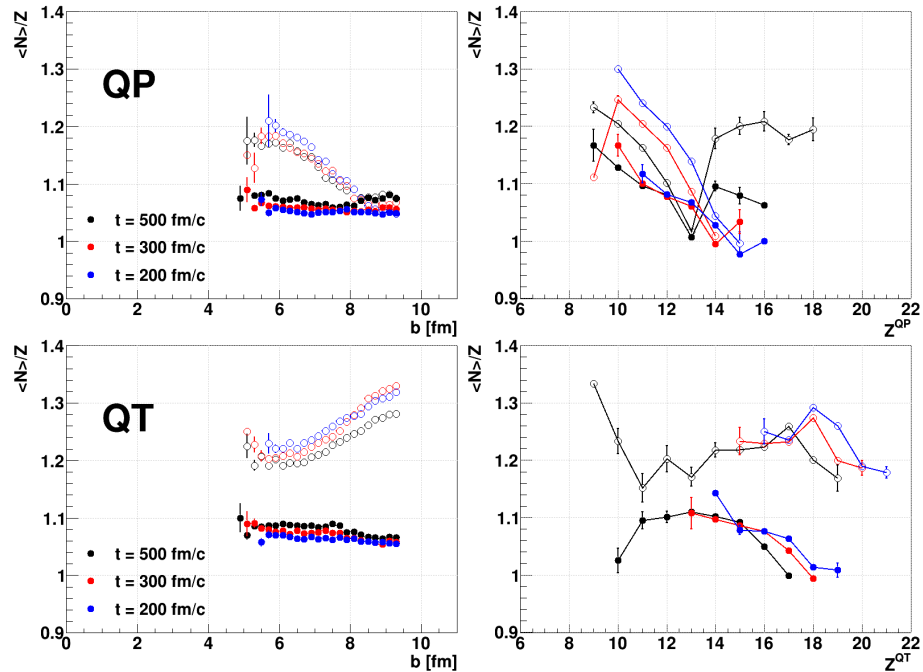


**Figure 4.15:** Average isospin as a function of the impact parameter (left side) and of the charge (right side) for the QP (top panels) and the QT (bottom panels) in DIC events. Full circles:  $^{32}\text{S} + ^{40}\text{Ca}$ ; open circles:  $^{32}\text{S} + ^{48}\text{Ca}$ . As in Figure 4.5, different colors correspond to different fragment recognition times.

function of the impact parameter, we can see that larger differences are observed for the less peripheral collisions. The QP in the reaction  $^{32}\text{S} + ^{40}\text{Ca}$ , where no isospin diffusion is expected ( $N/Z = 1$  for both projectile and target), almost constantly remains around  $N/Z \simeq 1.1$ ; this value differs from 1 because, as we said, in this reaction the system preferentially emits protons, thus increasing the isospin of the heavy fragment. For the  $^{32}\text{S} + ^{48}\text{Ca}$  reaction, a strong enrichment in the isospin of the QP, signature of the isospin diffusion process, is observed in less peripheral collisions, where the larger overlap between the two reaction partners allows to exchange more nucleons. In peripheral collisions, the isospin of the QP moves towards 1 (the original value), without reaching it, due to the model limitations at peripheral collisions that we discussed before. In this kind of representation no much difference is observed as a function of the recognition time.

On the right side of Figure 4.15, the average isospin is plotted as a function of the charge of the QP. In this case, since the impact parameters are mixed (because the impact parameter and the QP charge are not monotonically correlated, see Figure 4.12), the situation is more confused. For example, the open circles at  $Z \sim 14$ – $18$ , which suddenly jump at  $\langle N \rangle / Z = 1.2$ , may come from less peripheral impact parameters, where the separation between QP and QT is more problematic; as a consequence they might refer to the QT instead of the QP. Another problem of this representation is the fact that the number of events associated to a given  $Z$  is missing, thus misleading a little bit the interpretation of the plot. In any case, since this kind of plot is the only one we can do in the experimental case, yet it is important to investigate it. If we neglect the extreme values of  $Z$ , the isospin diffusion is clearly observed when the charge of the QP is in the region  $8 \leq Z \leq 13$  and the shorter the recognition time, the bigger the effect. For the QT (bottom part of Figure 4.15), we observe a complementary behaviour with respect to the QP, as a function of  $b$  in the  $^{48}\text{Ca}$  case: the isospin decreases moving towards more central collisions, as expected, since it is transferred to the QP. The QT of the n-poor case remains almost stable around 1.1, due to the proton evaporation of the system. Again, as a function of the charge of the QT, the situation is less clear (right side of the picture) because of the mixing of the impact parameter values.

In summary, the observed isospin in DIC collisions for the two reactions is the effect of a complicated interplay between the isospin diffusion process for the  $^{48}\text{Ca}$  case and the different kind of emissions in the two systems. From the point of view of the QP, the isospin diffusion when the target is the  $^{48}\text{Ca}$  causes the difference of isospin in the two reactions. However, the contribution of the particle emission reduces this difference because the n-poor system preferentially emits protons, while

the n-rich one preferentially emits neutrons.

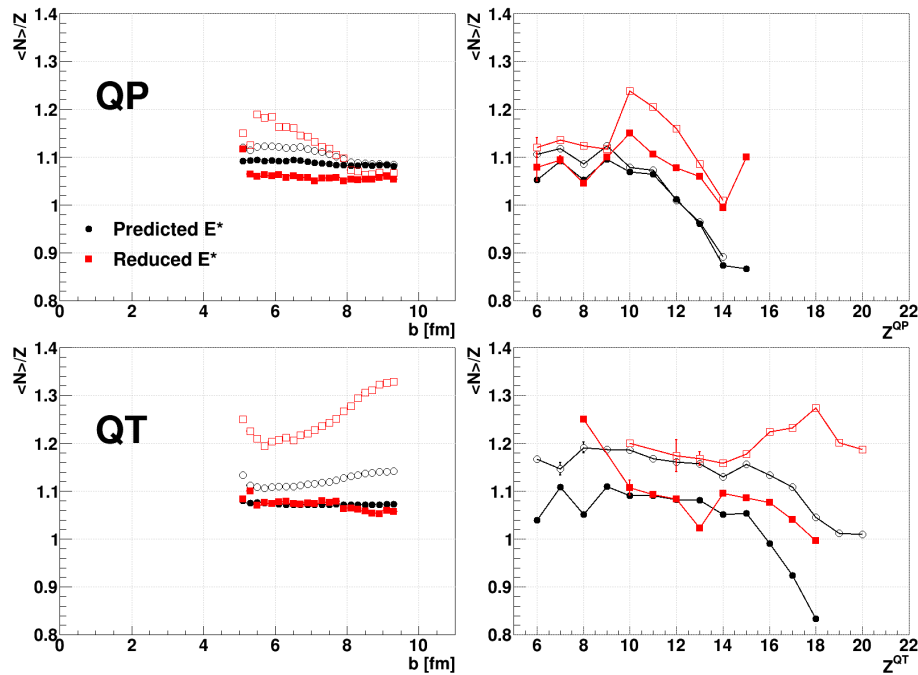


**Figure 4.16:** Average isospin as a function of the impact parameter (left side) and of the charge (right side) for the secondary QP (top panels) and the secondary QT (bottom panels) in DIC events. Full symbols:  $^{32}\text{S} + ^{40}\text{Ca}$ ; open symbols:  $^{32}\text{S} + ^{48}\text{Ca}$ . Black circles are obtained taking the excitation energy of fragments as given by the TWINGO code; red squares are obtained reducing it by 0.5 MeV/u. The recognition time is 300 fm/c.

The secondary decay tends to smear the isospin diffusion, as it is evident from black points in Figure 4.16, where the average isospin values of QP (top) and QT (bottom) as a function of the impact parameter (on the left) or of the charge (on the right) are shown for the two reactions after applying GEMINI++ as afterburner. In these pictures the recognition time is 300 fm/c, (to be compared with red curves in Figure 4.15). From these plots we can appreciate a residual isospin diffusion when we look at the QP case as a function of the impact parameter. On the contrary, the effect becomes almost negligible when the average isospin is plotted as a function of the charge of the QP, due to the mixing of the impact parameters. According to this model analysis, isospin diffusion effects result to be significantly reduced by secondary decay. If we reduce the recognition time to 200 fm/c, although for primary fragments the difference in the  $\langle N \rangle / Z$  of QP as a function of its charge in the two reactions becomes larger (blue symbols in Figure 4.15), no significant enhancement of the effect follows for secondary fragments. Only if we reduce the excitation energy of primary fragments by 0.5 MeV/u (a value compatible with the model uncertainties), we can keep a certain isospin diffusion effect on the secondary

fragments even for 300 fm/c recognition time (red symbols in Figure 4.16). As it will be discussed in Chapter 5, this is more in agreement with the experimental findings.

### 4.3.4 Asy-stiffness effects

As it was cited in Chapter 1, one of the main goal of the study of isospin phenomena is the comparison with model predictions including different parametrizations of the symmetry energy of the EoS in order to constrain its behaviour far from saturation density. Sizeable effects have been predicted and found at Fermi energies, where the system during the collision explores regions of different density (below the normal value). On the contrary, much smaller differences are expected at lower energies

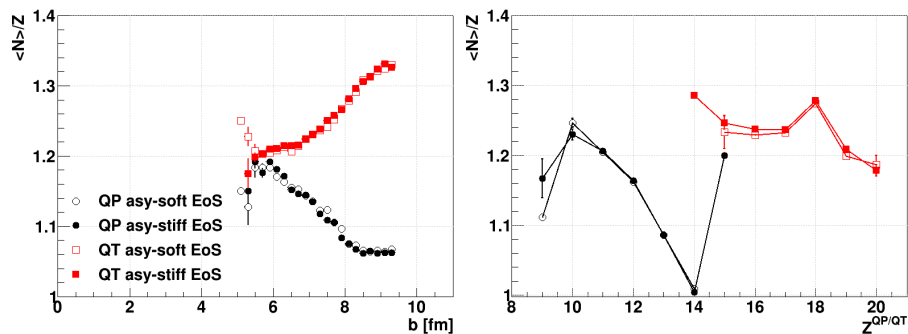


**Figure 4.17:** Average isospin as a function of the impact parameter (left panel) and of the charge (right panel) for the QP (black circles) and the QT (red squares) in DIC events. Open symbols correspond to an asy-soft parametrization for the symmetry energy, while full symbols corresponds to an asy-stiff parametrization. The recognition time is 300 fm/c.

(as in our case) where the explored density during the collisions remains around the normal value (where asy-soft and asy-stiff parametrizations coincide). This fact is demonstrated by Figure 4.17 for DIC events. The picture refers to the reaction  $^{32}\text{S} + ^{48}\text{Ca}$  for a fragment recognition time of 300 fm/c. Open symbols correspond to an asy-soft parametrization (this parametrization was used for all the figures plotted up to now), while full symbols correspond to an asy-stiff parametrization. We see almost no differences between the two  $E_{\text{sym}}$  assumptions and the results are quite similar for simulated fusion events. Therefore we expect that our experimental conditions are not sensitive to the stiffness of the symmetry energy.

## 4.4 The Gemini++ statistical model

There are many statistical model tools to simulate the decay of nuclear fragments (PACE, CASCADE, Empire-II, Simon, etc...). Today, one of the most used in

the nuclear physics community is GEMINI++ [47–50]. It accepts as input the nucleus charge  $Z$  and mass  $A$ , its excitation energy  $E^*$  and angular momentum  $J$ . GEMINI++ is a code which can be included as a part of a more complete Monte Carlo simulation to reproduce the measured events. In this case one randomly sorts a value of the impact parameter  $b$  (with a realistic distribution) and then runs the dynamical code to obtain the primary fragments; finally, for each fragment GEMINI++ is executed to obtain the secondary fragment distributions to be compared to the experimental one. As said before, when fusion reactions are studied at low energy and equilibrium is reached before any particle emission, one can directly use GEMINI++ giving as input parameters the total  $Z$  and  $A$  of the system, the calculated  $E^*$  and a random  $J$  generated following a triangular distribution up to the maximum spin at which the compound nucleus survives.

GEMINI++ is an improved version of the GEMINI statistical decay model, developed by R. J. Charity [51] with the goal of describing the decay of excited nuclei in a large range of energies, sizes, angular momenta as those produced in heavy-ion fusion experiments. The de-excitation of the compound nucleus proceeds through a sequence of binary decays until particle emission becomes energetically forbidden or is negligible due to the overwhelming competition with  $\gamma$ -ray emission. As compound nuclei created in heavy-ion reactions (specifically in fusion processes) are typically characterized by large intrinsic angular momenta, GEMINI++ explicitly considers the influence of spin on particle emission.

At variance with other statistical model routines, GEMINI++ treats both the light particle evaporation and the fission. This complete description, while it is quite useful for comparison with data, comes of course at the cost of several parameters that are needed to regulate the ingredients acting differently on the various exit channels. It was out of the scope of this thesis to enter the details of parameter regulation. Instead, we used GEMINI++ in its default option, the one designed to be a general purpose code. We attempted only to change the fission delay time  $\tau_f$  which is included in GEMINI++ to regulate the fission probability, mimicing the role of the viscosity in the fission process.  $\tau_f = 0$  gives the maximum fission probability, for a given parameter set, because it can compete at once with particle evaporation.  $\tau_f > 0$  (typically 5–20 zs) forbids the fission for a certain period, during which only light particles can be emitted. This delay represents the role of the viscosity which is a dynamical parameter and cannot be naturally present in statistical models, while it is properly taken into account in dynamical fission approaches [52, 53]. In any case, the introduction of a generic binary decay mode in GEMINI++ is necessary for the description of complex fragment formation and is one of the features that

set GEMINI and GEMINI++ apart from most of the other de-excitation models.

Within GEMINI++, the emission of nucleons and light nuclei ( $Z \leq 2, 3$  or  $4$ , depending on the user's choice) is described by the Hauser-Feshbach evaporation formalism [54], which explicitly treats and conserves angular momentum. For light systems and for asymmetric fission in heavier systems, the production of fragments is described by Moretto's binary-decay formalism [55]. Otherwise, the total fission yield is obtained from the Bohr-Wheeler formalism [56] and the width of the fission fragment mass distribution is taken from systematics compiled by Rusanov *et al.* [57]. In our case, the maximum size of the hot CN is  $A = 80$  and for these nuclei the Bohr-Wheeler formalism is not used.

The parameters of the model associated with evaporation have been adjusted to reproduce data from heavy-ion-induced fusion reactions [47]. To fit experimental light-particle kinetic-energy spectra, the transmission coefficients in the Hauser-Feshbach formalism were calculated for a distribution of Coulomb barriers associated with thermal fluctuations. The nature of fluctuations is not clear; they may be fluctuations of compound nucleus shape and/or of its density and/or of its surface diffuseness. Level densities are calculated with the Fermi-gas form:

$$\rho(E^*, J) \sim \exp\left(2\sqrt{a(U)U}\right)$$

where  $E^*$  is the total excitation energy,  $J$  is the spin, and  $U$  is the thermal excitation energy after the pairing, rotational, and deformation energies have been subtracted. The level density parameter  $a(U)$  in GEMINI++ is parametrized as an effective  $\tilde{a}(U)$  value that assumes the form:

$$\tilde{a}(U) = \frac{A}{k_\infty - (k_\infty - k_0) \exp\left(-\frac{\kappa}{k_\infty - k_0} \frac{U}{A}\right)}$$

which varies from  $A/k_0$  at low excitation energies to  $A/k_\infty$  at high values. GEMINI default parametrization is  $k_0 = 7.3$  MeV and  $k_\infty = 12$  MeV. The parameter  $\kappa$  defines the rate of change of  $\tilde{a}$  with energy and it is essentially zero for medium-light nuclei ( $A < 100$ ) and increases roughly exponentially with  $A$  for heavier nuclei. In our cases, since we have compound nuclei with  $A \leq 80$ , GEMINI++ will always use  $\tilde{a} = A/k_0$  as the level density parameter.

Generally speaking, adjusting GEMINI++ parameters (such as thermal fluctuation widths or  $k_0$ ) in the spin range and mass region of the studied systems would be very important to improve the predictions on fragment de-excitations. In fact, the parameters have an underlying physical meaning and by tuning them we can

understand the properties of the decaying nuclei. Just in this direction our collaboration recently made efforts to constrain GEMINI++ parameters using low energy reactions where complete fusion channel is supposed to prevail. In particular, I gave an effective contribution in the comparison, with GEMINI++, of the measured reactions  $^{48}\text{Ti} + ^{40}\text{Ca}$  at 300, 450 and 600 MeV [50, 58, 59], which has been useful also for *Giant Dipole Resonance* (GDR) studies at high spin values [49].

In the present case, as said, we didn't spend many efforts to improve or adjust the parameters of GEMINI++ and we preferred to run it essentially with the default options, mainly for two reasons. The first is that in our reactions — in case of complete fusion — the excitation energies for Krypton CN are above 4 MeV/u, larger than the typical values at which Gemini is used (below 3 MeV/u). So the code is operating in an extrapolation regime for some degrees of freedom where a fine tuning would be unuseful. The second, on the contrary, is that in our systems the contribution of some pre-equilibrium emission is likely; therefore, if this happens, the formed CN (whatever the centrality of the reaction) are less excited and they should enter in a region where the GEMINI++ applicability is safer. On the other hand, in this scenario the sources are less defined (there is a set of compound nuclei with unknown distributions of  $A$ ,  $Z$ ,  $J$  and  $E^*$ ) and the fine parameter tuning is unaffordable or scarcely constraining. Thus we decided to use the GEMINI++ code as a general guidance for the results, in particular to estimate the efficiencies of our set-up and to evidence, in a prudential way, effects clearly incompatible with statistical description.

## 4.5 Geometrical filter

The simulated secondary events have to be compared with experimental results. The response function of a composite apparatus is in general a huge problem which cannot be fixed in an analytical way but only using Monte Carlo simulations. In this way we can attempt to insert, in the simulated data analysis, all the known geometry and efficiency effects for each detector, in order to filter the calculated quantities just as the true quantities are during the experiment: the final spectra are directly comparable with experimental ones. For example, in Figure 4.18 the effect of the filter on the evaporation residue distribution from a GEMINI++ simulation is shown.

Though our apparatus has a large acceptance (more than 60% of  $4\pi$  sr, see Chapter 2), a sizeable fraction of reaction products cannot be detected. One of the most important role of the simulations is the extraction of the efficiencies for each reaction channel. For example, referring again to Figure 4.18, the ER detection

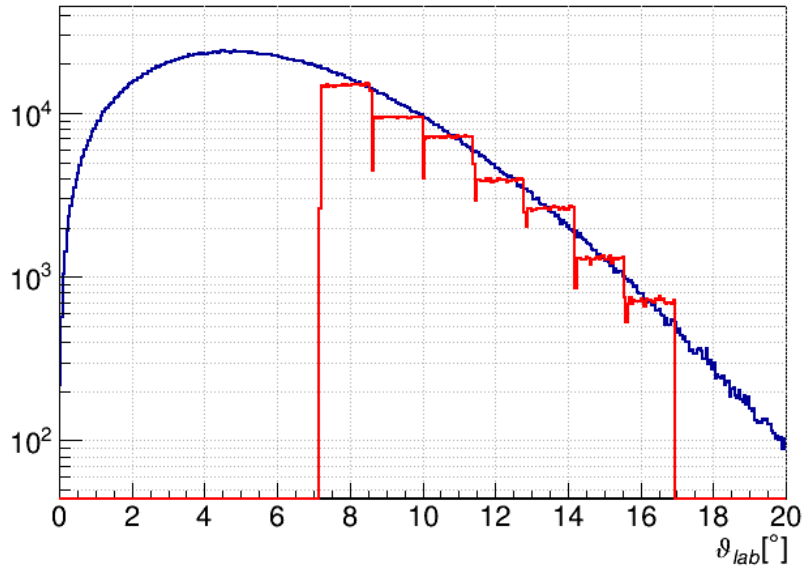


**Figure 4.18:** Evaporation residue detection efficiency. Blue line: the  $4\pi$  ER angular distribution; Red line: the same distribution after the filtering with the software replica of the detector acceptance.

efficiency is about 29%. Applying these efficiency factors to experimental data permits to verify experimental effects on detected distributions and to reconstruct  $4\pi$  quantities from the measured ones.

## 5.1 General event features

Each calibrated event contains the identified particles and fragments in terms of charge ( $Z$ ) and nuclear mass ( $A$ ) when possible. For each identified particle we have also the initial kinetic energy and the direction. We must note that our detectors don't measure directly the velocities but the energies. Thus, to reconstruct the velocity (or momentum), the mass information is needed. While for  $Z = 1$  and  $Z = 2$  the isotope discrimination is always feasible, we have mass discrimination for  $Z > 2$  ions only when they punch through the Si layer of the Ring Counter (for energy ranges see Table 3.2 on page 45). For all other ions an hypothesis on  $A = A(Z)$  must be assumed. In particular we assign  $A = 2Z$  in the range  $2 < Z < 12$  and  $A = 2.072 Z + 2.32 \cdot 10^{-3} Z^2$  (evaporator attractor line formula [60]) for  $Z \geq 12$ .

We start to characterize the various collected events, for the two target cases ( $^{40}\text{Ca}$  and  $^{48}\text{Ca}$ ), in order to distinguish the main reaction mechanisms which contribute to the reaction cross section. We expect that the most important reaction channels for our reactions are associated to fusion-like processes and Deep Inelastic Collisions (DIC).

### 5.1.1 Cleaning conditions

For the further analysis, it is important to reduce spurious events as much as possible. As we said before (§2.3.2 on page 34), in this experimental campaign the main

trigger condition GARFIELD+RCo (at least one particle in GARFIELD and one in RCo) was used. This condition is by itself rather constraining to good events. In fact requiring the coincidence between at least two particles strongly reduces the spurious particles, that are usually not correlated with any other particles. The trigger selection restricts the considered events to the 46% of the total number written on disk.

However, there are still some events in which the total collected charge  $Z_{\text{tot}}$  (the total charge summed over all the detected particles) is larger than  $Z_{\text{sys}} = Z_p + Z_t$  and/or the total momentum  $P_{\text{tot}}$  is larger than the initial projectile momentum  $P_i$ . So we removed the events with  $P_{\text{tot}}^{\prime\prime} > 1.05 P_i$  or with  $Z_{\text{tot}} > Z_{\text{sys}}$ .  $P_{\text{tot}}^{\prime\prime}$  is the projection of  $P_{\text{tot}}$  along the beam axis. We allowed for a 5% excess of  $P_{\text{tot}}^{\prime\prime}$  to take into account both ion mass uncertainties and effects of energy resolution. We also restricted our selection by rejecting highly uncomplete events through the conditions  $P_{\text{tot}}^{\prime\prime} > 0.2P_i$  and  $Z_{\text{tot}} \geq 10$ . Applying these cuts we are rejecting around 4% of the registered events. Overall, after these cuts, 42% of the initial set of events is kept.

### 5.1.2 Event selection

Referring to the detailed classification reported in Chapter 1, we may sort all our events in three main classes:

**Fusion-evaporation (F-E)** a single large fragment — the evaporation residue (ER) — is detected in coincidence with evaporated particles. The ER has a low velocity in the centre-of-mass (CM) frame due to the recoil of emitted particles.

**Fusion-fission (F-F)** the CN splits into two fragments which are therefore correlated: they are emitted back-to-back in the CM frame and their relative velocity distribution is centered at values in agreement with the Viola systematics of fission [61].

**Deep Inelastic Collisions (DIC)** the reactions are characterized by the presence of two fragments corresponding to the quasi-projectile (QP) and to the quasi-target (QT). QP is focused at forward angles in the CM frame while QT is backward emitted. In practice, due to the generally low QT velocities, the detection of QP and QT in coincidence is rare, so we divided the DIC selection into two sub-classes: **QP+QT**, in which we identified both the QP and the QT, and **QP-only**, where only the QP fragment was detected.

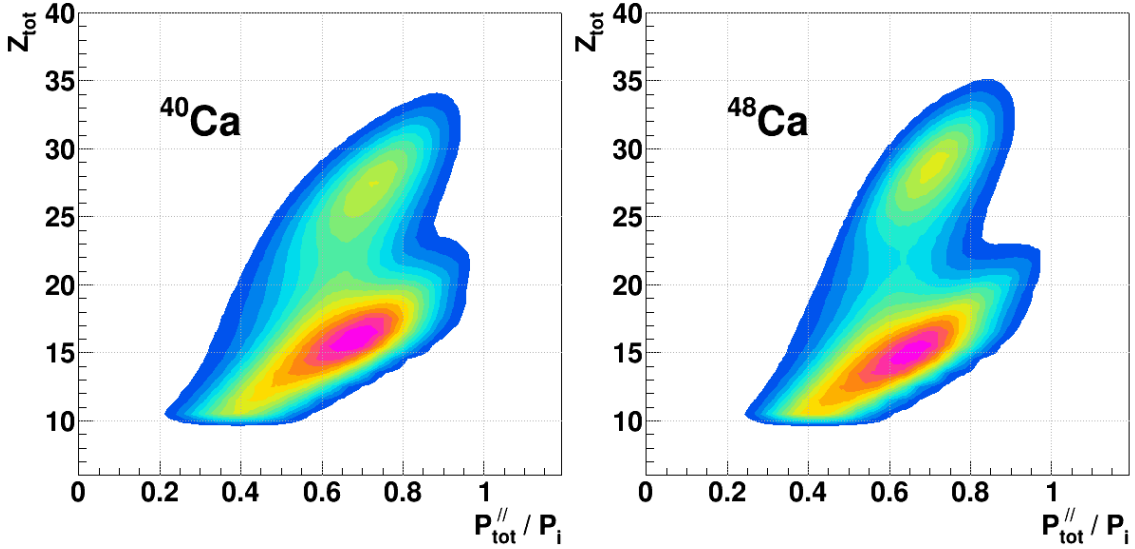
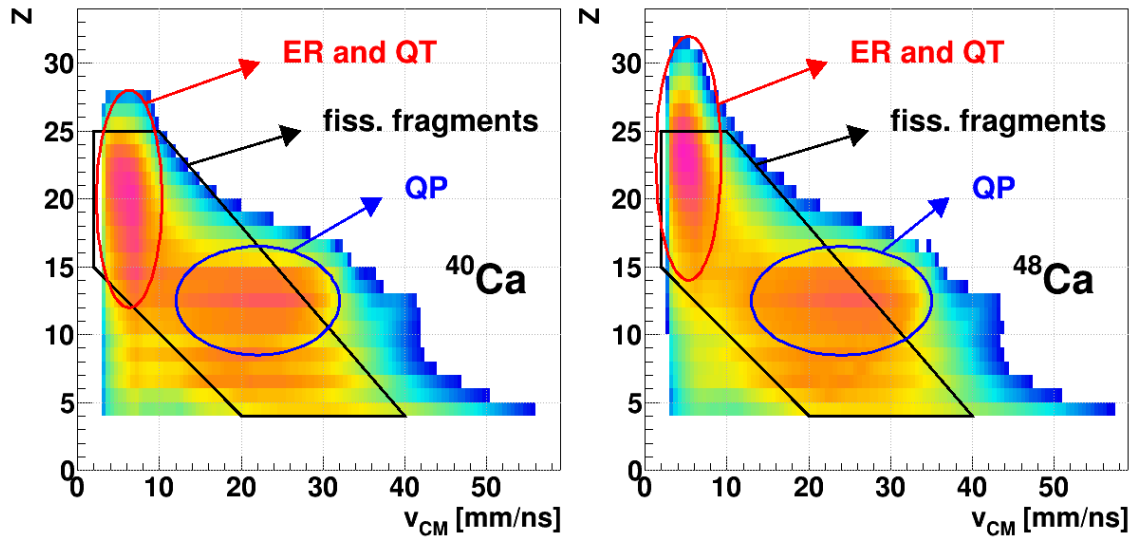


**Figure 5.1:** Total collected charge  $Z_{\text{tot}}$  versus the ratio between the total momentum projection along the beam axis and the initial momentum  $P_{\text{tot}}^// / P_i$  after the described cuts. Left panel:  $^{32}\text{S} + ^{40}\text{Ca}$  reactions; right panel:  $^{32}\text{S} + ^{48}\text{Ca}$  reactions.

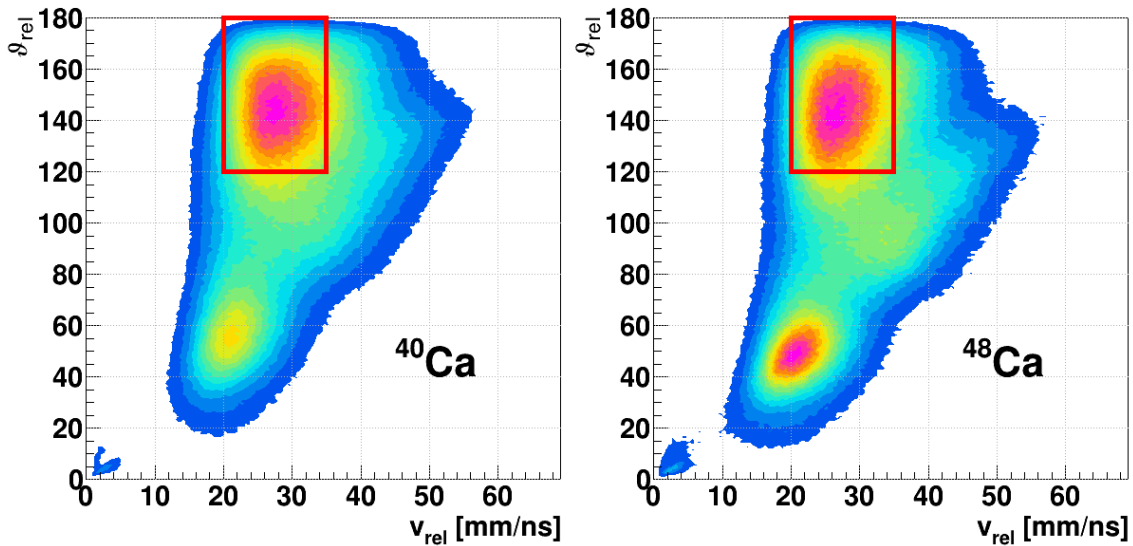
The different reaction mechanisms can be recognized with the help of the Figures 5.1 and 5.2. The first one presents a  $Z_{\text{tot}}$  versus  $P_{\text{tot}}^// / P_i$  plot. The second one shows the correlations between the charge  $Z$  of measured species versus their CM velocity. In each figure, on the left the  $^{40}\text{Ca}$  reaction is presented, while on the right the  $^{48}\text{Ca}$  one. These plots are commonly used in our field to present the general characteristics of the measured events.

Figure 5.1 shows two main regions. One is associated to events in which great part of the total charge is collected ( $Z_{\text{tot}} > 22$ ). The second group of events is populated mainly by DIC events in which we lost the quasi-target fragment and thus the total collected charge is much lower than  $Z_p + Z_t$ . A contribution of fusion-fission events where only one fission fragment was detected cannot be excluded, too.

Also in Figure 5.2 two main regions are visible. One is associated to fragments much heavier than Sulphur, with  $14 \leq Z \leq 28$  and  $16 \leq Z \leq 32$  for  $^{40}\text{Ca}$  and  $^{48}\text{Ca}$  target, respectively. The island of these heavy fragments is characterized by very low velocities which are compatible with a compound nucleus or a quasi-target from a deep inelastic collision. The second group of events is less sharply defined and has a charge range  $10 \lesssim Z \lesssim 15$  with high centre-of-mass velocities. This is populated mainly by QP from DIC events. We can also recognize a contribution of fusion-fission events overlapping the fusion-like and DIC regions. In fact, a very asymmetric fission resembles a fusion-evaporation process while a symmetric fission is quite similar to a strongly dissipative collision.



**Figure 5.2:** Charge versus the velocity in the centre-of-mass is drawn for every particle. Graphical cuts indicates the kind of species that populates each region. Left panel:  $^{32}\text{S} + ^{40}\text{Ca}$  reactions; right panel:  $^{32}\text{S} + ^{48}\text{Ca}$  reactions.



**Figure 5.3:** Correlation between the relative angle in the CM frame and the relative velocity of two fragments with  $Z \geq 4$ . The red rectangular window identifies the fusion-fission selection gates. Left panel:  $^{32}\text{S} + ^{40}\text{Ca}$  reactions; right panel:  $^{32}\text{S} + ^{48}\text{Ca}$  reactions.

The event selection for the different reaction mechanisms is a three-step procedure. The events included in a step are excluded from further selections (the three classes are exclusive):

1. First of all, F-E events are selected looking for an ER in coincidence with only light charged particles (LCP). This is implemented by requiring only one fragment within specific graphical cuts (decided for each reaction as shown indicatively in Figure 5.2). Beside the ER, the event can contain only LCP ( $Z = 1, 2$ ) and Lithium ions.
2. The DIC events are chosen by imposing the presence of at least a fragment (QP) with  $\vartheta_{\text{CM}} < 60^\circ$  and  $8 \leq Z \leq 16$ . Possibly a second fragment (QT) with  $12 \leq Z \leq 20$ , emitted at  $\vartheta_{\text{CM}} > 120^\circ$ , could be present too.
3. For the F-F case, we limited the selection to the events in which two fragments with  $Z \geq 4$  were detected, possibly accompanied by LCP. The fission fragment candidates have been selected on the basis of the correlation  $\vartheta_{\text{rel}}$  versus  $v_{\text{rel}}$  as shown in Figure 5.3. We imposed the conservation of momentum in binary splits taking into account that a perfect alignment is spread out by evaporation and resolution effects (indeed we chose  $\vartheta_{\text{rel}} > 120^\circ$ ); moreover we chose a  $v_{\text{rel}}$  window according to the Viola systematics (20–35 mm/ns) [61].

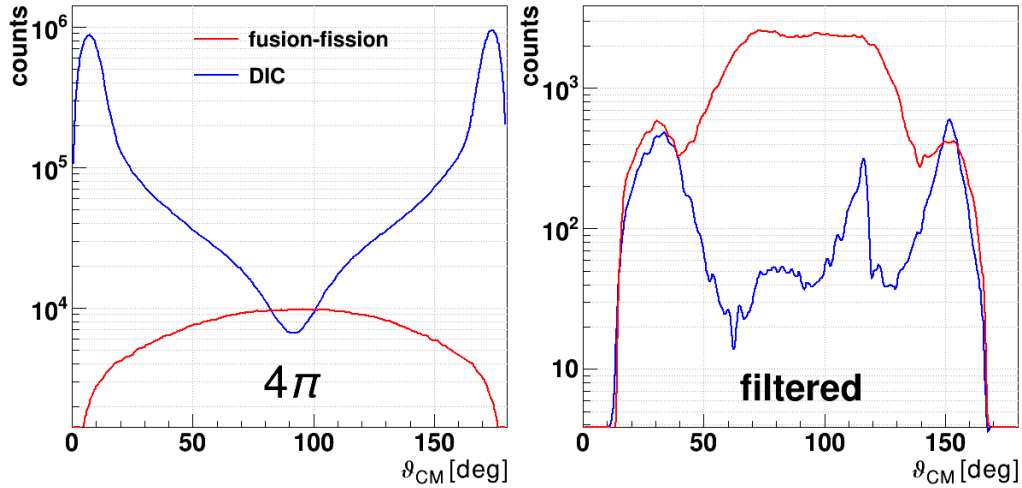


**Figure 5.4:** Angular distributions in the CM frame of fission fragments (red) and QP-QT pairs (blue) following the TWINGO+GEMINI++ predictions. In the left panel the original simulated distributions are shown, while the geometrically filtered ones are reported in the right panel

We underline that, in the present systems, the two event classes F-F (3) and DIC (2) cannot be fully disentangled on the basis of the kinematics. Indeed, both

classes contains two major fragments plus LCP, with relative velocities close to the fission systematics (the DIC events in our analysis must be strongly dissipative to allow for the QP+QT pair having been detected). Finally, both classes have wide  $\vartheta_{\text{CM}}$  distributions, according to the expected relatively long contact times before separation. However for DIC, we expect a certain residual focusing around QP (QT) directions: this is the reason of the choice  $\vartheta_{\text{CM}} < 60^\circ$  for QP and  $\vartheta_{\text{CM}} > 120^\circ$  for QT in the class DIC. The choice of class DIC is done before class F-F so we could have some pollution of fusion-fission events within the DIC class.

event subset	Meas. sharing		Contam. (calc.)	
	$^{40}\text{Ca}$	$^{48}\text{Ca}$	$^{40}\text{Ca}$	$^{48}\text{Ca}$
Fusion-evaporation	20 %	23 %	2.0 %	0.4 %
Fusion-fission	2.5 %	2.6 %		
DIC (QP+QT)	1.0 %	0.8 %	41 %	46 %
DIC (QP-only)	49 %	52 %	1.5 %	1.4 %

**Table 5.1:** Experimental event sharing among the exclusive subsets expressed as the fraction of all the events with not more than two  $Z \geq 4$  fragments. The event subset contamination due to other event classes is estimated thanks to a TWINGO+GEMINI++ simulation. This kind of simulation cannot distinguish between F-E and F-F because they both originate from a single big primary fragment.

The previous considerations are well illustrated in Figure 5.4 where the angular distributions of fission fragments (red) and QP-QT pairs (blue) are drawn following the TWINGO+GEMINI++ predictions. In the left panel the original simulated distributions are shown, while the geometrically filtered ones are reported in the right panel. The selected conditions further clean the DIC events with respect to the figure right panel, but the contamination from fission remains high, as it is shown in Table 5.1, where the measured fractions of the different kind of exclusive event subsets are presented together with the contamination from different event classes estimated thanks to the TWINGO+GEMINI++ simulation. The measured event sharing is normalized to the number of events with no more than two  $Z \geq 4$  fragments. The total is below 100 % because some events are not selected by our choice of gates.

It's worth mentioning in Figure 5.3 the occurrence of a strange intensification at  $\vartheta_{\text{rel}} \sim 50^\circ$  and  $v_{\text{rel}} \sim 20$  mm/ns. This region contains events where fragments have relative velocities compatible with the Viola systematics (i.e. fully relaxed motion governed mainly by the Coulomb repulsion) but have relative angles strongly violating the binary kinematics. As we will see in the next paragraph, these events

are attributable to  $^{32}\text{S} + ^{12}\text{C}$  reactions. The wrong direction in the centre-of-mass frame is due to the wrong assumption of the system because we are calculating CM velocities for the  $^{32}\text{S} + ^{12}\text{C}$  events as they were from  $^{32}\text{S} + ^{40,48}\text{Ca}$  reactions, instead.

### 5.1.3 Carbon background

As said at the beginning of Chapter 2, the Calcium targets were protected against oxidation by means of thin carbon foils deposited on both surfaces. The ratio of the reduced thicknesses between C and Ca is 0.04. As a consequence one expects that a few percent level background of  $^{32}\text{S} + ^{12}\text{C}$  reaction products can pollute the event selections of the main  $^{32}\text{S} + ^{40,48}\text{Ca}$  reaction channels. To estimate the  $^{32}\text{S} + ^{12}\text{C}$  contribution in the various  $^{32}\text{S} + ^{40,48}\text{Ca}$  distributions, a specific run has been carried out during the data taking, employing a  $15\ \mu\text{g}/\text{cm}^2$  thick  $^{12}\text{C}$  target. This  $^{32}\text{S} + ^{12}\text{C}$  run just followed the  $^{32}\text{S} + ^{48}\text{Ca}$  and lasted about 8 h with the same trigger configuration of the main reactions. The analysis of these events helps to estimate and possibly subtract the spurious contributions from our main observables on  $^{32}\text{S} + ^{40,48}\text{Ca}$ .

Before entering the details of this background analysis we anticipate some general arguments. Considering that the grazing angle for the  $^{32}\text{S} + ^{12}\text{C}$  reaction is quite small (less than  $2^\circ$ ), the contribution of moderately inelastic binary collisions from  $^{32}\text{S} + ^{12}\text{C}$  spoiling our data should be small. Also, central collisions of  $^{32}\text{S} + ^{12}\text{C}$  resulting in complete or incomplete fusion (and evaporation) should produce lighter residues than  $^{32}\text{S} + ^{40,48}\text{Ca}$ : even assuming complete fusion (scarcely probable at this energy), the CN produced in  $^{32}\text{S} + ^{12}\text{C}$  ( $^{44}\text{Ti}$ ) would be excited and would undergo the decay, thus the ER from  $^{32}\text{S} + ^{12}\text{C}$  is expected quite lighter than the evaporation residue of the main reaction ( $Z_{\text{ER}} \sim 22$ ). Also the forward focusing of the ER from  $^{32}\text{S} + ^{12}\text{C}$  is stronger than for  $^{32}\text{S} + ^{40,48}\text{Ca}$  and this reduces the amount of detected fragments above the active geometrical limit of the RCo ( $7^\circ$ ).

Considering the large acceptance of our apparatus, when summing the charge  $Z$  of all the detected particles for many events we obtain a value of  $Z_{\text{tot}}$  that is close to the total system charge  $Z_{\text{sys}}$ . In particular, this is true when all the heavier fragments of the reaction (ER, FF or QP+QT) are collected, as it can be seen in Figure 5.1 where two event clusters are visible: the top one corresponds to an almost complete characterization (all main fragments collected), while the bottom one refers to events where a big fragment is lost (typically the slow QT). Since  $Z_{\text{sys}} = 22$  for  $^{32}\text{S} + ^{12}\text{C}$ , this reaction can only produce a background in the incompletely detected events of the  $^{32}\text{S} + ^{40,48}\text{Ca}$  reactions. As a consequence, we expect that the Carbon background affects mostly the selected QP-only events. For the other event classes,

the condition  $Z_{\text{tot}} > 22$  is sufficient to automatically exclude Carbon background without affecting  $^{32}\text{S} + ^{40,48}\text{Ca}$  data.

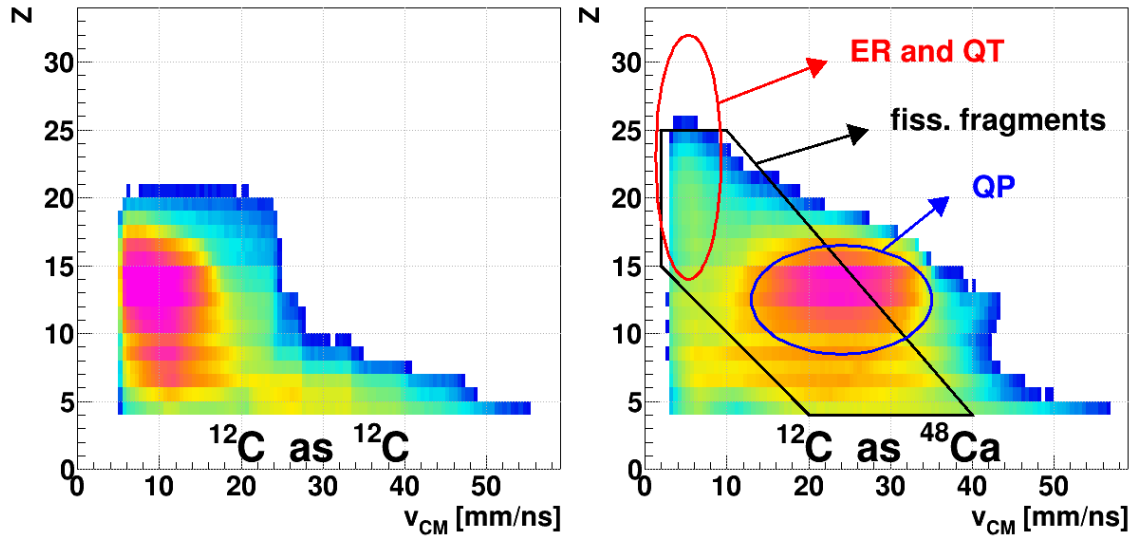


**Figure 5.5:**  $Z$  versus  $v_{\text{CM}}$  correlation in  $^{32}\text{S} + ^{12}\text{C}$  reactions. In the left panel the system is correctly analyzed, while in the right panel the system is treated like  $^{32}\text{S} + ^{48}\text{Ca}$ . The cuts correspond to the regions where the different event classes for the  $^{32}\text{S} + ^{48}\text{Ca}$  reactions are located.

The spurious reactions on  $^{12}\text{C}$  cannot be identified event by event in our analysis. However, the measured events of Sulphur on Carbon target, analyzed as they were on Calcium targets, allow to evidence the shape of the distributions when the  $^{12}\text{C}$  is a contaminant of the main reactions. This is favoured by the very different masses of Carbon and Calcium: the two CM velocities are strongly different and the kinematics is heavily affected. This is illustrated in Figure 5.5, where we show the  $Z$  versus  $v_{\text{CM}}$  plot for the  $^{32}\text{S} + ^{12}\text{C}$  reactions treated like  $^{32}\text{S} + ^{12}\text{C}$  (left panel) or like  $^{32}\text{S} + ^{48}\text{Ca}$  (right panel). In the left panel, the cleaning conditions for  $^{32}\text{S} + ^{12}\text{C}$  remove the spurious events with  $Z \gtrsim 20$ . In the right plot instead the conditions are based on  $^{32}\text{S} + ^{48}\text{Ca}$  reactions, so the cuts are not as effective as they should be. Focusing on the most populated region of the figure, it appears, from the left panel, to be originated by slow and heavy fragments, most probably evaporation residues. In the right panel these events are however shifted toward higher velocities due to the wrong centre-of-mass assumption. In particular they overlap with the region populated by quasi-projectiles from  $^{32}\text{S} + ^{48}\text{Ca}$ , corroborating our previous hypothesis that Carbon background contribution affects mainly the QP-only selection.

For what concerns fusion-fission, instead, it's easy to see from Figure 5.6 that most of Carbon background is eliminated. In fact, the  $^{32}\text{S} + ^{12}\text{C}$  fission fragments (with Viola-like relative velocity and back-to-back emission in the right centre of

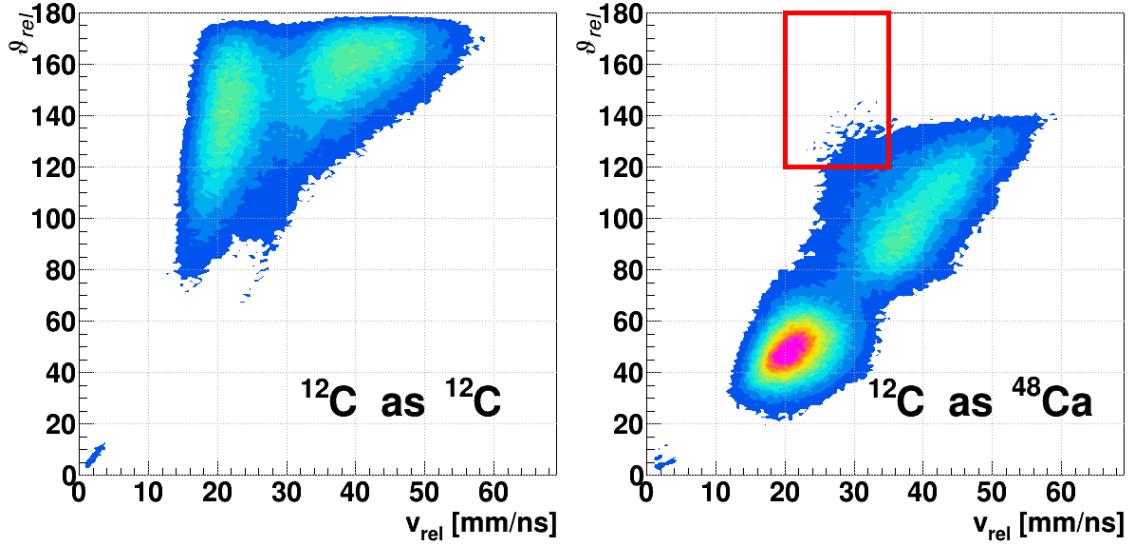


**Figure 5.6:**  $\vartheta_{rel}$  versus  $v_{rel}$  correlation in  $^{32}\text{S} + ^{12}\text{C}$  reactions. In the left panel the system is correctly analyzed, while in the right panel the system is treated like  $^{32}\text{S} + ^{48}\text{Ca}$ . The lines define the cuts adopted for the fission selection (see Figure 5.3). The shift of  $\vartheta_{rel}$  naturally excludes background events from the main analysis.

mass frame) move to around  $\vartheta_{rel} \sim 50^\circ$  when constrained by the wrong kinematics.

It’s just using this evident Carbon background region that we can infer a normalization to subtract the spurious events from our data. Indeed, we assume that the  $\vartheta_{rel} \sim 50^\circ$  bump region — clearly visible also in Figure 5.3 concerning  $^{32}\text{S} + ^{40,48}\text{Ca}$  reactions — is entirely due to  $^{32}\text{S} + ^{12}\text{C}$  background. Then we analyze the  $^{32}\text{S} + ^{12}\text{C}$  data as  $^{32}\text{S} + ^{40,48}\text{Ca}$ , with exactly the same routine that produces all the spectra. The normalization factor is the ratio  $f_A = N_A/N_{\text{bkg}}$  where the two integrals  $N_A$ ,  $N_{\text{bkg}}$  are limited to the above discussed “full background” region. In particular,  $N_A$  refers to the contaminated  $^{32}\text{S} + ^A\text{Ca}$  reactions, while  $N_{\text{bkg}}$  refers to the reference  $^{32}\text{S} + ^{12}\text{C}$  data. Because the number of events is different between  $^{32}\text{S} + ^{40}\text{Ca}$  and  $^{32}\text{S} + ^{48}\text{Ca}$  reactions, we expect to find different  $f_A$  values. Then, when needed, for each spectrum  $S$  of  $^{32}\text{S} + ^{40,48}\text{Ca}$  we obtain the “clean” spectrum  $S_{\text{clean}}$  by subtracting the background bin by bin:

$$S_{\text{clean}}(i, j) = S(i, j) - f_A \cdot S_{\text{bkg}}(i, j)$$

The  $f$  factors for the  $^{32}\text{S} + ^{40,48}\text{Ca}$  reactions resulted to be  $f_{48} = 2.8$  and  $f_{40} = 5.1$ .

Unexpectedly we found also a small Carbon background in the  $^{32}\text{S} + ^{48}\text{Ti}$  reactions, while the  $^{48}\text{Ti}$  had not the  $^{12}\text{C}$  protecting foils. This contamination may be due to the prolonged (days) exposition of the metallic target to Carbon atoms coming from various polluting sources in the scattering chamber (oil from pumps, residual

grease, low vacuum quality of some pipes for cooling) also taking into account the moderate vacuum level during the experiment ( $\sim 10^{-5}$  mbar).

event subset	C-background		
	$^{40}\text{Ca}$	$^{48}\text{Ca}$	$^{48}\text{Ti}$
Fusion-evaporation	2.0 %	1.6 %	0.9 %
Fusion-fission	3.1 %	2.5 %	1.5 %
DIC (QP+QT)	2.4 %	2.7 %	1.7 %
DIC (QP-only)	42 %	47 %	33 %

**Table 5.2:** Background weight in the different event subsets. As expected, the most polluted channel is the QP-only one.

event subset	Event sharing		
	$^{40}\text{Ca}$	$^{48}\text{Ca}$	$^{48}\text{Ti}$
Fusion-evaporation	27 %	33 %	33 %
Fusion-fission	3.4 %	3.7 %	3.3 %
DIC (QP+QT)	1.4 %	1.1 %	0.9 %
DIC (QP-only)	39 %	40 %	38 %

**Table 5.3:** Event sharing among the exclusive subsets expressed as the fraction of all the events with not more than two  $Z \geq 4$  fragments. Data are corrected for the Carbon background.

The effect of the background is different for the various event subsets and it is reported in Table 5.2. As said before, the pollution in fusion-evaporation, fusion-fission and QP+QT events is minimal. Only when we consider the DIC events where the QP alone was detected the pollution becomes not negligible. Thus, in the QP-only analysis (§5.4) the Carbon background cannot be neglected and the bkg-subtracted spectra were used. As shown in Table 5.3 — to be compared with Table 5.1 — the background subtraction alters significantly the event sharing. In fact, the QP-only channel weight is strongly reduced at the expense of the other subsets. For example, for the  $^{32}\text{S} + ^{48}\text{Ca}$  reactions, the QP-only event sharing drops from 52 % to 40 %.

To conclude this digression on the  $^{32}\text{S} + ^{12}\text{C}$  reactions, we notice in the left panel of Figure 5.6 the event intensification at  $v_{\text{rel}} > 30$  mm/ns. The two fragments reparate with high relative velocities not compatible with a fusion-like process from  $^{32}\text{S} + ^{12}\text{C}$ . Also we verified that statistical model calculations don't predict such kind of events which originate probably from dissipative collisions. However,

the collected statistics for  $^{32}\text{S} + ^{12}\text{C}$  is not sufficient to perform detailed analysis of this system.

## 5.2 Fusion-like events

In this part, we will discuss the reaction channel that leads to the formation of a heavy source; i.e. the fusion-evaporation and fusion-fission reactions. As evidenced in Table 1.1 on page 5, in case of complete fusion the compound nucleus (CN) reaches very high excitation energies, around 4 MeV/u. This value is above the limit where nuclear multifragmentation has been observed. However, the relatively small system size and the expected occurrence (to be verified) of some fast particle emission (which reduces the available excitation energy) should make the multifragmentation channel rather rare. As a matter of fact, in our systems we found that the events with more than 2 IMF ( $Z \geq 4$ ) are only small fractions (0.42 % and 0.35 % of the total measured events for the  $^{40}\text{Ca}$ ,  $^{48}\text{Ca}$  cases). The fission mode is an alternative or complementary way to evaporation, although with a small reduced partial width since the fissility of Krypton-like nuclei with mass  $A = 70\text{--}80$  is low.

It is interesting to study the differences in these decay modes, evaporation versus fission, as a function of the target isospin as done at low energies by the Chimera group [62]. In particular we want to investigate how the fusion-fission and fusion-evaporation change with the  $N/Z$  ratio of the target; also we would like to check pre-equilibrium effects and their possible dependence on the system isospin. To do so, we used the guidance of two models, one is the purely statistical GEMINI++ code (§4.4) and the other is the TWINGO dynamical code (§4.3) followed by GEMINI++ (see Chapter 4 for more details).

The pure GEMINI++ calculations have been performed assuming a CN formed in complete fusion reactions. Krypton ions ( $A = 72$  or  $A = 80$ ) are given as GEMINI++ input having the whole available excitation energy  $E^*$ . Only the spin  $J$  of the source is varied event by event assuming a triangular distribution that weights the involved partial waves in the fusion channel, from zero to the maximum related to the vanishing of the Coulomb barrier (calculated according to Sierk [63]).

Instead, event per event, the initial source of the TWINGO+GEMINI++ combination is the result of the specific dynamical path simulated by the SMF model. For each event the input parameters for GEMINI++, at the proper decay time (see below), are generated by the preceding dynamics: therefore  $Z$ ,  $A$ ,  $E^*$ ,  $J$  of the source change for each event. We remark that the CPU time consumed by TWINGO is quite high (about one week for 1000 events using 20 CPUs). To spare computation

time while preserving a reasonable description of the fragment phase-space after the collisions, we decided to run TWINGO for an affordable “reduced” number of representative events (10000). Then, for each primary event, we replayed the GEMINI++ code many times (2000 launches) thus widely populating the ER and LCP distributions with high enough statistics (20 Mevents).

### 5.2.1 Fusion-evaporation events

The first observable that we study in the F-E events is the charge distribution of the compound nucleus, which appears different in the two studied systems, as shown in Figure 5.7.

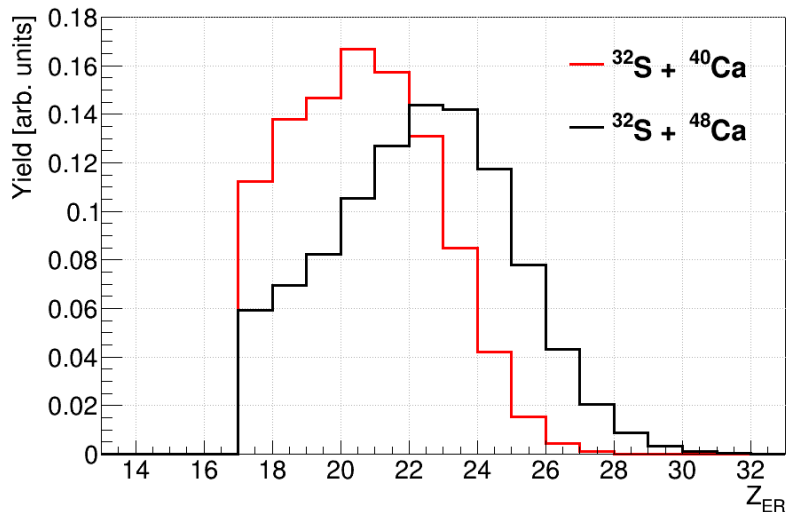


**Figure 5.7:** Charge distribution of the evaporation residues. ER are limited to  $Z > 16$  to reduce pollution from fragments coming from different reaction mechanisms

These differences, which can be also seen in the low-velocity parts of Figure 5.2, can qualitatively be understood with the different n-enrichment of the two systems. Either in case of pre-equilibrium emissions or in case of pure evaporation, the n-deficient system  $^{32}\text{S} + ^{40}\text{Ca}$  must free more charge units to dissipate the initial excitation energy which is quite similar in the two cases. Therefore, an ER with lower average atomic numbers must finally result.

The characteristics of the LCP in coincidence with the ER are a good tool to investigate the nature of the process [47, 48, 64, 65]. In the following we discuss several LCP observables comparing the experimental results with model calculations. We will consider together to the emitted particles also Lithium ions as they can be evaporated from the CN (as suggested by the GEMINI++ code). First we observe, as typically found for fusion-evaporation processes, that the LCP are dominated by

proton and  $\alpha$ -particles with minor contributions of deuterons, tritons and  ${}^3\text{He}$ . For instance, for the  ${}^{48}\text{Ca}$  case, protons represent 43 % and  $\alpha$ -particles 39 % of the total detected particles accompanying the ER. A very small percentage of  ${}^6\text{He}$  is also detected ( $\sim 0.03\%$ ).

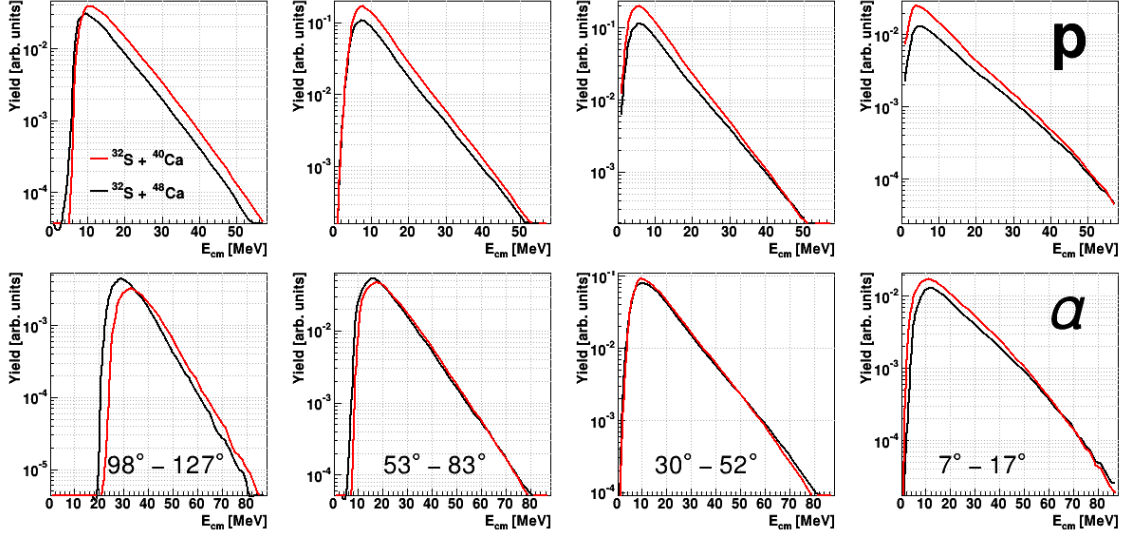


**Figure 5.8:** Experimental proton and  $\alpha$ -particle CM energy distributions at different detection angles for the two studied systems  ${}^{32}\text{S} + {}^{40,48}\text{Ca}$ . Spectra are normalized to the number of detected evaporation residues.

Energy distributions in the CM frame are shown in Figure 5.8 for protons and  $\alpha$ -particles for the  ${}^{32}\text{S} + {}^{40}\text{Ca}$  (red lines) and  ${}^{32}\text{S} + {}^{48}\text{Ca}$  (black lines) reactions. For each system the yield has been normalized to the total number of detected ER. In most cases, one clearly sees the typical Maxwellian shape for charged particle emission with a long exponential tail following the maximum positioned close to the Coulomb barrier which changes, naturally, from protons to alphas. The  ${}^{48}\text{Ca}$  spectra present slightly harder tails, maybe as a result of the slightly higher available excitation energy for fusion. Moreover it is evident that, as we will see more into detail later, the  ${}^{32}\text{S} + {}^{40}\text{Ca}$  system emits more protons with respect to  ${}^{32}\text{S} + {}^{48}\text{Ca}$ .

A more suggesting view of the emissions is presented in the Fig.5.9, where, for the same species and only for the  ${}^{48}\text{Ca}$  target, the  $v_{\perp} - v_{//}$  correlations are reported for the fusion-evaporation events. One sees the typical Coulomb ring shapes approximately centered on the CM. The  $v_{\perp} - v_{//}$  components are referred, for each event, to the flight direction of the detected ER in order to take into account the source recoil direction. The assumption of an emitting source located at CM velocity is largely satisfied at the first order of approximation.

We start now to compare the experimental data to the model predictions obtained using GEMINI++ and TWINGO+GEMINI++. As described in §4.3, for

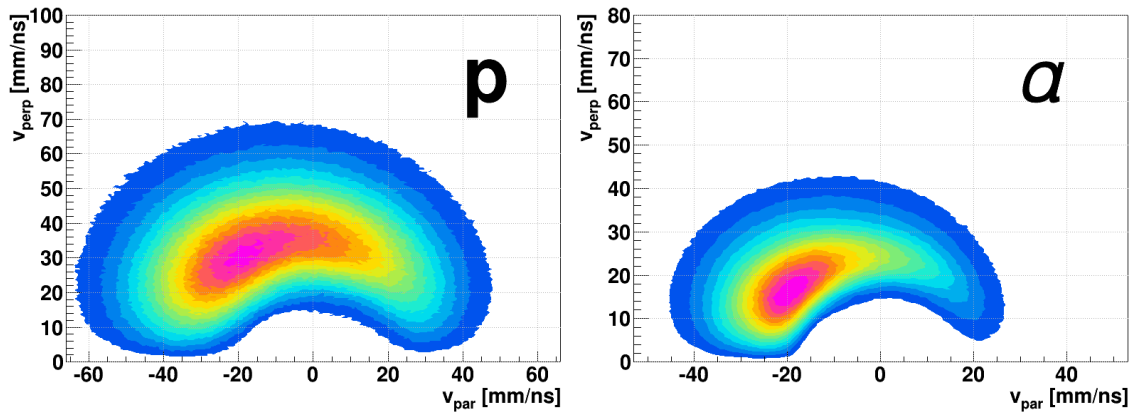


**Figure 5.9:** Experimental proton and  $\alpha$ -particle velocity distribution for the  $^{32}\text{S} + ^{48}\text{Ca}$  reactions. The velocities are calculated in the frame of the emitting nucleus (the ER) and separated in the parallel ( $v_{\text{par}}$ ) and perpendicular ( $v_{\text{perp}}$ ) components with respect to the ER direction.

each event simulated by TWINGO, the primary fragments must be identified after a reasonable time, typically in the range 200–500 fm/c. The choice of the recognition time is critical and in principle it depends on the bombarding energy, the system size, the entrance mass asymmetry and of course on the impact parameter.

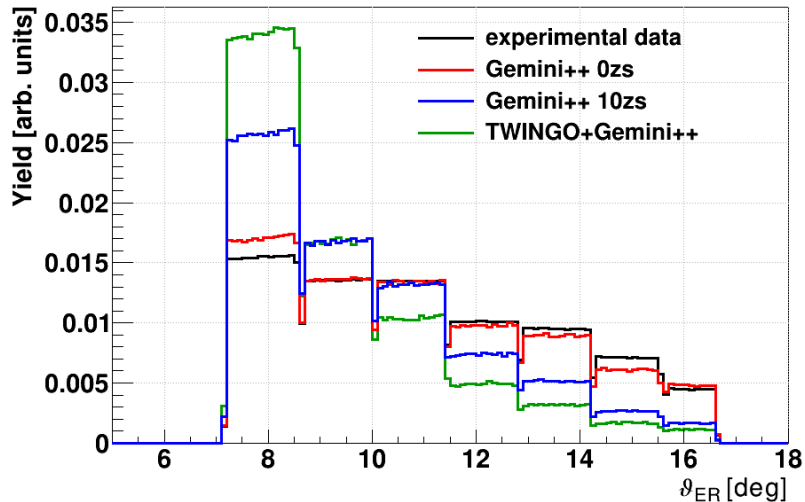


**Figure 5.10:** Evaporation residue angular distribution for the  $^{32}\text{S} + ^{48}\text{Ca}$  reactions. The yields are normalized to the total number of ERs. The overimposed Monte Carlo simulated distributions are described in the text.

As deeply discussed in §4.3, we decided to start the coalescence procedure after 300 fm/c, although this time is still not short enough to reproduce the correct excitation energy of the CN in the F-E channel. This fact is evidenced in Figure 5.10, where the ER angular distribution is shown for the  $^{32}\text{S} + ^{48}\text{Ca}$  reactions, normalized to the total number of evaporation residues. While GEMINI++ simula-

tions predicts wide distributions — in particular the one with  $\tau_f = 0$  zs — following quite well the experimental shape, the TWINGO+GEMINI++ angular distribution is strongly peaked at small angles. This means that in TWINGO the fluctuations due to particle emissions (whatever fast or evaporative) are underestimated.

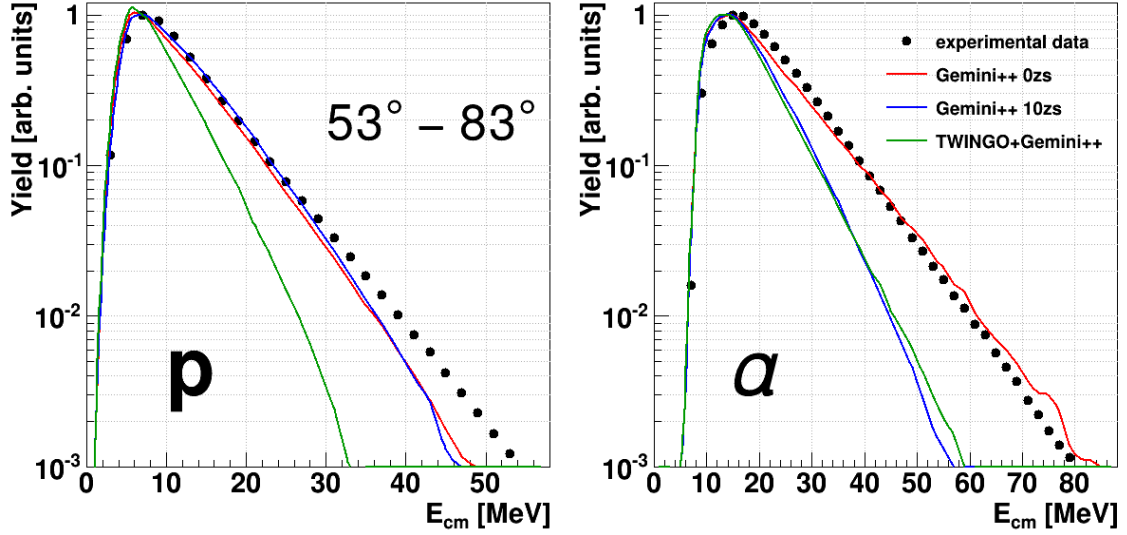


**Figure 5.11:** Proton and  $\alpha$ -particle CM energy spectra for the  $^{32}\text{S} + ^{48}\text{Ca}$  reactions. Monte Carlo simulated events are overimposed.

The low excitation energy of the CN from TWINGO is evident also in Figure 5.11, where the proton and  $\alpha$ -particle spectra are shown for the  $^{32}\text{S} + ^{48}\text{Ca}$  system. The spectra are normalized to their maximum value for an immediate shape comparison. We see that the GEMINI++ predictions fairly well reproduce both the distributions, while the agreement with the TWINGO+GEMINI++ is overall worse. Also in this case, the GEMINI++ simulation with zero fission delay time works better than GEMINI++ with  $\tau_f = 10$  zs. We remark that GEMINI++ with  $\tau_f = 0$  zs strongly favours the fission channel ( $\sim 80\%$  of the total). Moreover we observe that for Krypton CN the splits are strongly mass-asymmetric. So, when filtering with the apparatus geometry and efficiency, most of the F-F events are recognized as F-E events. In those cases one fission fragment is lost, and the other goes inside the ER gate. The heavy fission fragment resembles an ER from fusion-evaporation whose kinematics, however, results to be more disturbed with respect to only evaporation. The fact that experimental ER angular distribution and LCP energy spectra are similar to GEMINI++ with  $\tau_f = 0$  zs suggests that we truly have a very large fission probability.

As said before, about TWINGO+GEMINI++ comparison, it seems that too cold sources are decaying with respect to the experimental sources. Indeed the energy

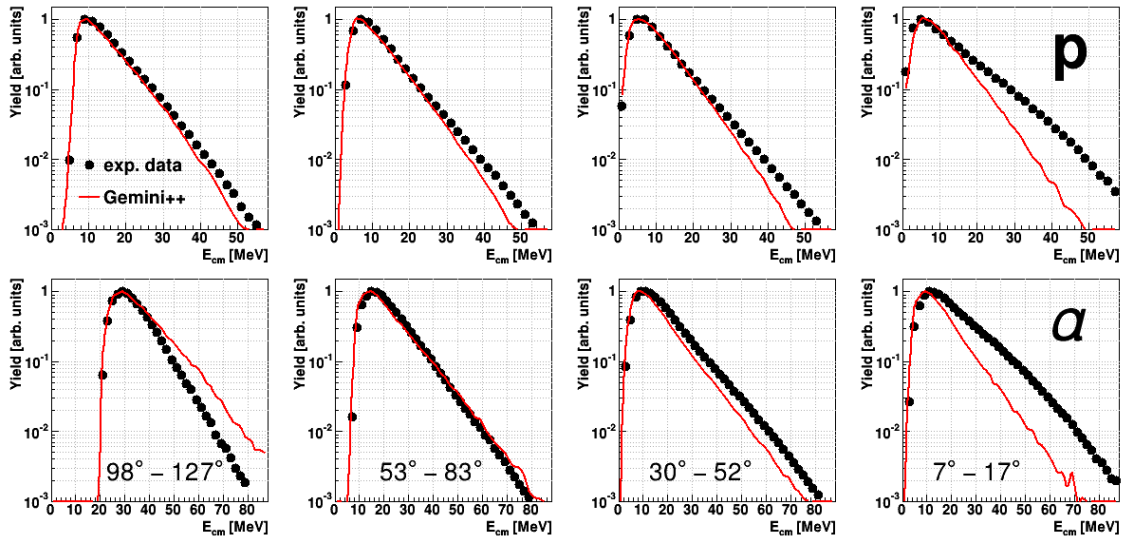


**Figure 5.12:** Proton and  $\alpha$ -particle CM energy spectra for the  $^{32}\text{S} + ^{48}\text{Ca}$  reactions. Yields are normalized to the maximum value of each spectrum. GEMINI++ with  $\tau_f = 0$  zs simulated events are overlaid.

spectra of LCP are softer, signaling a smaller temperature and a too low excitation energies. In Chapter 4, in particular in Figure 4.9 on page 67, we showed that TWINGO is producing primary CN with excitation energies less than 2.5 MeV/u, which appears not to be the case. Probably this is due to the occurrence of two effects. One is the pre-equilibrium emission, a real process that the dynamical model attempts to reproduce. The other is the long recognition time that, as said, allows for statistical particle evaporation within the TWINGO code itself, before the CN enters into the GEMINI++ simulation.

As for the pre-equilibrium, this mechanism is important and can be indeed present in our reactions which are at 17.7 MeV/u bombarding energy; it could be that TWINGO is overestimating this process. On the other hand pure GEMINI++ calculations assume the opposite, i.e. complete fusion, and this is not the case. Indeed, looking at the energy spectra in Figure 5.12, we notice in the experimental data a long energetic tail increasing at forward angles for protons and  $\alpha$ -particles, which is not reproduced by GEMINI++.

It is likely that the measured process corresponds on average to an incomplete fusion reaction. So we expect that the general average description of LCP features be reasonably given by GEMINI++ but with deviations on some important details, for instance the chemical distribution of particles which is an issue for isospin studies. To access on average the LCP multiplicities we must correct the data taking into account the detection efficiencies, that can be estimated using the model. This procedure works well under the hypothesis that the model simulated distributions, of whatever

type, reasonably span the measured domains of energy and momenta for the various species and particles. In addition, as explained in §4.5, one must accurately mimic in the analysis of simulated events all the effects which impact on the detected ions (the so called software replica of the response function of the apparatus). In other words, the models can be used to evaluate the overall efficiency of the detector for the various reaction channels and the various species thus permitting to estimate the “true” quantities (e.g. LCP multiplicities) and to attempt the source reconstruction.

	ion	G-0	G-10	TWINGO	average
$^{40}\text{Ca}$	H	6.04	5.40	6.29	$5.9 \pm 0.5$
	He	1.93	2.39	1.57	$2.0 \pm 0.4$
	Li	0.12	0.10	0.06	$0.09 \pm 0.03$
	<i>Charge removal from CN</i>				$10.1 \pm 0.6$
$^{48}\text{Ca}$	H	4.45	3.90	4.32	$4.2 \pm 0.3$
	He	1.88	2.26	1.41	$1.9 \pm 0.4$
	Li	0.15	0.12	0.06	$0.11 \pm 0.04$
	<i>Charge removal from CN</i>				$8.3 \pm 0.5$

**Table 5.4:** Experimental  $4\pi$  multiplicities for LCP and Lithium in coincidence with an ER. The values are corrected with different Monte Carlo simulations: “G-0” and “G-10” stand for GEMINI++ simulations with  $\tau_f = 0\text{zs}$  and  $\tau_f = 10\text{zs}$  respectively. The last row for each target shows the average charge removed from the CN in each F-E event.

Table 5.4 report the LCP multiplicities for the  $^{32}\text{S}+^{40,48}\text{Ca}$  reactions. The data in the table are corrected for the apparatus efficiency using three different Monte Carlo simulations: GEMINI++ with  $\tau_f = 0\text{zs}$  and  $\tau_f = 10\text{zs}$  and TWINGO+GEMINI++. For each model, the efficiency can change because the initial distributions are not the same and the global response of the apparatus is the complicated result of many effects. As a consequence, the final results in some sense are model dependent. The more faithful the model predictions are the more reliable the corrected values are. An indication of accuracy is the stability of the extracted experimental  $4\pi$  value. In our case we see that the differences between the values obtained with the different models are within 20% uncertainty for what concerns  $Z = 1$  multiplicities. Taking into account all the discussed problems, we decided to quote the average values as LCP multiplicities in  $4\pi$  as presented in the last column of Table 5.4.

For the detected ER events, one can try an average charge balance, assuming a good efficiency correction for the above multiplicities. By summing the charge numbers weighted with the  $4\pi$  multiplicities, one should obtain the initial CN charge that, in absence of pre-equilibrium, should be equal to  $Z = 36$ . For what concerns

	$^{32}\text{S} + ^{40}\text{Ca}$	$^{32}\text{S} + ^{48}\text{Ca}$
$\langle Z_{\text{LCP}} \rangle$	10.1	8.3
$\langle Z_{\text{ER}} \rangle$	22.7	25.3
$\langle Z_{\text{CN}} \rangle$	32.8	33.6
$\Delta Z$	-3.2	-2.4

**Table 5.5:** Charge balance for the detected particles in  $^{32}\text{S} + ^{40,48}\text{Ca}$  reactions. The sum of all  $4\pi$  corrected average  $Z$  is reported in the third row ( $\langle Z_{\text{CN}} \rangle$ ), while the difference with the expected  $Z_{\text{CN}} = 36$  value is indicated in the last row.

the LCP and Li, the value is reported in the last row of Table 5.4. In Table 5.5 the above mentioned charge balance is carried out, assuming for  $\langle Z_{\text{ER}} \rangle$  an efficiency correction with the GEMINI++ ( $\tau_f = 0$ zs) simulation, that better reproduces the ER distribution (see for example Figure 5.10). From the table we see that a certain charge deficit survives, larger for the neutron deficient system.

We can therefore say that with respect to GEMINI++ the experimental data suggest an amount of missing nucleons in the reconstructed CN with respect to the total system: for the  $^{40}\text{Ca}$  case we have about  $\Delta Z = -3.2$  and for the  $^{48}\text{Ca}$  case about  $\Delta Z = -2.4$ . The main message is that on average we have not complete fusion. We can note that GEMINI++ predicts, with default parameters, a rather large amount of fission. The gate selected for fusion-evaporation can contain a contribution of asymmetric fission. Asymmetric fission populates phase-space regions marginally overlapping to fusion-evaporation events; if the model predicts a sizeable (and too abundant) contribution of fission, the use of GEMINI++ to deduce the  $4\pi$  multiplicities introduces a systematic error, difficult to estimate. Of course, also experimental F-E data can be polluted by asymmetric fission. This is the reason why our first choice has been to use GEMINI++ events, for comparisons and efficiency evaluation, not restricted to only fusion-evaporation (as it could be done). However, a not realistic (with respect to truth) balance of fusion-evaporation to fusion-fission branching ratio can distort final multiplicities and thus  $Z$  balances. We verified, however, that the results don't change much by adopting GEMINI++ corrections rejecting ab initio fission events. Thus the result that we measure on average incomplete fusion-evaporation is rather convincing.

We have two other reasons to support this scenario. One comes by a careful observation of the LCP energy spectra and the other from the literature. CM energy spectra for protons and  $\alpha$ -particles were shown in Figure 5.12 compared to GEMINI++ spectra. We saw that the experimental shapes are faithfully reproduced by GEMINI++ at backward angles while a tail rises up at forward directions.

This is true for protons and  $\alpha$ -particles but also for deuterons, tritons and  ${}^3\text{He}$  whose energetic spectra (not here reported) present some shoulder or tails (not Maxwellian) growing at forward angles. This is a strong support of a contribution of non-statistical emission of LCP from the system. The literature, on the other hand, confirms this incomplete fusion scenario. Lassen [14] reports on the fusion of the system  ${}^{40}\text{Ar} + {}^{40}\text{Ca}$  from 10 to 30 MeV/u to study the limit to nuclear excitation through fusion due to pre-equilibrium emissions. The system is quite similar to ours, in particular to the lighter one. The Lassen's study suggests an increasing contribution of fast emission which prevents the system to undergo complete fusion from around 13–14 MeV/u. Lassen concentrates on free neutron emission and on mass deficit  $\Delta A = A_{\text{sys}} - A_{\text{CN}}$  while no information is shown there on charges; therefore, we can only deduce some consistency but not perform an exact comparison with our results which are based on the detection of charges. Interpolating from the pictures in the paper (reported also in Chapter 1 of this thesis, in Figure 1.3 on page 14) we deduce, at  $\sim 18$  MeV/u,  $\Delta Z \sim -5.5$  for the  ${}^{40}\text{Ar} + {}^{40}\text{Ca}$  system. The results are in fair consistency, taken into account the approximations of the method and the estimations.

The difference in the isospin of the two reactions clearly appears also in the properties of the fusion channel, as far as ER and LCP are concerned. If we look at the chemistry of the evaporated particles, we discover, as expected, that  ${}^{48}\text{Ca}$  produces relatively more n-rich H, He and Li isotopes. The measured isotopic ratios are reported in Table 5.6. We note that for this ratios we used the directly measured LCP multiplicities not scaled to  $4\pi$  via Monte Carlo corrections.

ratio	${}^{32}\text{S} + {}^{40}\text{Ca}$		${}^{32}\text{S} + {}^{48}\text{Ca}$	
	exp	G-0	exp	G-0
d/p	0.15	0.13	0.25	0.20
t/p	0.031	0.029	0.089	0.073
${}^3\text{He}/\alpha$	0.039	0.013	0.025	0.006
${}^7\text{Li}/{}^6\text{Li}$	0.69	0.61	1.45	1.20

**Table 5.6:** Experimental isotopic ratios for LCP and Li ions in coincidence with an ER for the reactions  ${}^{32}\text{S} + {}^{40,48}\text{Ca}$ . The values are compared with the GEMINI++ ( $\tau_f = 0$  zs) simulation. Errors are only statistical and they are on the last digit.

It appears that the n-richness of the target somehow persists in the measured isotopic LCP fractions. This signal is strong and it's not much disturbed by statistical uncertainty since the measurements have been done with the same calibrations and operating conditions. The same evidence appears for the GEMINI++ calculations,

also reported in the table. The model follows the n-enrichment of the target producing evaporated species that qualitatively present the same experimental trend. It clearly appears that  ${}^3\text{He}$  are experimentally more abundant than in GEMINI++ and this can be an interesting signal. However we note that  ${}^3\text{He}$  represents only 1% of the measured LCP yield in this channel.

### 5.2.2 Fusion-fission events

As described in §5.1, the measured fusion-fission channel is less populated than the F-E one. Moreover, the selection procedure is more critical. For these reasons, we will limit our analysis to LCP and fission fragment isospin. The LCP isotopic ratios will be described here while the isospin of the fission fragments will be described later in §5.4.

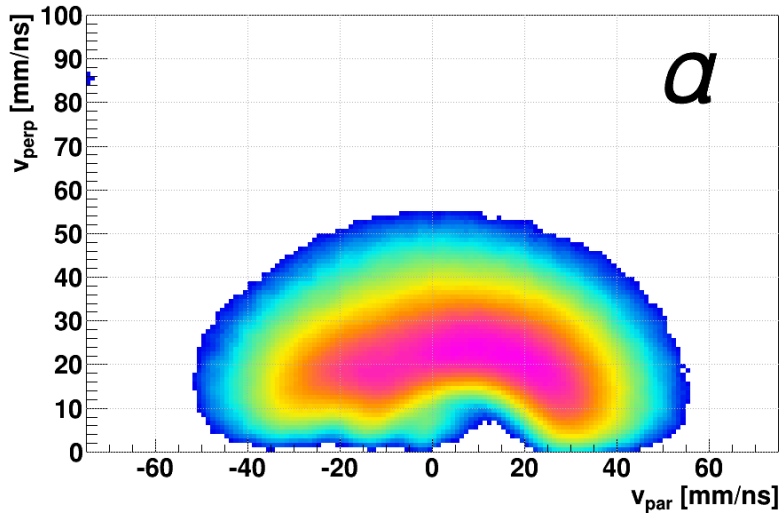


**Figure 5.13:** Fusion-fission measured events:  $\alpha$ -particle velocity distribution for the  ${}^{32}\text{S} + {}^{48}\text{Ca}$  reactions. The velocities are calculated in the centre-of-mass frame of the fission fragments and separated in the parallel and perpendicular components with respect to the direction towards the centre-of-mass of the fission fragments.

Firstly, to be sure of the event selection we show in Figure 5.13 the  $v_{\perp} - v_{\parallel}$  correlations for the  $\alpha$ -particles detected in fusion-fission events for the  ${}^{48}\text{Ca}$  target case (a similar result is found for the  ${}^{40}\text{Ca}$  case). Two Coulomb ring shapes appear, corresponding to the two different emitting sources. The  $v_{\perp} - v_{\parallel}$  components are referred, for each event, to the centre-of-mass of fission fragments in order to enhance the source separation.

In Table 5.7 the measured and simulated (GEMINI++ with  $\tau_f = 0\text{zs}$ ) isotopic ratios for LCP and Li ions are reported for the fusion-fission reactions, together with the experimental ratios found for fusion-evaporation. We immediately notice that

ratio	$^{32}\text{S} + ^{40}\text{Ca}$			$^{32}\text{S} + ^{48}\text{Ca}$		
	exp F-F	G-0 F-F	exp F-E	exp F-F	G-0 F-F	exp F-E
d/p	0.13	0.10	0.15	0.23	0.16	0.25
t/p	0.024	0.018	0.031	0.075	0.049	0.089
$^3\text{He}/\alpha$	0.030	0.015	0.039	0.022	0.008	0.025
$^7\text{Li}/^6\text{Li}$	0.63	0.50	0.69	1.33	0.98	1.45

**Table 5.7:** Experimental isotopic ratios for LCP and Li ions in coincidence with two fission fragments. For a ready comparison, also the GEMINI++ ( $\tau_f = 0$  zs) simulation for fission and the experimental data for fusion-evaporation (previous table) are quoted. Errors are only statistical and they are on the last digit.

the measured F-F ratios are very similar to the values for the F-E channel. That means that we are selecting fragments coming from a similar source (the compound nucleus from fusion-like processes) and the DIC contamination is low, as expected from the estimation reported in Table 5.1. Instead, in §5.3 — in particular in Table 5.9 — we will see that for the LCP isotopic ratios in the DIC channel the values significantly differ, as it is expected for a much lighter average source (the QP).

Due to the many similarities, the same considerations done for the fusion-evaporation channel are still valid. In particular we have that GEMINI++ follows the trend of isotopic ratios changing with the n-richness of the system. In the F-F channel, however, we have more differences between experimental data and GEMINI++ with respect to the F-E channel, in particular for what concerns t/p and  $^3\text{He}/\alpha$  ratios. However, also considering the pre-equilibrium emission and the consequent spread of sources that are not considered in the pure GEMINI++ calculations, the discrepancies cannot be too heavily considered.

### 5.3 DIC events

Concerning light particles emitted in DIC events, in Figure 5.14 the  $v_{//}$  vs.  $v_{\perp}$  correlations for protons (left) and  $\alpha$ -particles (right) for the QP+QT selection for the reaction  $^{32}\text{S} + ^{48}\text{Ca}$  are presented. In the top part experimental data are shown, while in the bottom part the results obtained by the TWINGO code with recognition time 300 fm/c and after applying GEMINI++ as afterburner, filtered with the software replica of the setup, are plotted.

Referring to Figure 5.15, in these pictures for the QP+QT selection the parallel and perpendicular components of the LCP velocity are calculated with respect to

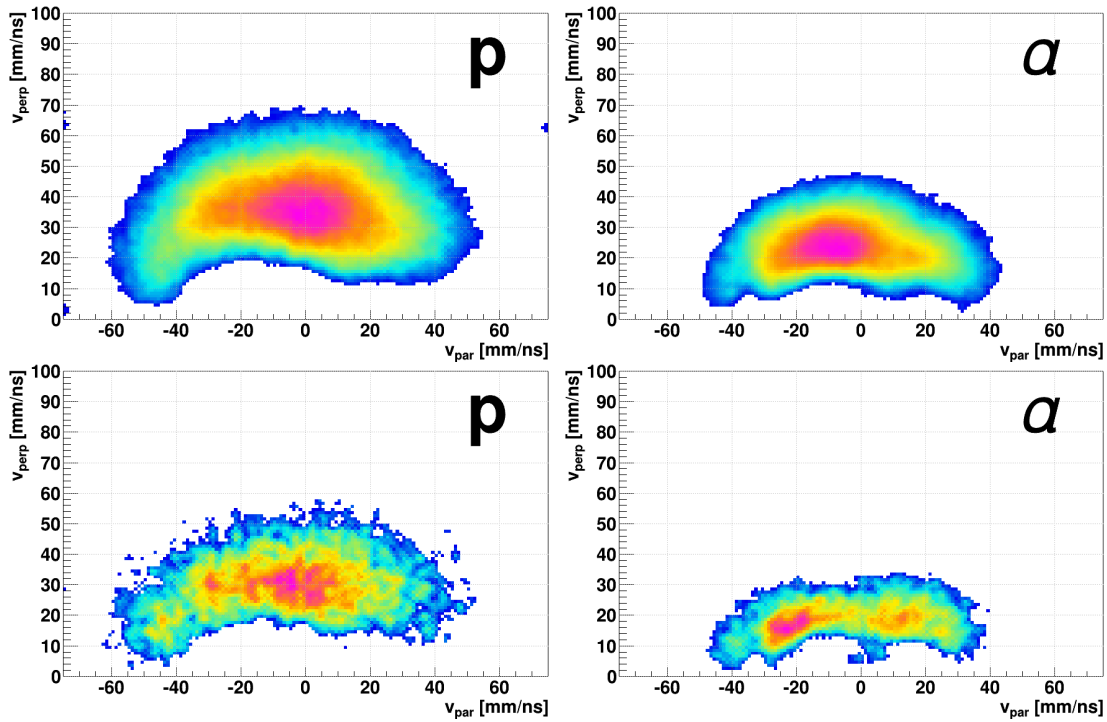


**Figure 5.14:**  $v_{\perp}$  vs.  $v_{\parallel}$  correlations for protons (left side) and  $\alpha$ -particles (right side) emitted in DIC events for the selection QP+QT. Top panels: experimental data for the  $^{32}\text{S} + ^{48}\text{Ca}$  reactions. Bottom panels: simulated and filtered events obtained from TWINGO+GEMINI++.

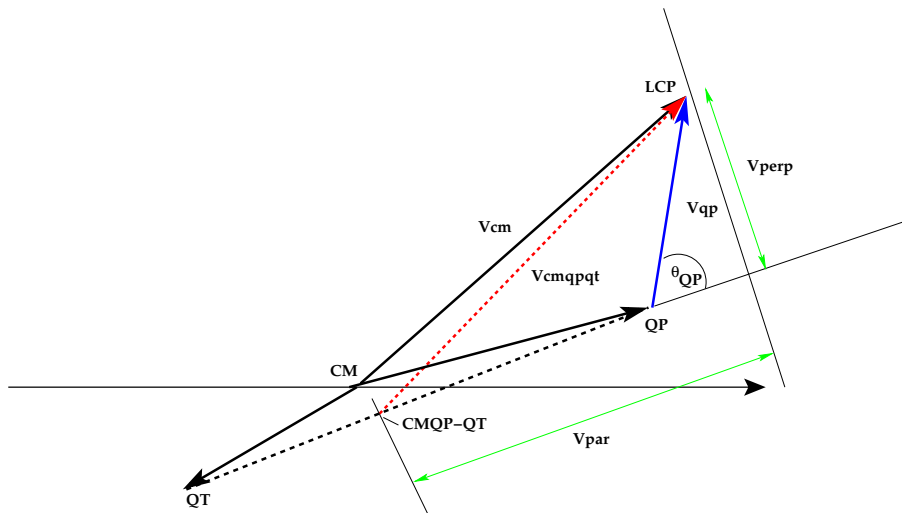


**Figure 5.15:** Reference system used for DIC events for the QP+QT selection. For QP-only selection, the centre of mass of the couple QP-QT is supposed to coincide with the centre of mass of the whole system.

the direction given by the relative velocity of QP and QT, with origin in the centre of mass of the pair QP+QT; on the contrary, for the QP-only selection, we obviously refer the LCP to the global system centre of mass velocity of the QP.

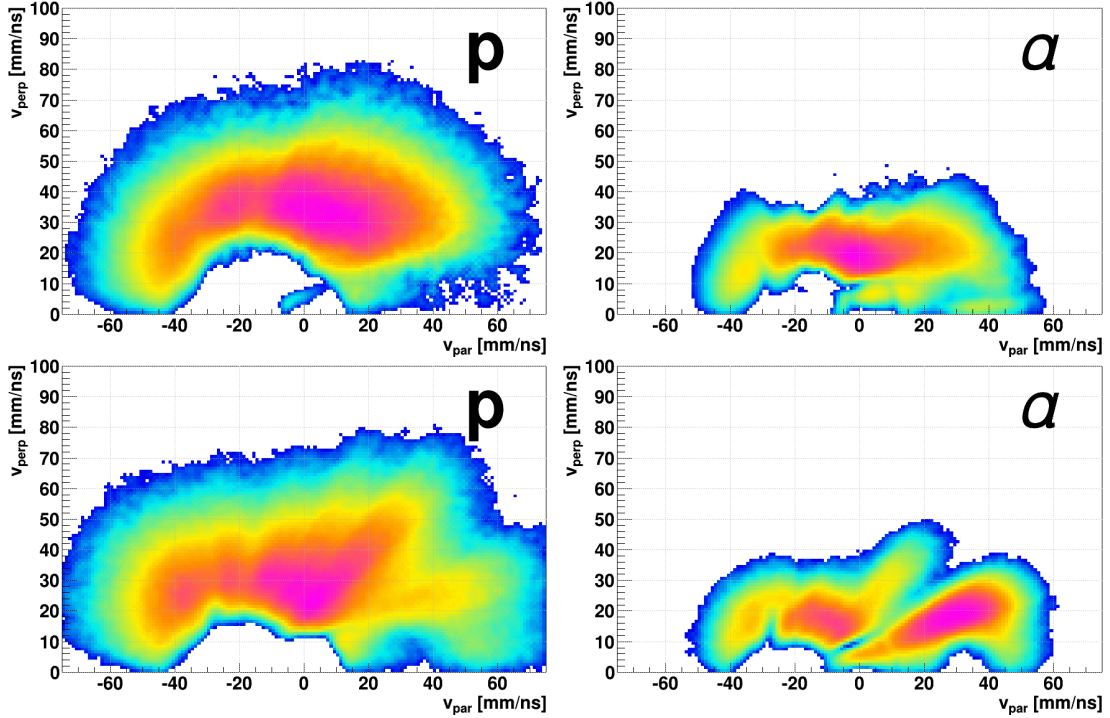


**Figure 5.16:**  $v_{\perp}$  vs.  $v_{\parallel}$  correlations for protons (left side) and  $\alpha$ -particles (right side) emitted in DIC events for the selection QP-only. Top panels: experimental data for the  $^{32}\text{S} + ^{48}\text{Ca}$  reactions after subtracting the Carbon background. Bottom panels: simulated and filtered events obtained from TWINGO+GEMINI++.

Since we have seen that the QP-only selection is strongly affected by the  $^{12}\text{C}$  background, it is important to subtract (on average, according to the procedure described in §5.1.3) this contribution before comparing with the prediction of the model, in which this effect is absent. The obtained results are shown in Figure 5.16. The background subtraction reduces the particles with high transverse velocity; in fact if they come from the C-background, they are emitted by a CN of  $^{44}\text{Ti}$  with an excitation energy much higher than the QP of the DIC of  $^{32}\text{S} + ^{40,48}\text{Ca}$ . Obviously, since it is an average correction, some mismatch can take place, leaving some regions too much heavily and others too much weakly corrected.

For both DIC selections (Figure 5.16 and 5.14) both for the experimental data and the simulation two sources (QP and QT) are quite clearly evident and the main characteristics of the experimental plots are qualitatively reproduced by the simulation. We remark that in the simulated case all the particles emitted before the recognition time are not included in the final set.

	$^{32}\text{S} + ^{40}\text{Ca}$		$^{32}\text{S} + ^{48}\text{Ca}$	
	total mult	QP forw mult	total mult	QP forw mult
p	$3.97 \pm 0.19$	$0.74 \pm 0.30$	$1.41 \pm 0.14$	$0.29 \pm 0.12$
d	$0.25 \pm 0.04$	$0.04 \pm 0.01$	$0.33 \pm 0.03$	$0.06 \pm 0.02$
t	$0.03 \pm 0.01$	$0.004 \pm 0.001$	$0.15 \pm 0.05$	$0.02 \pm 0.01$
$^3\text{He}$	$0.07 \pm 0.04$	$0.02 \pm 0.01$	$0.03 \pm 0.01$	$0.01 \pm 0.01$
$\alpha$	$0.99 \pm 0.09$	$0.11 \pm 0.01$	$0.90 \pm 0.09$	$0.08 \pm 0.02$

**Table 5.8:**  $4\pi$  corrected Light Charged Particles experimental multiplicities in DIC events adding DIC selections (QP-only and QP+QT)

The  $4\pi$  corrected experimental multiplicities for the two systems are reported in table 5.8. Both total multiplicities and multiplicities associated to particles forward emitted with respect to the QP ( $\vartheta_{\text{QP}} < 90^\circ$  in Figure 5.15), in order to avoid the QT emission, are reported in different columns. Data refers to both DIC selections (QP-only and QP+QT) after subtracting the C background. For the DIC channel the  $4\pi$  correction is much less reliable than in the case of the Fusion channel, where the expected emission path was isotropic; due to this, the errors on the obtained multiplicities are very high. The correction was obtained on the basis of the TWINGO code followed by GEMINI++.

The biggest difference in the LCP multiplicities between the two systems is observed for protons; in fact in case of  $^{40}\text{Ca}$  the total p multiplicity is 2.8 times that of  $^{48}\text{Ca}$ ; if the only QP emission is considered, protons emitted by S-like QP when the target is the n-poor one are 2.5 times those emitted for the n-rich system. This effect can be qualitatively understood considering the preferential p-emission associated to the n-poor system, as stated also by the SMF model (see Chapter 4). A strong difference in the LCP multiplicities is observed for the two systems, both when the whole emission is considered (“total mult” column) and when the only QP emission is taken into account (“QP forw mult” column). In any case the average isospin of the LCP emitted by the QP (obtained considering only particles forward emitted with respect to the QP, in order to avoid the QT contribution, “QP forw mult” column) is 0.47 for the  $^{48}\text{Ca}$  and 0.28 for the  $^{40}\text{Ca}$ . The fact that the LCP emission from the QP is more n-rich when the target is the n-rich one is a further confirmation of the isospin diffusion phenomenon.

The n-enrichment of the LCP emission from the QP can be put into evidence looking directly at the ratios of the forward-emitted experimental multiplicities (without efficiency correction and  $\vartheta_{\text{QP}} < 90^\circ$ ) among particles of different N/Z, such as d/p, t/p,  $^3\text{He}/\alpha$  and  $^6\text{He}/\alpha$  (Table 5.9). In this case the efficiency and geometrical corrections are less important because the instrumental cuts act in a

similar way (except for, in minimal part, the detection thresholds) both for the numerator and the denominator. The obtained results are presented together with the ratio  $\alpha/p$  for all the investigated systems summing both DIC selections. A clear

	$^{32}\text{S} + ^{40}\text{Ca}$	$^{32}\text{S} + ^{48}\text{Ti}$	$^{32}\text{S} + ^{48}\text{Ca}$
d/p	0.061	0.100	0.187
t/p	0.008	0.021	0.062
$^3\text{He}/\alpha$	0.132	0.095	0.105
$^6\text{He}/\alpha$	0.001	0.001	0.002
$\alpha/p$	0.257	0.400	0.449

**Table 5.9:** Experimental ratio between forward emitted ( $\vartheta_{\text{QP}} < 90^\circ$ ) particle multiplicities obtained summing both DIC selections (QP-only and QP+QT). Errors are only statistical and are on the last digit.

trend can be put into evidence looking at this table: the ratio between n-rich and n-poor particles (d/p, t/p,  $^6\text{He}/\alpha$ ) emitted by S-like QP increases when the isospin of the target increases. Concerning the  $^3\text{He}/\alpha$  ratio, where we expect the opposite trend, a larger ratio is observed for  $^{40}\text{Ca}$  than for the  $^{48}\text{Ca}$  one; the  $^{48}\text{Ti}$  constitutes an exception in this trend, thus requiring an accurate check of the particle identification procedure for the  $^{48}\text{Ti}$  case, at present still in progress. Concerning the  $\alpha/p$  ratio, we can see that it increases moving from  $^{40}\text{Ca}$  to  $^{48}\text{Ca}$ , due to the fact that, as we have seen many times, the  $^{40}\text{Ca}$  system tend to equilibrate preferentially emitting protons. The ratios calculated using data reported in table 5.8 are a bit different with respect to the values presented in table 5.9; the discrepancy among these values can give an idea of the systematic error introduced with the procedure for the correction of the geometrical efficiency.

A final comparison can be done between the multiplicities of Tables 5.4 for ER and of Table 5.8 (DIC). We see that the total multiplicities of the DIC are close, although smaller, to those of ER, for the respective target. This is reasonable as our DIC events are surely strongly dissipative due to both the trigger condition and the off-line analysis cuts. So the total excitation deposited in the binary system at the end should be converted in a rather similar final amount of particles.

Instead, if we focus on QP emissions, the multiplicity strongly drops as a consequence of the quite smaller size of the QP source. In the next future it will be much interesting to compare the quoted multiplicities of LCP emitted from S-like QP to the values reported in the literature on past studies of fusion for very light systems as O + O, N + F, Ne + C or others.

## 5.4 The isospin of the heavy fragments

The average isospin of all the detected fragments (independently of the reaction channel) as a function of the fragment charge is presented as full symbols in Figure 5.17 for the two main systems (black:  $^{32}\text{S} + ^{48}\text{Ca}$ , red:  $^{32}\text{S} + ^{40}\text{Ca}$ ) and for the complementary system  $^{32}\text{S} + ^{48}\text{Ti}$  (blue). In this picture, as in all the the following figures, only fragments detected in Si-CsI in Ring Counter are included, because only in this case their mass is fully discriminated. As expected, the average isospin is sistematically higher for the  $^{48}\text{Ca}$  case, because the total isospin of the system is higher. The  $^{48}\text{Ti}$  case is in the middle. For  $Z=4$  the difference is extremely evident. In fact, as shown in Figure 5.18, for the  $^{48}\text{Ca}$  case the isotopic distribution is more unbalanced towards n-rich isotopes ( $^9\text{Be}$  and  $^{10}\text{Be}$ ), while for the  $^{40}\text{Ca}$  case more  $^8\text{Be}$  and  $^7\text{Be}$  are produced, but since the  $^8\text{Be}$  is unstable, it is not found in the final Be yield and this provokes the valley for the  $^{40}\text{Ca}$  reaction. Again, the  $^{48}\text{Ti}$  case is in between. Similar evidences for Beryllium isotopes have been reported also in [66].

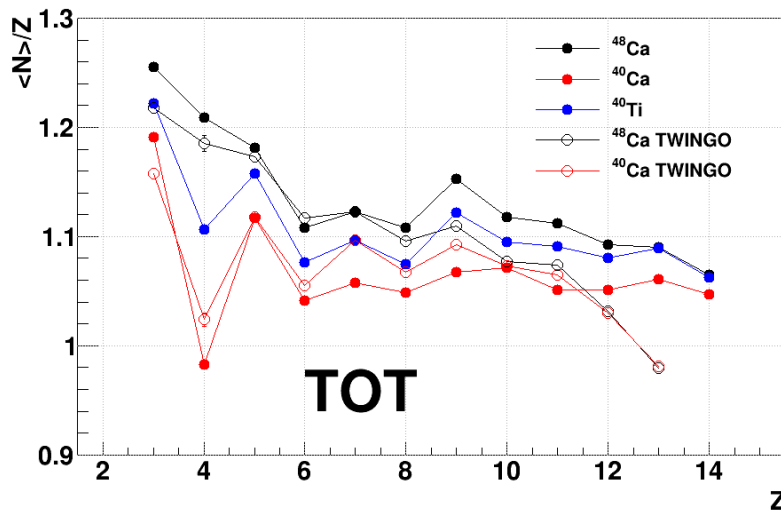


**Figure 5.17:** Average fragment isospin as a function of its charge for all the reaction channels. Black points:  $^{32}\text{S} + ^{48}\text{Ca}$  reactions; red points:  $^{32}\text{S} + ^{40}\text{Ca}$  reactions; blue points:  $^{32}\text{S} + ^{48}\text{Ti}$  reactions. Full circles: experimental data; open circles: TWINGO+GEMINI++ simulated and filtered events. The  $^{32}\text{S} + ^{48}\text{Ti}$  reaction has not been simulated.

Simulated filtered events given by TWINGO with asy-soft parametrization and recognition time 300 fm/c, followed by GEMINI++ as afterburner are also plotted in Figure 5.17 as open symbols (the  $^{48}\text{Ti}$  case is absent). At least for light isotopes the agreement with experimental data is quite good. Instead, starting from  $Z = 10$ , while in the experimental case the isospin remains different for the two reactions, in the simulation the two systems overlap. This fact may be due to a different composition of the reaction channels in the experimental case and in the simulation:

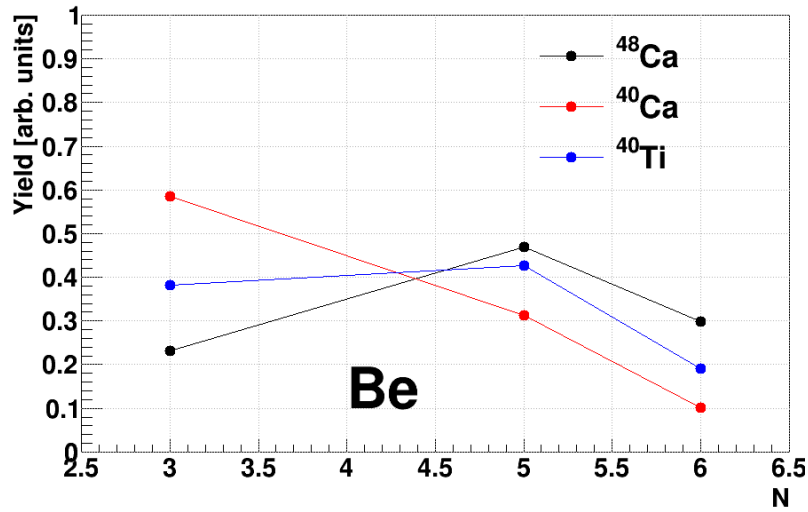


**Figure 5.18:** Isotopic distribution of  $Z = 4$  for the reactions  $^{32}\text{S} + ^{40}\text{Ca}$  (red points),  $^{32}\text{S} + ^{48}\text{Ca}$  (red points) and  $^{32}\text{S} + ^{48}\text{Ti}$  (blue points). The yields for each isotope are normalized to the total yield of  $Z = 4$ .

for example, a higher contribution of DIC in the simulation with respect to the experimental case can take to an average isospin approaching to 1 in peripheral collisions, where the isospin diffusion is negligible.

Now we focus on the specific channels. Let's consider the QP channel: the average isospin for the two different selections (QP-only and QP+QT, see §5.1.2) is plotted as full symbols in Figure 5.19 on the left and on the right side, respectively. Obviously, the average isospin of QT cannot ever be experimentally detected. A

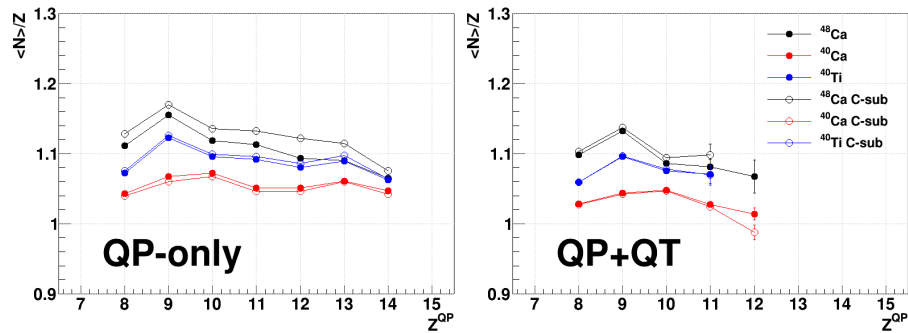


**Figure 5.19:** Average isospin of the QP as a function of its charge for QP-only (left side) and QP+QT (right side) selections. Black points:  $^{32}\text{S} + ^{48}\text{Ca}$  reactions; red points:  $^{32}\text{S} + ^{40}\text{Ca}$  reactions; blue points:  $^{32}\text{S} + ^{48}\text{Ti}$  reactions. Full circles: experimental data; open circles: experimental data after subtracting the  $^{12}\text{C}$  contamination.

clear effect of isospin diffusion is observed with both selections: the average isospin of the QP is systematically higher when the target is the n-rich one (the  $^{48}\text{Ti}$  case is in between the two Ca cases). The difference tends to decrease moving towards higher  $Z$  for the QP-only selection, i.e. when more peripheral collisions are selected,

where the isospin transport process is less effective due to the limited superposition between the two reaction partners. As it was cited in §5.1.3, the QP-only selection for the Ca case is strongly polluted by the background of  $^{12}\text{C}$ ; as a consequence, it can be interesting to produce the same isotopic distribution after subtracting (on average) such a contribution. The obtained result is plotted as open symbols in the same picture. Since the  $^{32}\text{S} + ^{12}\text{C}$  is a  $N = Z$  system as  $^{32}\text{S} + ^{40}\text{Ca}$ , when we remove its contribution, we observe only slight modifications for the  $^{40}\text{Ca}$  case, while a significant increase of the isospin is obtained for the  $^{48}\text{Ca}$ . As a consequence, the isospin diffusion effect is reinforced. For the  $^{48}\text{Ti}$  case the effect of this background subtraction is almost negligible, as expected, since in this case the pollution is weak.

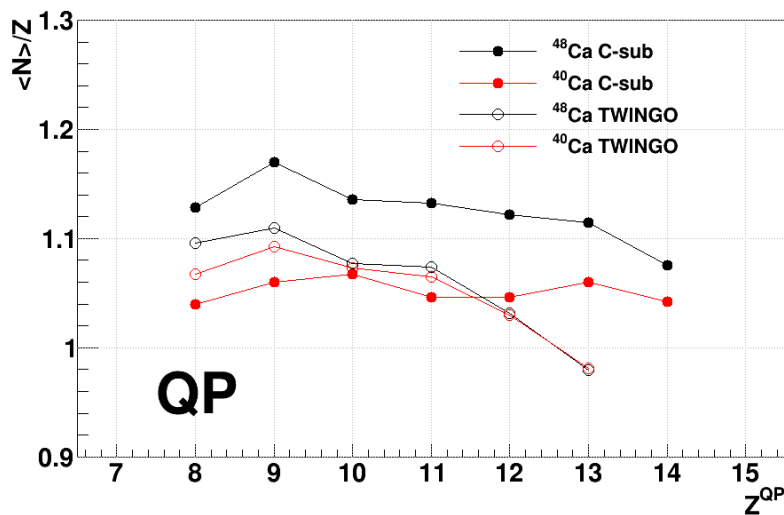


**Figure 5.20:** Average isospin of the QP as a function of its charge for QP-only selection. Black points:  $^{32}\text{S} + ^{48}\text{Ca}$  reactions; red points:  $^{32}\text{S} + ^{40}\text{Ca}$  reactions; Full circles: experimental data; open circles: TWINGO+GEMINI++ simulated and filtered events.

The QP+QT selection corresponds to less peripheral events; as a consequence the average isospin remains different of about the same amount in the three systems. In this case, as discussed in §5.1.3, the effect of C background subtraction is almost negligible. In Figure 5.20 the average isospin of QP for simulated events (TWINGO with recognition time 300 fm/c followed by GEMINI++ as afterburner) as a function of  $Z$  is compared to the experimental results after subtracting the C background. It is clear that the model underestimates the  $N/Z$  differences in the two target cases. As it has been already cited in Chapter 4, the isospin diffusion signal related to  $N/Z$  is weakened by the further decay. Thus, the found difference between the data and the model for  $N/Z$  can be related to either a too small diffusion predicted in the interaction phase or a not exact description of the sources decay. In the interpretation of all these data it is necessary to keep into account the fact that,

according to the model, about 30 % of DIC events in the QP+QT selection are really coming from a fusion-fission event, while such a contamination is almost negligible for the QP-only selection.

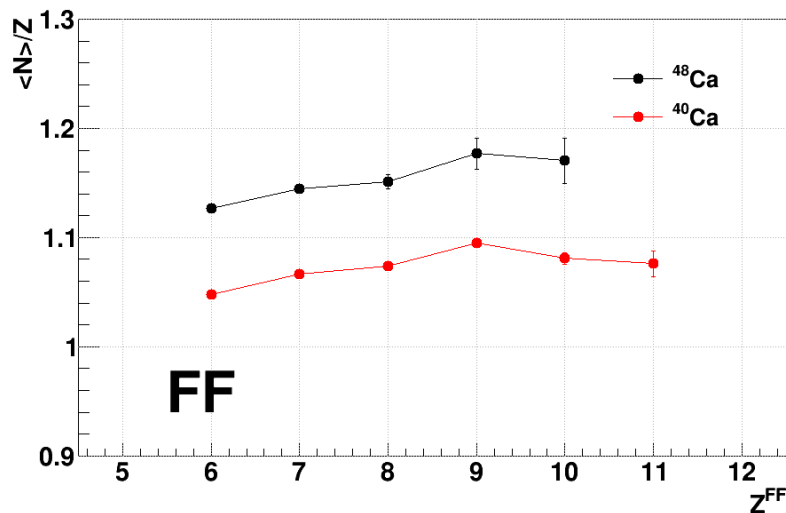


**Figure 5.21:** Average fragment isospin as a function of its charge for F-F selection. Black points:  $^{32}\text{S} + ^{48}\text{Ca}$  reactions; red points:  $^{32}\text{S} + ^{40}\text{Ca}$  reactions.

In Figure 5.21 the average isospin for the fission fragments in F-F events is shown for two reactions with the Ca target. It is important to remark that isotopic distributions are accessible only for fragments in the RCo punching through the Si layer and that this condition is not fulfilled for both fission fragments in the same event, due to kinematical reasons. As a consequence, in this plot for each event either the heavier or the lighter fission fragment is included. As expected, fission fragments coming from the n-rich reaction are more n-rich than those coming from the n-poor one, because they reflect the structure of the compound nucleus. According to the model, these events are little polluted (around 2%) by DIC events.

## 5.5 Estimation of cross sections

From the Bass model of fusion we estimate that overall cross-sections for fusion-like processes are 518 mbarn (584 mbarn) for the  $^{32}\text{S} + ^{40}\text{Ca}$  ( $^{32}\text{S} + ^{48}\text{Ca}$ ) reactions [4]. We remind also from Table 1.1 on page 5 that the total reaction cross section is expected to be 2.37 barn (2.53 barn) for the  $^{32}\text{S} + ^{40}\text{Ca}$  ( $^{32}\text{S} + ^{48}\text{Ca}$ ) reactions [3].

To experimentally extract absolute cross section values a reference and well known cross section is needed. It's common practice in heavy-ion experiments to put a small detector at a very forward angle to normalize measured counts to the

Rutherford cross section for the elastic scattering. As previously hinted in Chapter 2, in our case we put a small plastic scintillator at  $(1.00 \pm 0.05)^\circ$ . During the entire measurement the plastic scintillator collected elastic scattered  $^{32}\text{S}$  ions that were selected thanks to a window in the time of flight variable and a high threshold on the pulse height. By dividing the Rutherford cross section by the total number of elastic scattering events we obtained, for each analyzed system, the conversion factor  $f$  from counts to absolute cross section.

For a specific reaction channel, the number of experimentally selected events must be corrected for the efficiency before applying the factor  $f$ . In this regard is very important to have clean selections and reasonable simulations. In principle, we could extract  $4\pi$  corrected reaction cross sections for the three channels F-E, F-F and DIC. However, considering the uncertainties related to the F-E and F-F observed in the GEMINI++ runs with  $\tau_f = 0\text{zs}$  or  $10\text{zs}$  and the not yet deeply investigated fission features (namely fragment  $Z$  and  $A$  distributions, energy-angle correlations, etc...) we adopt here a conservative approach, not disentangling the F-E and the F-F cross sections. We assume that GEMINI++ gives a correct efficiency correction of the whole fusion-like channel, while TWINGO+GEMINI++ simulations are very indicated to correct DIC events.

Channel	G-0	G-10	TWINGO	chosen value
Fusion-like	$(0.44 \pm 0.08)\text{ b}$	$(0.68 \pm 0.13)\text{ b}$	$(1.29 \pm 0.25)\text{ b}$	$(0.56 \pm 0.08)\text{ b}$
DIC			$(1.52 \pm 0.29)\text{ b}$	$(1.52 \pm 0.29)\text{ b}$
Total				$(2.08 \pm 0.30)\text{ b}$

**Table 5.10:** Experimentally estimated absolute cross sections for the different reaction channels for the  $^{32}\text{S} + ^{40}\text{Ca}$  reactions. The values are corrected for the efficiency as better explained in the text. “G-0” and “G-10” stands for GEMINI++ simulations with  $\tau_f = 0\text{zs}$  and  $\tau_f = 10\text{zs}$  respectively.

Channel	G-0	G-10	TWINGO	chosen value
Fusion-like	$(0.33 \pm 0.06)\text{ b}$	$(0.57 \pm 0.11)\text{ b}$	$(1.06 \pm 0.20)\text{ b}$	$(0.45 \pm 0.06)\text{ b}$
DIC			$(1.36 \pm 0.26)\text{ b}$	$(1.36 \pm 0.26)\text{ b}$
Total				$(1.81 \pm 0.27)\text{ b}$

**Table 5.11:** As Table 5.10 for the  $^{32}\text{S} + ^{48}\text{Ca}$  reactions.

In Tables 5.10 and 5.11 the total reaction cross section is estimated also separating the fusion-like and DIC components. Different models were used for the efficiency

correction. For example, in the third and fourth columns the fusion-like cross sections obtained thanks to GEMINI++ simulation with  $\tau_f = 0$  zs and  $\tau_f = 10$  zs are reported, while the TWINGO corrected values for fusion-like and DIC are indicated in the fifth column.

We need to give some comment on the above table. First of all, the two fusion-like cross sections obtained from the two different GEMINI++ parametrizations have a fairly acceptable agreement in both  $^{32}\text{S} + ^{40}\text{Ca}$  and  $^{32}\text{S} + ^{48}\text{Ca}$  reactions. Thus, we take their average value as our measured fusion-like cross section. We notice that with respect to the Bass systematics, the value obtained for  $^{40}\text{Ca}$  is in perfect agreement, while the value obtained for  $^{48}\text{Ca}$  is a bit lower. The TWINGO corrected value for fusion-like is very anomalous. This is due to the poor reproduction of the ER angular distribution: since TWINGO predicts very forward focused evaporation residues, they mainly go in a region that is not covered by any detector. Thus, the predicted efficiency is very low and this imply a big  $4\pi$  correction (presumably overestimated) on experimental data. However, the DIC distributions should be correctly reproduced by TWINGO, so we consider the extracted DIC cross section as reliable.

Summing fusion-like and DIC cross sections, we obtained an estimation of the total cross section. We can see that for the  $^{32}\text{S} + ^{40}\text{Ca}$  system the value is compatible with the predicted one, while for the  $^{32}\text{S} + ^{48}\text{Ca}$  reactions we obtain a slightly lower value. Nevertheless a lower value of the total reaction cross section is acceptable if we consider that in our experimental analysis we cut all the more peripheral collisions by requiring a coincidence trigger and these trigger conditions might not be perfectly reproduced by the filtered Monte Carlo simulations.

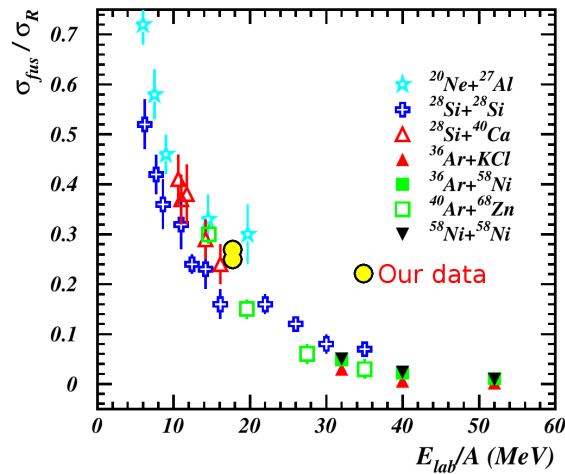


**Figure 5.22:** Lautesse systematics [12] for the ratio between fusion and total reaction cross sections. Our data are found to be consistent with the many other measurements.

In Figure 5.22 we compare our predicted values for the ratio between fusion and total cross section with a cross section systematics proposed by Lautesse [12]. Our data nicely follow the distribution of all the other considered experiments.

---

## Summary and conclusions

---

This Thesis discussed the experimental study of two heavy ion reactions at bombarding energies where the full description of the dynamics in terms of mean-field only is not still valid and N-N collisions start contributing. Therefore, fast processes such as preequilibrium emission may appear. The study compared mainly two similar systems  $^{32}\text{S} + ^{40,48}\text{Ca}$  and aimed at describing with some details the various reaction channels also as a function of the initial (different) isospin ratios ( $N/Z = 1$  and  $1.22$  in the two cases). A third system ( $^{32}\text{S} + ^{48}\text{Ti}$ ), having an intermediate value of isospin ratio ( $N/Z = 1.11$ ) was investigated, too.

The idea was to see if and how the fragment properties and the reaction channel weights change when changing the n-enrichment of the target which can translate in the n-enrichment of the whole system. The events were registered in an experiment carried out at the LNL Legnaro laboratories using  $^{32}\text{S}$  beams at  $565\text{ MeV}$  and using the GARFIELD-RCo multidetector. The apparatus is a  $\Delta E - E$  multitelescope gas-Si-CsI array with big efficiency for charged products (it covers  $\sim 60\%$  of solid angle) and with a very performing electronics based on fast sampling boards. This allows to exploit at our best the identification capability of the detectors. A large part of the Thesis concerned the detector calibrations, the verification of the hundreds channels, the optimization of the identification procedure in the framework of a calibration package, C++ based, which I contributed developing. In particular the improvement of the energy loss calculations of the heaviest ejecta in the gas of the ionization chamber has been very important.

Three major event classes have been selected in our bulk of data, for each reaction, corresponding to the main expected reaction channels. First, the fusion-like events with the formation of a biggest fragment, the remnant of the excited com-

pound nucleus after deexcitation, plus coincident particles. Second, events with two main fragments, accompanied by particles, which can be candidates for fusion-fission events. Third, the class of deep inelastic events, further dividing this subset in the events where only the quasi-projectile QP was detected together with some particles and the very dissipative binary collisions, where both major fragments have been collected.

Due to the fact that Calcium metal is very chemically reactive, the targets were protected with Carbon depositions on both sides, with reduced thickness around 4% of the Ca one. The background of the reactions on C when studying the  $^{32}\text{S} + ^{40,48}\text{Ca}$  and the  $^{32}\text{S} + ^{48}\text{Ti}$  reactions has been evaluated and discussed using runs purposely collected for the reaction  $^{32}\text{S} + ^{12}\text{C}$  during the experiment.

As for the data interpretation of the results, we used two different models, both in the form of Monte Carlo simulations in order to mimic as realistically as possible all the effects of our set up and analysis. The first is a statistical model, in the version of GEMINI++, a well acknowledged evaporation code able to describe the decay of the hot nuclei which form during the reactions. This model has been used for the fusion (evaporation and fission) subset assuming that the hot source is the CN originated from fusion processes with full momentum transfer. We were aware that the excitation energy density of our compounds, in case of complete fusion, overcomes the typical application range of GEMINI++ which is below 3MeV/u. However, neglecting multifragmentation events which would call for an expanding source (and thus for concepts quite out the GEMINI++ reasonable limits), we guessed that GEMINI++ extrapolations at high energy can constitute a rather reasonable starting point for a statistical interpretation, to be a posteriori confirmed and commented. Beside fusion events, the statistical model GEMINI+++ has been the “afterburner” choice, in our analysis, to follow event by event the decay chain of whatever hot nuclear source can be formed at the various impact parameters.

Importantly, in this thesis we demonstrated, for the first time below 20 MeV/u, the full employ of a dynamical transport model of the stochastic mean field type. Here the word “full” means in a comprehensive way; the code has been used to produce events distributed over all impact parameters just as we believe the measured events are, thanks to the big acceptance of GARFIELD-RCo. It’s important to have a dynamical code able to follow with a certain detail the evolution of the reaction mechanisms from peripheral to central collisions. The adopted SMF model is in the version of the TWINGO code, developed by Dr. Maria Colonna (LNS INFN), who has been in close contact with me and was kindly ready for fruitful discussions. The idea was to test the SMF, amply used to predict fragment properties and the

reaction mechanism features at Fermi energies, also at lower energies in order to learn about its applicability and to possibly refine some aspects to make it more predictive. The SMF is particularly important to describe the isospin transport and in general the isospin effects related to the details of the  $E_{\text{sym}}$ , the symmetry energy term of the nuclear potential. The variation of  $E_{\text{sym}}$  vs. the excitation energy and the density is not well known. On the other hand  $E_{\text{sym}}$  plays a not negligible role in the description of nuclei far from the stability, both as far as their structure or reaction mechanisms are concerned. Also, the details of  $E_{\text{sym}}$  in exotic regions of the EoS are important to improve the prediction in astrophysical contexts (e.g. supernovae explosions). The original aspect of this thesis, concerning SMF, has been its full implementation within the analysis tools and routines which have been used to produce the simulated distributions to be compared with the data. For the first time, at our knowledge, this has been performed in a coherent way, running the code to produce primary distributions as a function of all impact parameters from zero to the grazing one.

The main results are summarized as follows. The fusion channel appears to be related on average to incomplete fusion, in agreement with previous findings reported in the literature for similar systems. This means that part of the nuclear matter doesn't participate to the fusion process and it escapes on faster time scales. The pre-equilibrium emission seems to depend on the  $N/Z$  of the system being more proton rich for the  $^{40}\text{Ca}$  case. As a matter of fact the target isospin has an impact of the final fragment properties and associated particles. This means, as expected, that even in presence of pre-equilibrium emissions with more neutrons for the  $^{48}\text{Ca}$  target, the neutron contents are still different in the two cases for the formed nuclei. The GEMINI++ code overall does a good job as it describes reasonably most of the emitted particle features. At forward angles, the CM energy spectra deviate from the pure statistical predictions but, as said, this is not surprising because the charge balance (in agreement with the literature) suggests the presence of some pre-equilibrium emission (several percent on charge). The pre-equilibrium of course, if present, alters the initial state of the hot CN which is not more given by the exact conservation of target plus projectile quantities. However, since the pre-equilibrium is a correction, the main features remain of the statistical type as predicted by GEMINI++. We didn't start any iterative procedure to better follow the description of the primary source to be input into GEMINI++ on average. Instead, as said, we tried to verify the predictions of SMF: if the dynamics is reasonably well described, the code should automatically predict the contribution of pre-equilibrium and thus produce hot CN sources distributed accordingly. The further decay of the species

have been modeled, for each event, with GEMINI++. We discussed in the thesis the issue of the coalescence-recognition time of the primary fragments produced by SMF with the implications of this choice on the following distributions. In general, TWINGO reproduces correctly the main features of the collisions, at the various impact parameters. However, in case of fusion-like events it leads to too cold fragments because, by waiting for a recognition time sufficient to properly distinguish the fusion from the DIC events, pre-equilibrium and evaporative nucleons are emitted and the further afterburner stage is applied to too “cold” sources. Using shorter recognition times (down to 200 fm/c) helps but doesn’t fix the problem which will be in future still investigated.

The results for the isospin diffusion can be summarized as follows. We detected a sizeable difference in the average  $N/Z$  of QP (coming from Sulphur projectiles) when changing the target from  $^{40}\text{Ca}$  to  $^{48}\text{Ca}$ . Since the  $^{32}\text{S} + ^{40}\text{Ca}$  is charge balanced in itself, the measured isospin of QP should be close to one and essentially constant (whatever the final charge) apart from shifts due to pre-equilibrium or evaporative emission. This is indeed the case (Figure 5.21, 5.20 and 5.19): isospin is constant at around 1.05 for the various  $Z$  whatever the reaction channel selection. When hitting the  $^{48}\text{Ca}$ , the QP appears to be more neutron rich as a consequence of the isospin diffusion process. The development of the process is clearly a function of the impact parameter because the  $N/Z$  of QP increases in DIC event selection when moving from heavier QP (low excitation) to lighter remnants (high excitation) as in fig.5.21. For events classified as fusion—fission, which are of course strongly dissipative (more central, only), the  $N/Z$  differences are larger and not much  $Z$ -dependent because the initial source (the incompletely fused compound) keeps memory of the different system isospin (fig.5.19). As for the important model test (see Figure 5.20) we can see that it perhaps underestimates the isospin diffusion processes; whatever the motivations, it predicts too much similar QP isospin in the two target cases. Observing the figure one sees that  $N/Z$  increases from heavy to light remnants for both targets. This is expected for the  $^{48}\text{Ca}$  target (which still remain below the experimental points) while for the  $N = Z$  system can be only the result of an overpredicted proton emission which lifts up the  $^{40}\text{Ca}$  isospin.

---

## Bibliography

---

- [1] P. J. Siemens, *Nature*, 410 (1983).
- [2] B. Borderie et al., *Prog. Part. Nucl. Phys.* **61**, 551 (2008).
- [3] S. K. Gupta et al., *Z. Phys. A* **317**, 75 (1984).
- [4] R. Bass, *Nucl. Phys. A* **231**, 45 (1974).
- [5] R. Bass, *Phys. Rev. Lett.* **39**, 265 (1977).
- [6] D. R. Bowman et al., *Phys. Rev. Lett.* **70**, 3534 (1993).
- [7] M. D'Agostino et al., *Phys. Lett. B* **371**, 175 (1996).
- [8] L. Beaulieu et al., *Phys. Rev. Lett.* **84**, 5971 (2000).
- [9] A. S. Botvina et al., *Phys. Rev. C* **59**, 3444 (1999).
- [10] V. Baran et al., *Nucl. Phys. A* **703**, 603 (2002).
- [11] W. von Oertzen et al., *Phys. Rev. C* **78**, 044615 (2008).
- [12] P. Lautesse et al., *Eur. Phys. J. A* **27**, 349 (2006).
- [13] H. Morgenstern et al., *Phys. Rev. Lett.* **52**, 1104 (1984).
- [14] L. Lassen et al., *Phys. Rev. C* **55**, 1900 (1997).
- [15] W. Rösch et al., *Nucl. Phys. A* **496**, 141 (1989).
- [16] M. T. Magda et al., *Phys. Rev. C* **53**, R1473 (1996).
- [17] T. H. R. Skyrme, *Nuclear Physics* **9**, 615 (1959).
- [18] C. Hartnack et al., *Phys. Rev. Lett.* **96**, 012302 (2006).
- [19] V. Baran et al., *Phys. Rep.* **410**, 335 (2005).
- [20] C. J. Horowitz et al., *J. Phys. G* **41**, 093001 (2014).
- [21] M. Colonna et al., in *Dynamics and thermodynamics with nuclear degrees of freedom*, edited by P. Chomaz et al. (Springer Berlin Heidelberg, 2006), pp. 165–182.

- 
- [22] A. R. Raduta et al., Phys. Rev. C **75**, 024605 (2007).
- [23] A. R. Raduta et al., Phys. Rev. C **75**, 044605 (2007).
- [24] W Lin et al., arXiv:1401.0363 (2014).
- [25] M. D’Agostino et al., Nucl. Phys. A **875**, 139 (2012).
- [26] GARFIELD *homepage*, <http://www.lnl.infn.it/~garfweb/garf/>.
- [27] M. Bruno et al., Eur. Phys. J. A **49**, 128 (2013).
- [28] A. Moroni et al., Nucl. Instr. and Meth. A **556**, 516 (2006).
- [29] G. F. Knoll, *Radiation detection and measurement* (John Wiley & Sons, 2000).
- [30] J. Billard et al., Journal of Instrumentation **9**, P01013, 1013P (2014).
- [31] G. Pasquali et al., Nucl. Instrum. Meth. A **570**, 126 (2007).
- [32] N. Le Neindre et al., Nucl. Instr. and Meth. A **701**, 145 (2013).
- [33] L Bardelli et al., Nucl. Instrum. Meth. A **521**, 480 (2004).
- [34] M. Pârlog et al., Nucl. Instrum. Meth. A **482**, 693 (2002).
- [35] G. Casini et al., *Refining energy calibrations of the nucl-ex csi(tl) scintillators*, Annual Report (LNL, 2004).
- [36] L. Morelli et al., Nucl. Instrum. Meth. A **620**, 305 (2007).
- [37] L. C. Northcliffe et al., Atomic Data and Nuclear Data Tables **7**, 233 (1970).
- [38] R. Bimbot et al., Radiation Effects and Defects in Solids **110**, 15 (1989).
- [39] F. Hubert et al., Atomic Data and Nuclear Data Tables **46**, 1 (1990).
- [40] *Vedaloss homepage*, <http://indra.in2p3.fr/KaliVedaDoc/KVedaLossDoc/KVedaLoss.html>.
- [41] *Srim/trim homepage*, <http://www.srim.org>.
- [42] M. Barbui et al., Nucl. Instr. and Meth. B **268**, 2377 (2010).
- [43] P. Diwan et al., Nucl. Instrum. Meth. B **174**, 267 (2001).
- [44] A. Ono, Phys. Rev. C **59**, 853 (1999).
- [45] M. Colonna et al., Nucl. Phys. A **642**, 449 (1998).
- [46] J. Rizzo, “Collective and stochastic observables in heavy ion collisions at intermediate energies”, PhD Thesis (Università degli studi di Catania, 2007).
- [47] R. J. Charity, Phys. Rev. C **82**, 014610 (2010).
- [48] L. Morelli et al., J. Phys. G **41**, 075107 (2014).
- [49] M. Ciemała et al., Phys. Rev. C **91**, 054313 (2015).
- [50] S. Valdré et al., submitted to Phys. Rev. C (2015).
- [51] R. J. Charity et al., Nucl. Phys. A **483**, 371 (1988).
- [52] S. A. Kalandarov et al., Phys. Rev. C **83**, 054611 (2011).

- 
- [53] K. Mazurek et al., Phys. Rev. C **91**, 041603 (2015).
  - [54] W. Hauser et al., Phys. Rev. **87**, 366 (1952).
  - [55] L. G. Moretto et al., Nucl. Phys. A **247**, 211 (1975).
  - [56] N. Bohr et al., Phys. Rev. **56**, 426 (1939).
  - [57] A. Y. Rusanov et al., Phys. At. Nucl. **60**, 683 (1997).
  - [58] S. Valdré et al., EPJ Web of Conferences **66**, 03090 (2014).
  - [59] S. Valdré, Il Nuovo Cimento C **38**, 66 (2015).
  - [60] R. J. Charity, Phys. Rev. C **58**, 1073 (1998).
  - [61] V. E. Viola et al., Phys. Rev. C **31**, 1550 (1985).
  - [62] S. Pirrone et al., EPJ Web of Conferences **17**, 16010 (2011).
  - [63] A. J. Sierk, Phys. Rev. C **33**, 2039 (1986).
  - [64] J. Cabrera et al., Phys. Rev. C **68**, 034613 (2003).
  - [65] L. Morelli et al., J. Phys. G **41**, 075108 (2014).
  - [66] K. Brown et al., Phys. Rev. C **87**, 061601 (2013).



---

## Ringraziamenti

---

Scrivere una tesi è un'impresa. Scrivere una tesi di dottorato lo è ancor di più. Fortunatamente mi sono trovato a lavorare all'interno di una collaborazione eccezionale, con un tutor sempre presente, sabati e domeniche compresi, che ha passato innumerevoli serate a riguardare ogni bozza che gli ho spedito. Grazie. Sempre all'interno del gruppo, un ringraziamento particolare va a Silvia e Sandro, il cui aiuto nella fase di calibrazione e di analisi dei dati è stato fondamentale, per non parlare delle ultime settimane in cui il loro lavoro di meticolosa rilettura della tesi ha portato alla luce ogni più piccola sbavatura. Grazie alla Dott.ssa Maria Colonna per l'importantissimo contributo che hanno apportato alla tesi le proficue discussioni sulla materia nucleare ed sul modello SMF. Grazie al Prof. Bini, al Prof. Pasquali ed ai colleghi dei Laboratori di Legnaro, il cui costante lavoro sull'apparato sperimentale ha permesso la piena riuscita dell'esperimento trattato in questa tesi e di tutti quelli svolti fino ad ora.

Questa tesi non sarebbe comunque arrivata alla fine senza l'affetto degli amici e dei parenti. Grazie ai miei genitori, che mi hanno sopportato in questi mesi in cui tornavo a casa solo per mangiare e dormire. Infine il ringraziamento più speciale va a Claudia, che mi è stata sempre vicino.